SYNCHROTRON-BASED X-RAY CHARACTERIZATIONS OF HIGH CAPACITY ANODE MATERIALS IN LITHIUM-ION BATTERIES

by

Tianyi Li

A Dissertation

Submitted to the Faculty of Purdue University

In Partial Fulfillment of the Requirements for the degree of

Doctor of Philosophy

School of Mechanical Engineering

West Lafayette, Indiana

December 2020

THE PURDUE UNIVERSITY GRADUATE SCHOOL
STATEMENT OF COMMITTEE APPROVAL

Dr. Likun Zhu, Co-Chair

Department of Mechanical and Energy Engineering

Dr. Kejie Zhao, Co-Chair

School of Mechanical Engineering

Dr. Steven Wereley

School of Mechanical Engineering

Dr. Li Qiao

School of Aeronautics and Astronautics

Approved by:

Dr. Nicole Key

Dedicated to my parents Liang Li and Hua Li

ACKNOWLEDGMENTS

TABLE OF CONTENTS

LIST OF FIGURES

10

ABSTRACT

Lithium-ion batteries have been widely used in current numerous devices include laptops, smartphones, medical devices, and electric vehicles. The high specific energy with low maintenance and limited self-discharge characteristics of lithium-ion batteries changed the way of communications and transportations during the last few decades. The current commercial anode material for lithium-ion batteries is graphite because of its well-defined layered structure and good cycling stability with a specific capacity of 372 mAh g^{-1}. But the energy density of graphite is limited and will not likely satisfy the increasing market demand on high capacity batteries. Therefore, it is essential to develop and investigate alternative anode materials.

Currently, there is growing interest in using other group IV elements such as silicon (Si), germanium (Ge), tin (Sn) due to their high theoretical capacity. However, the intrinsic volume changes during (de)lithiation processes lead to mechanical pulverization and unstable solid electrolyte interface of the active materials, resulting in delamination and capacity fading issues. To address these problems, fundamental understandings related to the chemical and microstructural evolutions of high capacity anode materials are necessary and beneficial.

This dissertation is mainly focused on the chemical and morphological evolutions of Ge, Sn, and gallium liquid metal-based anode materials by using synchrotron-based characterizations including transmission X-ray microscopy (TXM), X-ray diffraction (XRD), X-ray absorption spectroscopy (XAS), and computed nanotomography (NanoCT). The main objective is to investigate the morphological and chemical evolutions of the active materials. The impacts caused by particle size and shape variations and the interactions between different particles on the same electrode has been examined and interpreted by employing tin as the anode. Composites containing a high capacity anode and stress accommodating phase is a promising approach to withstand massive strain in the high capacity anode materials. The effect of selenium doping into germanium anode and the formation of the in-situ formed stress accommodation phase have been studied to explain the good cycling and rate capability of selenium-doped germanium comparing to the germanium anode itself. Pulverization and delamination are a major concern which limits the implementation of high capacity anode materials. Combining a liquid metal anode with a solid electrolyte provides a potential strategy to solve cracking problems due to its self-healing ability at room temperature. Cracks formed due to volume expansion can be recovered by the fluidity of

the liquid metal and the performance of the gallium tin alloy typed anode has been presented. Although the battery system involves a complex structure including electrodes, membrane, electrolyte, etc. The complicated architecture limits the understanding of the material itself. Therefore, it is in need to investigate the active material stand along without interferences caused by other factors. A novel designed single particle schematic has been implemented and interpreted herein which provides insights into the dynamic compositional and morphological characteristics of the selenium-doped germanium anodes under the operational condition that helps understand the outstanding reversibility and cycling performance.

1. INTRODUCTION

The demand for high-performance rechargeable batteries has become universal in recent years. Lithium-ion batteries have been widely used in portable devices and become the most popular energy storage devices since it was first commercialized by SONY in 1991 [1]. Lithium-ion batteries were considered as alternative renewable energy and the revolutionization of portable electronics led to a drastically increases in different research interest aspects of them through the following years. The objective of the research has not been altered over the years although the growth and progression of battery research were astounding and impressive. People in the 20th century were enthusiastic about fossil fuel which leads to environmental issues, climate change, and oil crises [2] that motivated the research for the alternative energy system to replace petroleum. The previous battery technologies existed before including nickel-metal hydride and lead-acid systems possessed relatively low energy densities that limit their future applications. Li-ions occupied characteristics of the small atomic radius and high diffusion coefficient appeared to be promising for the high energy density demands of portable energy storage systems [3]. The challenges of finding a suitable anode were problematic due to the concern regarding energy efficiency and safety. In addition to the current commercial graphite anode that delivers a theoretical capacity of 372 mAh g^{-1}, other candidates such as silicon (3590 mAh g^{-1}), germanium (1384 mAh g^{-1}), tin (994 mAh g^{-1}), and gallium (769 mAh g^{-1}) have attracted significant attention due to their high theoretical capacities. However, the concept of alloy-typed anodes was discouraged due to the volume change and the subsequent pulverization and delamination problems. Therefore, it is necessary to understand the mechanisms of evolution on the microstructural and compositional aspects.

The objective of the present dissertation is to investigate the chemical and morphological changes during operational conditions. The content has been separated into four parts include (1) characterization of dynamic morphological changes of tin anode electrode during lithiation and delithiation processes; (2) investigation of morphological and phase changes of selenium-doped germanium compared with germanium anode; (3) gallium-based self-healing liquid metal anode with solid electrolyte for rechargeable batteries; (4) single particle characterization of germanium based anode under operational conditions.

Chapter 2 introduced a literature review of the development of lithium-ion batteries and their histories. The advantages and limitations of utilizing high capacity anode materials in lithium-ion batteries as well as the characterizations of anode materials using in situ and operando techniques regarding morphological and chemical evolutions.

Chapter 3 demonstrates the dynamic morphological evolution of tin particles during cycling processes using operando transmission X-ray microscopy. The negative feedback mechanism caused by the particle size variations and constant current applied to the system has been interpreted. The behavior of nonspherical active material has been monitor and explained as well.

Chapter 4 compares the morphological and compositional evolutions of selenium-doped germanium electrode and pure germanium anode via in-situ and operando X-ray diffraction, X-ray absorption spectroscopy, and transmission X-ray microscopy. A more homogeneous optical density and volumetric changes of selenium-doped germanium material were observed and analyzed due to the in-situ formed Li-Se-Ge network that has been validated in this study, which explains the good rate capability and cycling performance of it compared to the pure germanium anode.

To solve the pulverization and delamination problems, a gallium-based self-healing liquid metal coupled with polymer solid electrolyte has been presented herein in chapter 5. The concept of employing a low melting point anode material combined with solid electrolyte provides a strategy to solve the cracking issues caused by volumetric change during cycling. Crystalline and chemical changes were investigated by operando X-ray diffraction and transmission X-ray microscopy with energy scan demonstrate its chemical reversibility and self-healing abilities.

However, the lithium ion battery system involves truly complicated architectures and components that lead to variations and uncertainties therefore it would be difficult to extract the intrinsic kinetics and properties for the active material itself. A novel developed single particle schematic has been proposed and validated in chapter 6. By using operando transmission X-ray microscopy and in situ nanotomography, the dynamic evolution of selenium-doped germanium microparticle has been examined and presented to illustrate its outstanding performance. This method helps discover the fundamental understanding of the active material itself.

Chapter 7 contains the conclusions of this dissertation with the future works presented in chapter 8.

2. LITERATURE REVIEW

2.1 Introduction of lithium-ion batteries

In the late 20th century, the world has been facing an energy crisis in two major aspects. Preventing the overconsumption of fossil fuels and replacing electricity generation from burning coal or petroleum products with sustainable energy sources [4]. Switching ground transportations toward electrical propulsion instead of driven by combustion engines. The increased demand for electrical energy and excessive consumption of limited petroleum resources motivate research into the development of novel energy storage systems. Multiple primary batteries were invented for usage as the new energy storage devices with unsolved environmental hazards and pollutions issues when the disposal is needed. The secondary rechargeable batteries were developed thereafter and implemented into the market to satisfy the requirements of reusable batteries. The lead-acid, nickel hydride and nickel-zinc typed batteries were widely used in portable electronic devices with limitations for future applications in the 21st century due to their limited capacity, low efficiency, memory effects, which motivate people to discover a new generation of rechargeable batteries.

Although SONY was the first company to commercialize and manufacture lithium ion batteries, several previous studies provided fundamental understanding and inspiration to the creation of lithium ion batteries. Dr. M. Stanley Whittingham was the first scientist who employed the concept of intercalation reactions and proposed the idea of lithium ion battery in the 1970s [5]. A seminal discovery by the Goodenough laboratory in 1979 demonstrated and patented $LiCoO_2$ has the ability to reversibly deintercalated and re-intercalate lithium ions at relatively high potentials making it to be the cathode material in lithium ion battery [6]. The discovery of suitable anode material was more complicated. Early work on graphite and carbonaceous materials demonstrated that lithium ion can be intercalated [7] with side reactions caused by the electrolyte solvent reduction and disruption of the carbon structure [8-10]. Several studies reported the decomposition of organic electrolyte on the surface of graphite during lithiation can separate graphite and the liquid electrolyte was thereafter knows as the solid electrolyte interface. Since SONY first commercialized lithium ion battery, a tremendous number of research regarding cathode, anode, electrolyte, and separators have emerged thereafter.

The creation of lithium ion battery was revolutionary that delivers electrical energy during discharging and restore chemical energy upon charging. Comparing to the primary batteries and previous secondary batteries, lithium ion battery possesses high efficiency, energy density, and specific capacity characteristics with limited memory effect and long cycle life. These advantages enable its commercialization for the usage of portable electric devices and electrical vehicles afterward.
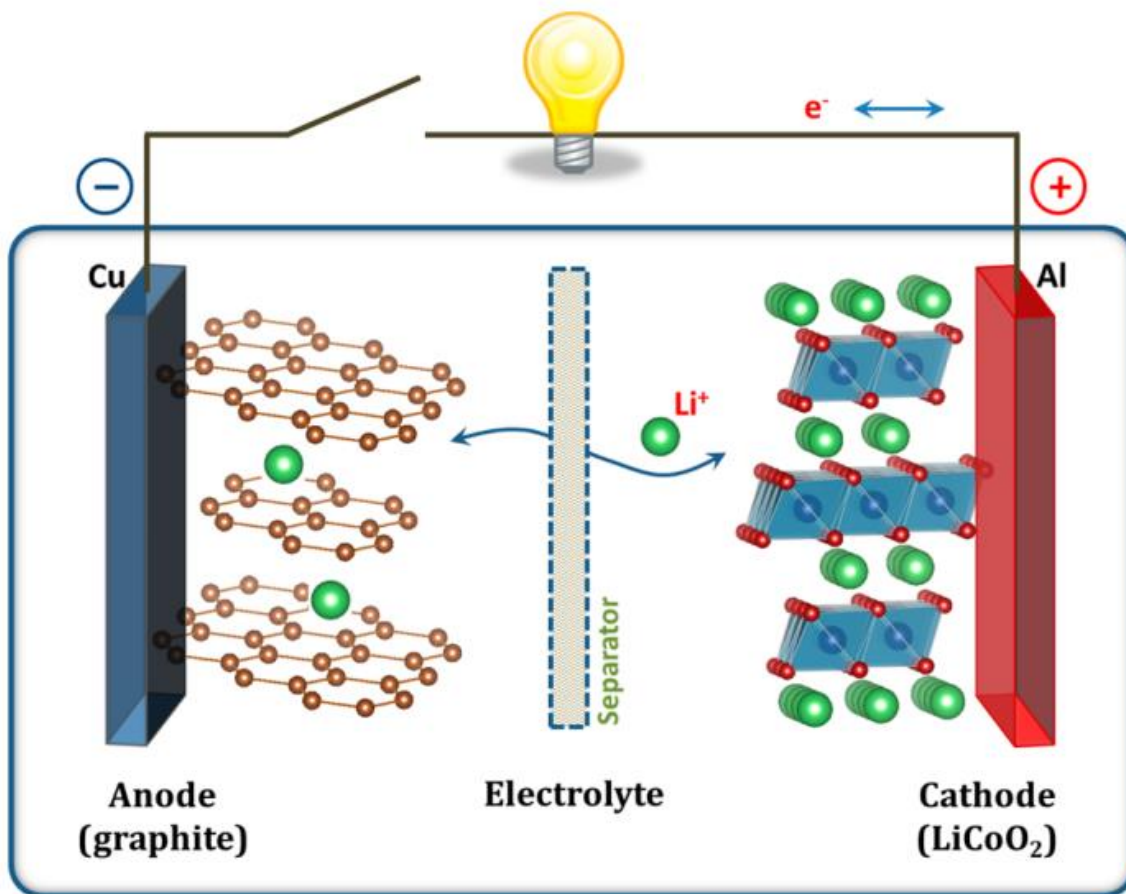
Figure 2.1 The schematic illustration of the lithium ion battery with graphite as anode and LiCoO$_2$ as cathode electrodes [11]

Figure 2.1 demonstrates the most common schematic of commercially used lithium ion battery in the current market place with graphite as anode, LiCoO$_2$ as the cathode, with separator and electrolyte in between [11]. During the process of discharging, the anode releases lithium ions and electrons. The lithium ions travel to the cathode side through electrolyte and separator subsequently intercalate into the cathode material while the electrons flow to the cathode side via

the external circuit and provide energy for different applications. These intercalation and extraction reactions are shown below:
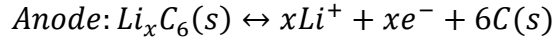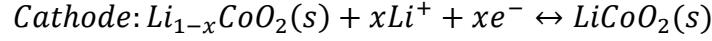
$$Cathode: Li_{1-x}CoO_2(s) + xLi^+ + xe^- \leftrightarrow LiCoO_2(s)$$
$$Anode: Li_xC_6(s) \leftrightarrow xLi^+ + xe^- + 6C(s)$$
$$\text{where } 0 \leq x \leq 1$$

In order to maintain the integrity and stability of cathode material, the amount of lithium extraction is in general limited to around 0.5 which constrains the capacity to half of its theoretical capacity by converting between $LiCoO_2$ and $Li_{0.5}CoO_2$. Although layered lithium transition metal oxides are the most common cathode materials [12], $LiCoO_2$ only delivered a reversible capacity of 160 mAh g^{-1} limits its future application due to the high cost of cobalt and low reversible capacity. $LiMnO_2$ was proposed to replace $LiCoO_2$ due to its less expensive characteristic. Even though different efforts have been made, the cycling performance of $LiMnO_2$ is still disappointing with the dissolution of Mn^{2+} into the electrolyte leads to losing active materials [13]. The dissolved Mn^{2+} transport to the anode side influences the stability of the solid electrolyte interface layer [14]. Ternary transition metal oxides include $LiNi_{1/3}Mn_{1/3}Co_{1/3}O_2$, $LiNi_{0.8}Co_{0.15}Al_{0.05}O_2$, etc. have attracted more research interests in the past few decades [15-18] with Nickle rich materials become more popular in recent years due to its lower cost and higher capacity delivered. The current limitations of Nickle rich materials include weak thermal stability and poor cycling performance [19]. Modifications strategies are necessary to address these problems [20-22]. Other commercial cathode materials such as $LiMn_2O_4$ and $LiFePO_4$ are cheaper and more environmentally friendly. $LiMn_2O_4$ is spinel structured material that could be reduced and oxidized in the nonaqueous electrolyte at high potential similar to $LiCoO_2$ with comparable capacity therefore selected for many high rate batteries for commercial applications [23]. $LiFePO_4$ has very good power capability, thermal stability, and cycle life which is mainly used in high power devices and energy storage applications with a few disadvantages include low average potential resulting in low specific energy [24].

Research for safer and stable anode materials have undergone great progress in parallel to the search for cathodes. Graphite has dominated the market for years with its low cost, high conductivity, fast lithium diffusivity, and small volume change characteristics. However, graphite

delivers a theoretical specific capacity of 372 mAh g^{-1} with low discharge potential limits its future applications [25, 26]. To solve the lithium plating issue, lithium titanate oxide was proposed and validated to has outstanding thermal stability and highly reversible zero-strain lithium intercalation and extraction mechanisms. Its high lithiation potential prevents the decomposition of electrolytes which made it extremely stable and therefore has been commercialized although sacrifices the cell voltage and capacity [27-29].

Lithium metal has been considered as one of the most promising anode materials due to its high specific capacity of 3860 mAh g^{-1} and the lowest potential among all anode materials with potential applications into lithium-sulfur and lithium-oxygen batteries [30-33]. However, the lithium metal will be plating and stripping during cycling leads to the growth of lithium dendrite due to the unstable deposition of lithium metals, consequently, resulting in short circuit and other fatal obstacles. Several methods have been reported to suppress the lithium dendrite by employing solid electrolyte or electrolyte additives but it is still challenging for commercial applications [34-37].

2.2   Group IV high capacity anode materials

The theoretical specific capacities for Group IV elements (silicon, germanium, tin) are significantly higher than graphite but decrease at higher atomic numbers making them promising anode materials. Despite the differences between their specific capacities, group IV elements suffer from pulverization of active materials and delamination from the current collector as well as the continual formation of solid electrolyte interface caused by the volume change during cycling, resulting in capacity fading [38]. The degradation mechanisms of group IV materials are shown below in **Figure 2.2** [39]. Different methods have been proposed to address this problem including surface coating, doping, and nanostructure, etc. [40-45].
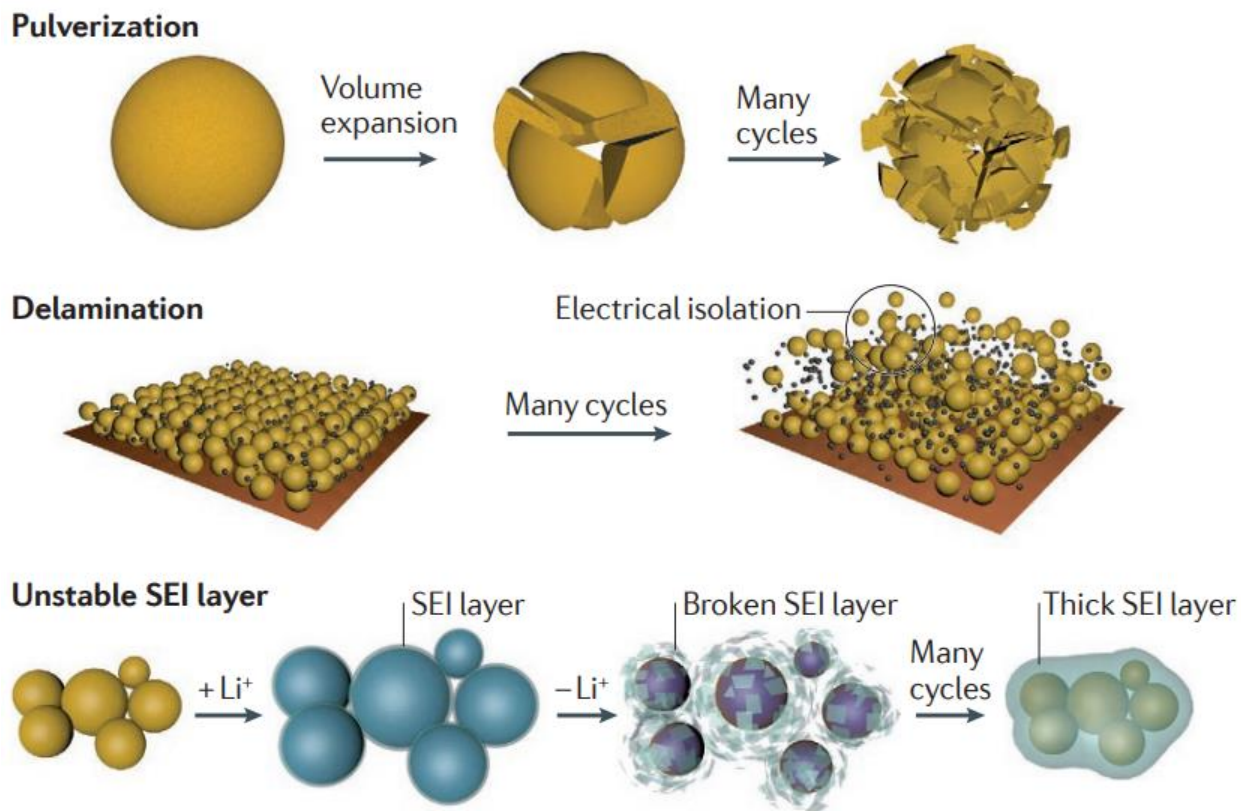
Figure 2.2 Main degradation mechanisms of group IV anodes originating from volume expansion during cycling [39]

Silicon is the most widely studied material due to its abundant, non-toxic, eco-friendly, and high specific capacity of 3579 mAh g^{-1} characteristics [46, 47]. Tremendous modification strategies have been made to address its volume expansion and poor intrinsic electron conductivity problems such as employing a physical compartment to alleviate volume expansion, synthesize nanosized silicon particles, and fabricate stress relief buffer matrix or coating techniques [48-51]. More recently, the research on the silicon anode has been expanded from its initial strategies to nanowires, nanotubes, and porous structures which significantly improve cycling performance. Although the silicon-based anodes with outstanding performance have been extensively reported, several concerns need to be addressed before being put into the market including coulombic efficiency, mass loading, and expenses. Currently, the coulombic efficiency is essential for full cell due to the limited lithium-ion resources. Normally, the initial coulombic efficiency of the silicon anodes is typically lower than graphite anode which needs further improvement while the

real mass loading of silicon was not high enough and the cost for the synthesis of nanostructured silicon is expensive making commercialization difficult [52, 53].

Comparing with silicon, germanium has 400 times faster lithium ion diffusivity and 1×10^4 times higher electronic conductivity than silicon at room temperature [54, 55]. Germanium anode possesses a high theoretical specific capacity of 1384 mAh g^{-1} (for lithiation to the $Li_{15}Ge_4$ phase) with improved lithium insertion and extraction kinetics, which is considered as a promising candidate of the anode to satisfy the increasing demand for batteries with higher energy and power density. Other than silicon, germanium may use micron-sized particles with good cycling and rate capability [56]. This advantage eliminates the excessive solid electrolyte interface that leads to the build-up of irreversible capacity and impedance. However, germanium experiences a similar volume expansion issue as silicon. To address this problem, several strategies like nanoparticles, nanowires, and porous structures were designed and examined [57-59]. These structure designs may alleviate the large volume change problem but germanium is still far from commercial application due to its high cost.

Unlike silicon or germanium, tin anode materials have drawn people's attention due to their advantages in terms of rich sources and low cost for synthesis. Despite the abundance of silicon on the earth, the synthesis of pure silicon from silica always consumes a lot of energy and may potentially pollute the environment. Also, it is rarely impossible to achieve its full capacity in practical applications for silicon. On the opposite, germanium is rare on the earth and it is difficult to find germanium minerals with high purity. Although the capacity of tin is not comparable with silicon or germanium, tin anode materials are easy to obtain with tripled specific capacity comparing with graphite making it a great contender for anode material in the next generation of lithium ion battery. In order to solve the similar volume expansion and unstable solid electrolyte interface problems as silicon and germanium experienced, people are focusing on the microstructures of tin anode since the chemical and physical properties may significantly depart from their bulk properties [60, 61]. Tin-based materials with hollow structure, mesopores, core-shell structures prevent active materials from pulverization and maintain stable structure stability [62-65]. Introducing inert components may provide the void space to accommodate their volume change but sacrifice the specific capacity due to the increase in total mass. Designing and manufacture tin-carbon is superior since the coulombic efficiency will be high in the first and following cycles and the pulverization issue will be alleviated due to the carbon coating on the

surface [66, 67]. Extensive research has demonstrated that proper modification and fabrication are the effective approaches for achieving high capacity with good cycling stability for tin, but it is still far from industrialization due to the cost and processability.

Comparing with most of the high capacity anode materials, gallium-based anodes only deliver 769 mAh g^{-1} seems not competitive [68]. But benefiting from fluidity and surface tension, gallium materials are one of the best candidates for its self-healing and fast ion diffusion abilities at room temperature. Recent studies found the construction of nanostructures such as nanoparticles, nanowires, or nanorods is considered as an effective method to improve the electrochemical performance of active materials [68-70]. Gallium confined in porous carbon has been reported to demonstrate a reversible capacity of 400 mAh g^{-1} after 100 cycles [71]. By introducing tin into gallium lattice, the melting point decreased to below pure gallium at room temperature. The combination of gallium tin alloy nanoparticles with reduced graphene oxide and carbon nanotube exhibits around 400 mAh g^{-1} at 4000 mA g^{-1} for more than 4000 cycles without an obvious decay [68]. Other gallium based anode materials including gallium selenide, gallium nitride, gallium sulfide anodes have been investigated as well [72-74], nevertheless, technical optimization and cost-related concern are still needed for the development of gallium anodes [75].

2.3   In situ and operando characterizations of battery materials

Lithium ion batteries are the most attractive technique for energy storage nowadays. However, further optimizations and improvements are still required to solve challenges such as stability and safety. Addressing these issues in the battery system requires a fundamental understanding of the reaction and degradation mechanisms when the battery is under operational condition. The synchrotron-based X-ray techniques provide insights for monitoring and studying the dynamic changes of crystal structure, chemical composition, and morphology, which benefit the comprehensive understanding of the battery system. Performing operando or in situ approaches provides advantages over ex-situ measurements. In situ experiment probe the reaction taking place at the specific time step or location of the sample providing higher precision and reliability for data analysis. The continuous measurement of a single sample under the operational condition eliminates the preparation of multiple specimens and the discrepancies caused by the different samples. Also, in situ or operando measurements may detect non-equilibrium and fast transient processes during electrochemical reactions which nearly impossible for ex-situ experiments [76-

78]. Ex-situ experiment suffers from contamination, relaxation, and irreversible changes during handing therefore the results may be affected [78]. Since the synchrotron X-ray is limited and difficult to get, ex-situ experiments are still necessary and beneficial before operando measurements. The general synchrotron-based X-ray techniques for battery research are X-ray diffraction, X-ray pair distribution function, X-ray absorption spectroscopy, and transmission X-ray microscopy. Each technique has its own capabilities and limitations. X-ray diffraction provides structure information with crystallinity, lattice parameters but impractical for amorphous materials [79-82]. The pair distribution function is highly limited and fastidious which needs careful in situ cell design [83-85]. But it is useful for atomic pair distance and local ordering to solve the structure of amorphous and disordered materials. The X-ray absorption spectroscopy is not capable to study low atomic number elements but generates information related to valence changes and local structural changes of bond length and degree of disordering [85-87]. Transmission X-ray microscopy provides a combination of morphological and structure evaluations as well as chemical information in three dimensional, but the operando cell designs are generally complicated [88-90]. Wang et al. employed chemical vapor deposition for making the in situ cell and successfully conducted the transmission X-ray microscopy measurement to investigate the morphological evolutions during cycling for tin anode [88]. Liu et al. adopted operando X-ray diffraction and X-ray absorption spectroscopy explored the correlation between manganese dissolution and the dynamic phase stability in spinel based cathode materials [91]. The phase transformation of germanium anode materials into amorphous and crystalline lithiated phases, and the effect by applying different cycling rate has been revealed by Lim et al. via operando X-ray diffraction and X-ray absorption spectroscopy [92, 93]. A similar study reported by Silberstein et al. employed the same characterization methods explored different phenomenon for germanium nanowire due to the intrinsic differences between germanium powder and nanowire as the active anodes [94]. The complicated battery system consists of cathode, anode, separator, and electrolyte with chemical variations in each component making it is even harder to analyze. The combination of different characterization techniques is essential to obtain a more comprehensive and fundamental understanding about the structural and chemical evolutions in lithium ion battery.

3. CHARACTERIZATION OF DYNAMIC MORPHOLOGICAL CHANGES OF TIN ANODE ELECTRODE DURING (DE)LITHIATION PROCESSES USING OPERANDO SYNCHROTRON TRANSMISSION X-RAY MICROSCOPY

3.1 Abstract

The morphological evolution of tin particles with different sizes during the first lithiation and delithiation processes has been visualized by an operando synchrotron transmission X-ray microscope (TXM). The operando lithium ion battery cell was operated at constant current condition during TXM imaging. Two-dimensional projection images with 40 nm resolution showing morphological evolution were obtained and analyzed. The analysis of relative area change shows that the morphology of tin particles with different sizes changed simultaneously. This phenomenon is mainly due to a negative feedback mechanism among tin particles in the battery electrode at a constant current operating condition. For irregular-shaped tin particles, the contour analysis shows that the regions with higher curvature started volume expansion first, and then the entire particle expanded almost homogeneously. This study provides insights for understanding the dynamic morphological change and the particle-particle interactions in high capacity lithium ion battery electrodes.

3.2 Introduction

Advanced lithium ion battery (LIB) technologies have been considered promising in the realization of electric vehicles because they have high energy and power density relative to other cell chemistries [95-98]. During the last decade, many research efforts have been made to develop alloy-type anode materials for LIBs, because of their much higher storage capacity compared to graphite (372 mAh g^{-1}) [99]. Tin (Sn) is one of the alloy-type materials and it has a theoretical capacity of 994 mAh g^{-1} (for the charged $Li_{22}Sn_5$ phase) [100-102]. Sn is also non-toxic, abundant, and inexpensive. However, the major challenge in the development of Sn anode is the high volumetric change (about 360%) involved in the reaction scheme, which could result in particle fracture and electrode delamination from the current collector, thereby leading to a rapid loss of specific capacity [38, 100, 103-106]. Particle fracture can be alleviated by nano-structuring the alloy-type anode materials due to the facile strain accommodation and the short diffusion path for

electron and lithium transport in the nanostructured electrodes [42, 70, 107-109]. However, nanostructured particles have low tap density and lead to lower energy density anodes, making scale-up difficult [110]. In addition, the surface area of the material increases with a decrease in particle size, which leads to a largely irreversible capacity loss due to the formation of the solid electrolyte interphase (SEI) [100]. Another approach to withstanding the massive strain in high capacity anode materials is to design composites containing both high capacity anode material and stress-accommodating phase [100]. Although the composite anode material can alleviate the particle fracture, the large volume change still exists and it is a dynamic process during the cycling of a LIB. Therefore, it is essential to understand the dynamic morphological change of Sn electrodes in LIB cycling processes.

To this end, several in situ studies have been conducted to investigate the morphological change of Sn electrodes. For instance, Ebner et al. used X-ray tomography to visualize and quantify the origin and evolution of electrochemical and mechanical degradation of the tin oxide electrode [111]. Sun et al. used in situ synchrotron radiography to investigate the lithiation and delithiation mechanisms of multiple Sn particles in a customized flat radiography cell [112]. Wang et al. studied the microstructural change of a Sn electrode using in situ synchrotron X-ray nano-tomography [88]. Recently, Zhou et. al. reported the evolution of the microstructure of a single Sn particle battery using in situ focused-ion beam scanning electron microscopy [105]. These in situ and operando studies have revealed the dynamic morphology and microstructure change of Sn particles. However, the real LIB electrodes are composed of Sn particles with different sizes and shapes, and the electrochemical performance of the whole cell is on the multiple-particle scale. We hypothesize that the interaction between particles and the shape irregularity of the particle could affect the dynamic morphological change of Sn particles. The single particle study and the homogeneous electrode assumption (same particle size and spherical shape) cannot help to test this hypothesis.

Therefore, the objective of this paper is to investigate the morphological evolution of a Sn electrode made of particles with different sizes and shapes. We want to answer the following two questions in this paper. (1) Does the morphology of Sn particles with different sizes change simultaneously? (2) Does an irregular-shaped Sn particle have a homogeneous morphology change? In this work, we studied the morphological evolution of Sn electrodes via operando synchrotron transmission X-ray microscopy (TXM) at the Beamline 8-BM-B of Advanced Photon Source

(APS) which is operated by the National Synchrotron Light Source-II (NSLS-II) through an NSLS-II transition program. Two-dimensional (2D) projection images of Sn particles in the Sn electrode were obtained and analyzed to study the effect of particle size and shape on the dynamic morphological change during the lithiation and delithiation processes. Ex-situ X-ray diffraction (XRD) was implemented to monitor the crystalline change and the XRD results were used to interpret the morphological evolution data.

3.3 Experimental section

3.3.1 Materials

Sn powder (Sn, 10 µm, 99% trace metals basis, Sigma-Aldrich), super C65 conductive carbon black (Timcal Co., Ltd.), polyvinylidene fluoride binder (PVDF, 12 wt.%, Kureha Battery Materials Japan Co., Ltd.), 1-methyl-2-pyrrolidinone (NMP, anhydrous 99.5%, Sigma-Aldrich), 1M $LiPF_6$ electrolyte in 1:1 volume ratio mixture of ethylene carbonate and dimethyl carbonate solution (BASF Corporation), pyrolytic graphite sheet as the current collector (MTI Corporation), lithium ribbon (thickness of 0.38mm, 99.9% trace metals basis, Sigma-Aldrich) were purchased from commercial corporations and utilized as received.
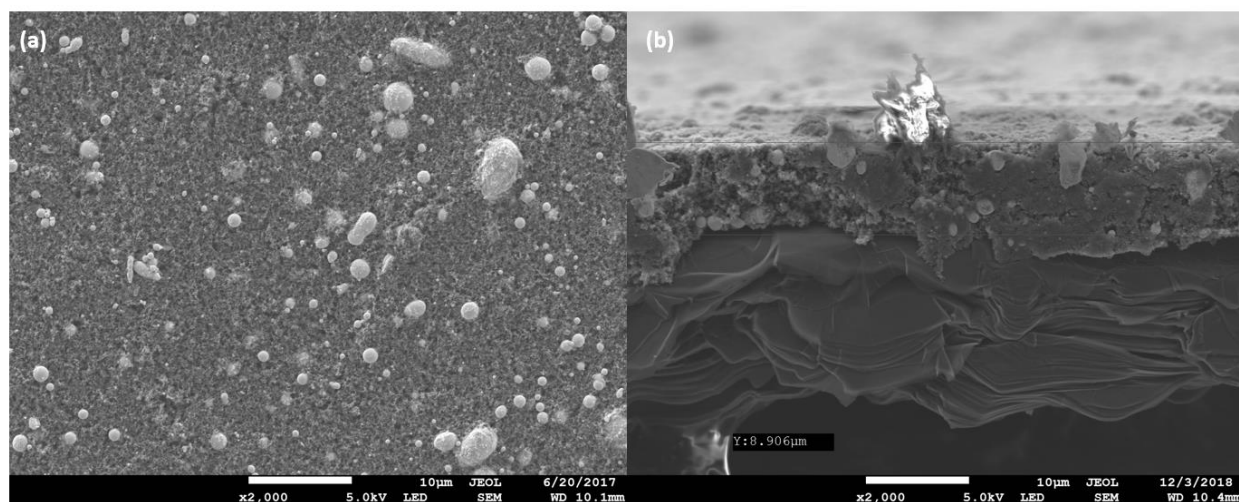
Figure 3.1 SEM images for (a) the top surface and (b) the cross-section of a Sn electrode. The Sn electrode was fabricated from a 25:45:30 (weight%) mixture of Sn, carbon black, and PVDF. The scale bar is 10 µm.

3.3.2 Preparation of Sn electrode

To investigate the morphological and phase change of Sn particles, Sn electrodes for TXM and XRD were fabricated from a 25:45:30 (weight%) mixture of Sn, carbon black, and PVDF. A low percentage of Sn was used to avoid the overlaps of Sn particles during TXM imaging. The mixture was added to the NMP solution and mixed homogeneously by a magnetic stir bar in a vial for 20 h. The gel-like slurry was coated onto a thin pyrolytic graphite sheet via a film casting doctor blade (EQ-Se-KTQ-100, MTI, Richmond, CA, USA). The graphite sheet was used as the current collector to avoid strong X-ray absorption from the current collector during TXM imaging. The electrode was dried at 100 °C in a vacuum oven for 12 h. As shown in **Figure 3.1a**, Sn particles were uniformly distributed, and the particle size was between 1 to 10 µm. The thickness of the Sn electrode is about 9 µm as shown in **Figure 3.1b**. Circular discs with 1.11 cm in diameter were cut out of the Sn electrode film for cell assembly. The mass loading of Sn on the graphite current collector is approximately 0.3 mg cm^{-2}. All the cut Sn electrodes were stored in an argon-filled glove box.

3.3.3 Coin cell assembly and electrochemical evaluation

CR2032 coin cells were modified and used in this study. Briefly, 2 mm diameter holes were punched at the center of the anode and cathode cases. 30 µm thick Kapton tape was used to seal the hole on both sides of the case. The cells were assembled in an argon-filled glovebox (under $O_2 < 0.1$ ppm, $H_2O < 0.1$ ppm; Unilab 2000, Mbraun, Stratham, NH, USA) as shown in **Figure 3.2a**. First, a Sn electrode was placed on the anode case with the graphite side facing down, followed by adding 15 µL electrolyte. A Celgard 2400 separator was placed on top of the Sn electrode and another 15 µL electrolyte was added on top of the separator. Then a piece of lithium metal (1.27 mm in diameter) was placed on the separator. Finally, a stainless-steel plate (with a 2 mm hole at the center) covered the lithium metal with a spring as the spacer. The cell was crimped and taken out of the glove box for electrochemical evaluation.

The operando coin cell was galvanostatically cycled from open circuit potential to 0.01 V at 0.1 C during the first lithiation, at 0.05 C for the second lithiation, and from 0.01 to 1.2 V at 0.1 C for delithiation using an Arbin 2000 battery cycler. The second 0.05 C lithiation was implemented because no morphological changes were detected by the TXM at the end of the first 0.1 C lithiation.
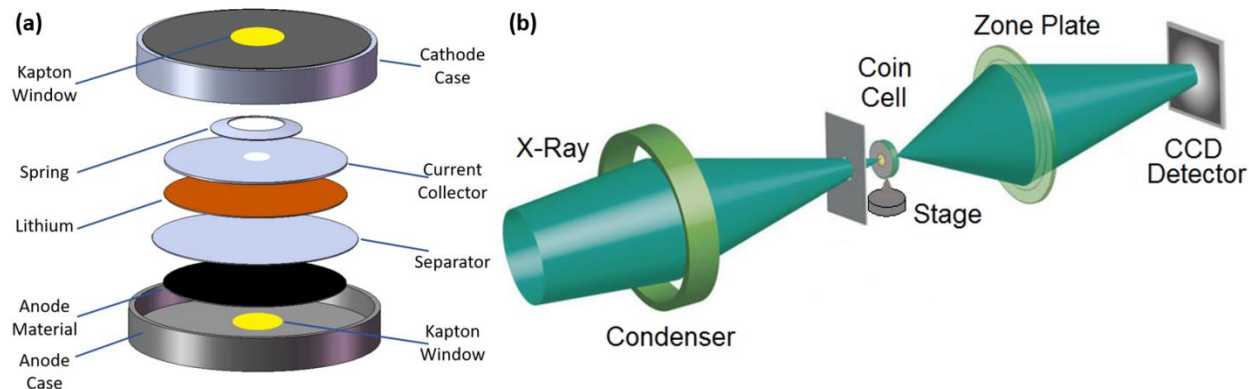
Figure 3.2 Schematics of (a) the operando coin cell assembly and (b) the synchrotron transmission X-ray microscopy setup.

3.3.4   Operando transmission X-ray microscopy

Transmission X-ray microscopy is a non-destructive technology to perform nano-imaging. The synchrotron TXM with a large field of view of 40 µm by 40 µm at 40 nm pixel size was employed in this study. This TXM hosted on beamline 8-BM at APS was operated by NSLS-II through an NSLS-II transition program. The 2D operando TXM images were consecutively collected to visualize and quantify morphological changes of Sn particles under operating conditions. We employed a 10 min time interval for data acquisition. Ten different positions were collected consecutively with an exposure time of 3 s for each capture. During the image collecting process at each position, 10 images were captured and averaged to improve accuracy. The overall image collection took 5 min and we adopted a 5 min gap between each series of acquisitions. The schematic of the TXM is shown in **Figure 3.2b**.

3.3.5 X-ray diffraction

An ex-situ XRD measurement was performed on a Bruker D8 Discover XRD instrument equipped with Cu Kα radiation at the Integrated Nanosystems Development Institute (INDI) with a photon wavelength of 1.5406Å. Each coin cell to be measured was cycled to a specific voltage. Electrodes were obtained by dissembling the coin cells. The cycled electrodes were rinsed with diethyl carbonate solution, dried under vacuum for 30 min, and sealed in Kapton tape. We measured 2θ from 20 ° to 60 ° with an increment of 0.02 ° for the XRD experiment. The exposure time for each increment was 0.5 s. The XRD data were calibrated using the corundum standard and analyzed via DIFFRAC.EVA software.

3.3.6 Image processing

Image processing was conducted via a commercial software Avizo®. Motion artifacts were observed in the operando experiment due to the movement of the sample during the measurement, such as volume expansion or shrinking of active materials and tilted of the electrode during the data acquisition. Hence, image filtering was employed as the first step in image analysis. All the grayscale images in this work were subject to non-local means filtering to remove noise and blur due to its high efficiency at noise removal [113], followed by a register image algorithm in Avizo®. Image registration is the process to transform different sets of images into one coordinate system based on the gravitational center and contour lines for conducting further analysis.

3.4 Results and discussion

The voltage profile of a Sn cell is shown in **Figure 3.3a**. The Sn electrode was lithiated twice at different C rates (0.1 C and 0.05 C) in order to achieve full lithiation. **Figure 3.3b** shows a series of TXM images at one of the ten positions during the first cycle. As shown in **Figure 3.3b**, the entire electrode had a clear deformation during the first cycling process. The electrode moved to the left side during the first 0.1 C lithiation and reached a 4 µm movement. At the end of the second 0.05 C lithiation, the electrode moved an additional 5 µm to the left. Before the delithiation process, the 9 µm movement was calibrated so that all the particles have their original positions. The electrode moved to the opposite direction during delithiation and a 4 µm movement was achieved at the end of delithiation. It was noticed that the first 4 µm movement might potentially

due to the sample holder shift during motion. However, the movement during the second lithiation is larger within a shorter period of time which indicates that the movement is mainly due to the volume change of Sn particles while the sample holder shift during the data acquisition has minor influences.
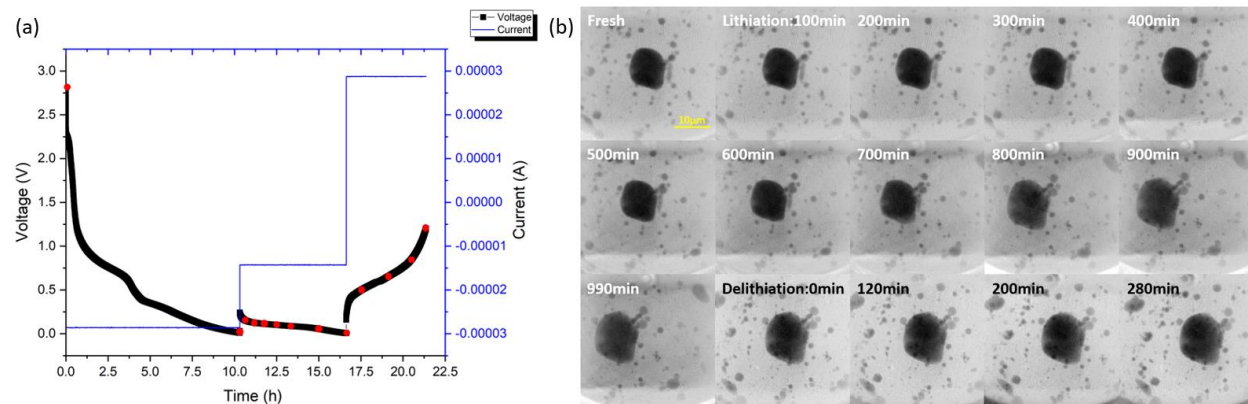
Figure 3.3 (a) Voltage and current profiles of an operando Sn cell. (b) TXM images at one of the ten positions during the first cycling process showing the movement of the electrode during lithiation and delithiation processes (as indicated in white during lithiation and black for delithiation) caused by electrode deformation and sample holder shift. The scale bar is 10 µm.

At the ten positions for imaging, several hundreds of particles with different sizes have been monitored by the operando TXM. Less than 3% of the particles don't have any volume change during the first cycle. We believe that the main reason is the loss of electrical connection for those particles. Among the active particles, 4 particles at different positions with different sizes were selected to evaluate the effect of size on the dynamic morphological changes. In order to eliminate the effect of shape, spherical particles were selected. The largest one is not spherical because there was no spherical one at this size.
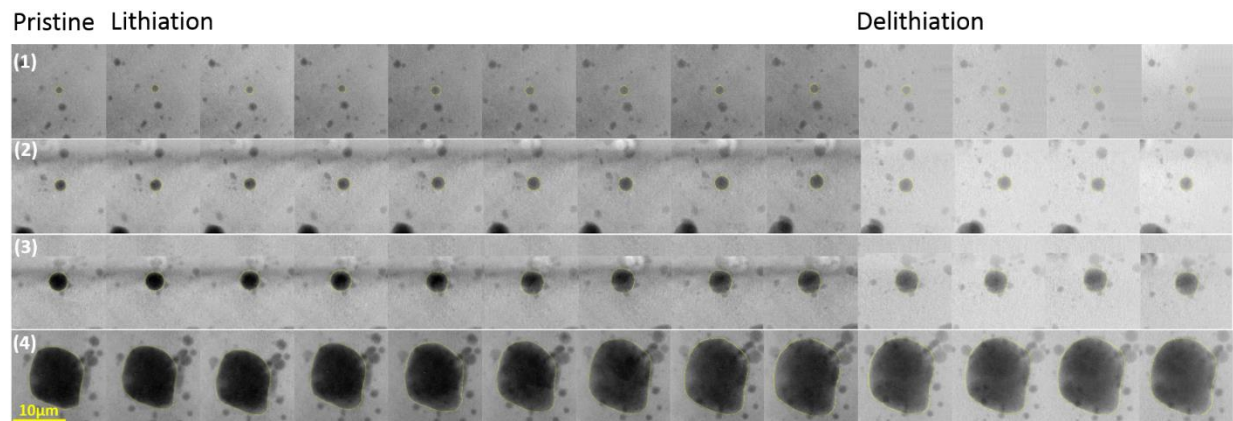
Figure 3.4 Corresponding TXM images for the selected particles at the time steps highlighted in Figure 3.3a.

As shown in **Figure 3.4**, the original sizes are 1 µm, 2 µm, 3.4 µm, and 10 µm in diameter or area equivalent diameter in pristine condition. The contours in these selected particles demonstrate the area change of the projection images during the first cycling process. The relative area which stands for the ratio between the current area to its original area was measured via contour analysis in ImageJ based on the intensity gradient of each specific image. The particles have relatively smooth contours and a 150% overall 2D area expansion (on average) was achieved at the end of the 0.05 C lithiation as shown in **Figure 3.5**. At the end of the first delithiation, the particles shrink around 10% and they are not able to recover their original sizes. The reasons could be the formation of nanopores inside the particle [105, 114-116] during delithiation and the loss of electronic connection [110, 117, 118].
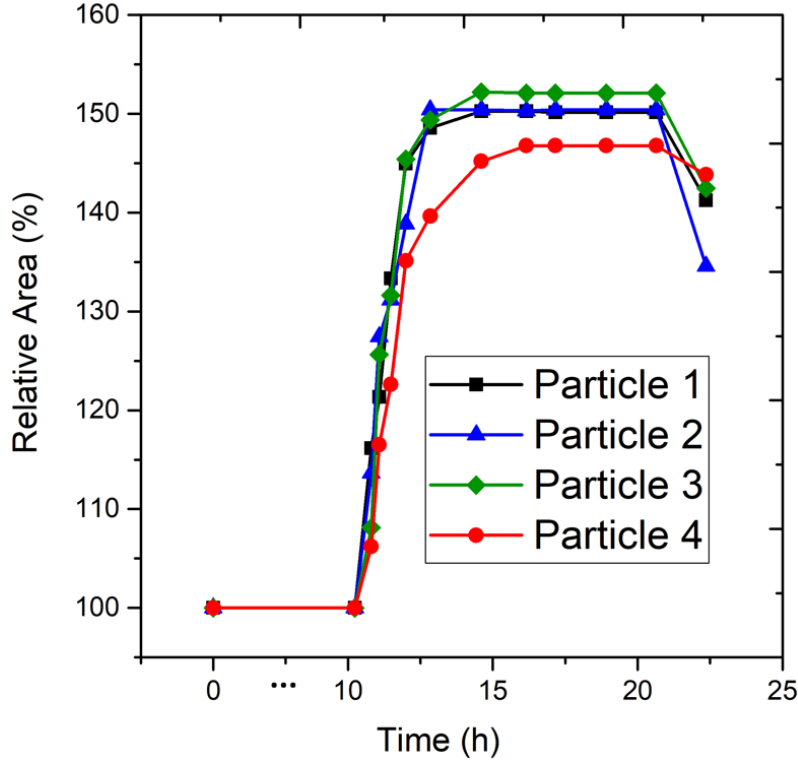
Figure 3.5 Dynamic two-dimensional area evolution calculated from the projected TXM images for the selected particles.

It was observed that regardless of particle size, volume expansion occurred simultaneously which is different from the phenomenon observed by Chao et al. [114, 119]. They found that the smaller Sn particles expand at a much faster pace than the larger particles. The major difference between the two operando experiments was the lithiation process after the first constant current lithiation. Chao et al. did not observe the volume change at the end of the first constant current lithiation. Then a constant voltage lithiation at 0.001 V was implemented. In our case, the second lithiation is still constant current. This phenomenon can be explained by the negative feedback mechanism proposed by Yan et al. [120]. As shown in Eq.1, lithium ion intercalation reaction across the interfaces of electrolyte and Sn particles can be determined by the Butler-Volmer equation:

$$J^{\text{Li}} = \frac{J}{F} = \frac{i_0}{F}\left\{\exp\left(\frac{\alpha F}{RT}\eta\right) - \exp\left[-\frac{(1-\alpha)F}{RT}\eta\right]\right\} \qquad (1)$$

where J^{Li} and J are the reaction flux of lithium ion and reaction current density respectively, R is the universal gas constant, T is absolute temperature, F is Faraday's constant, i_0 is the exchange

current density, η is the surface overpotential, and α is a symmetry factor that represents the fraction of the applied potential promoting the cathodic reaction, α is 0.5 for the electrochemical reaction in LIBs. The overpotential η is defined as below:

$$\eta = \emptyset_1 - \emptyset_2 - U_{OCP} \qquad (2)$$

where $\emptyset_1$ and $\emptyset_2$ are the potential of Sn particles and electrolyte at the interface respectively, and U_{OCP} is the open circuit potential (OCP) at the interface. It should be noted that the overpotential is a negative value during lithiation and a positive value during delithiation.

If the battery is cycled at a low rate, such as 0.1 C and 0.05 C, we can assume that the exchange current density i_0 is constant at the Sn particle/electrolyte interface for all the particles in the electrode. Then the lithium ion intercalation rate on the surface of Sn particles is determined by the overpotential η. Due to the low rate cycling, high electronic conductivity of Sn, and high ionic conductivity of the electrolyte, we also can assume that both $\emptyset_1$ and $\emptyset_2$ have very small spatial variation in the electrode and the value of $\emptyset_1$ - $\emptyset_2$ is the same for all the Sn particles in the electrode. Therefore, the difference of lithium intercalation rate on the surface of different Sn particles in the electrode is only determined by the OCP. The OCP is determined by the lithium ion concentration on the surface of Sn particles. As shown in the literature [88, 100, 121-123], the OCP of Sn decreases when the lithium concentration increases on the surface. During a constant current lithiation, the value of $\emptyset_1$ - $\emptyset_2$ also decreases to keep a certain overpotential for the constant current. If we assume that the lithium concentration on the surface of smaller Sn particles increases faster than it on the surface of larger particles at the beginning of the lithiation process, the higher lithium concentration on the surface of smaller particles causes smaller OCP. According to Eq. 2, overpotential decreases when OCP decreases assuming all the Sn particles have the same $\emptyset_1$ - $\emptyset_2$, which leads to a lower intercalation rate. The lower intercalation rate slows down the lithium concentration increase on the surface. At certain lithium concentration level, OCP = $\emptyset_1$ - $\emptyset_2$ and the overpotential could be zero, which completely stops the intercalation reaction. This is a negative feedback mechanism caused by the interaction among heterogeneous particles in the electrode. However, if the battery cell is operated at constant voltage mode, the value of $\emptyset_1$ - $\emptyset_2$ almost does not change as the lithiation process proceeds. The interaction of particles does exist, and all the particles react at their own pace. The smaller particles proceed faster due to their larger surface to volume ratio. However, the negative feedback mechanism could be invalid at high

current rates. A high current rate means fast electron and lithium ion transport, which can cause large polarization and large lithium ion concentration differences in the electrode. We cannot assume that i_0 (the exchange current density), $\emptyset_1$ and $\emptyset_2$ (the potential of Sn particles and electrolyte at the interface) have very small spatial variation in the electrode with large polarization and lithium ion concentration difference. According to Eqs. 1 and 2, the dynamic volume change of the particles is related to the local environment of the particle.
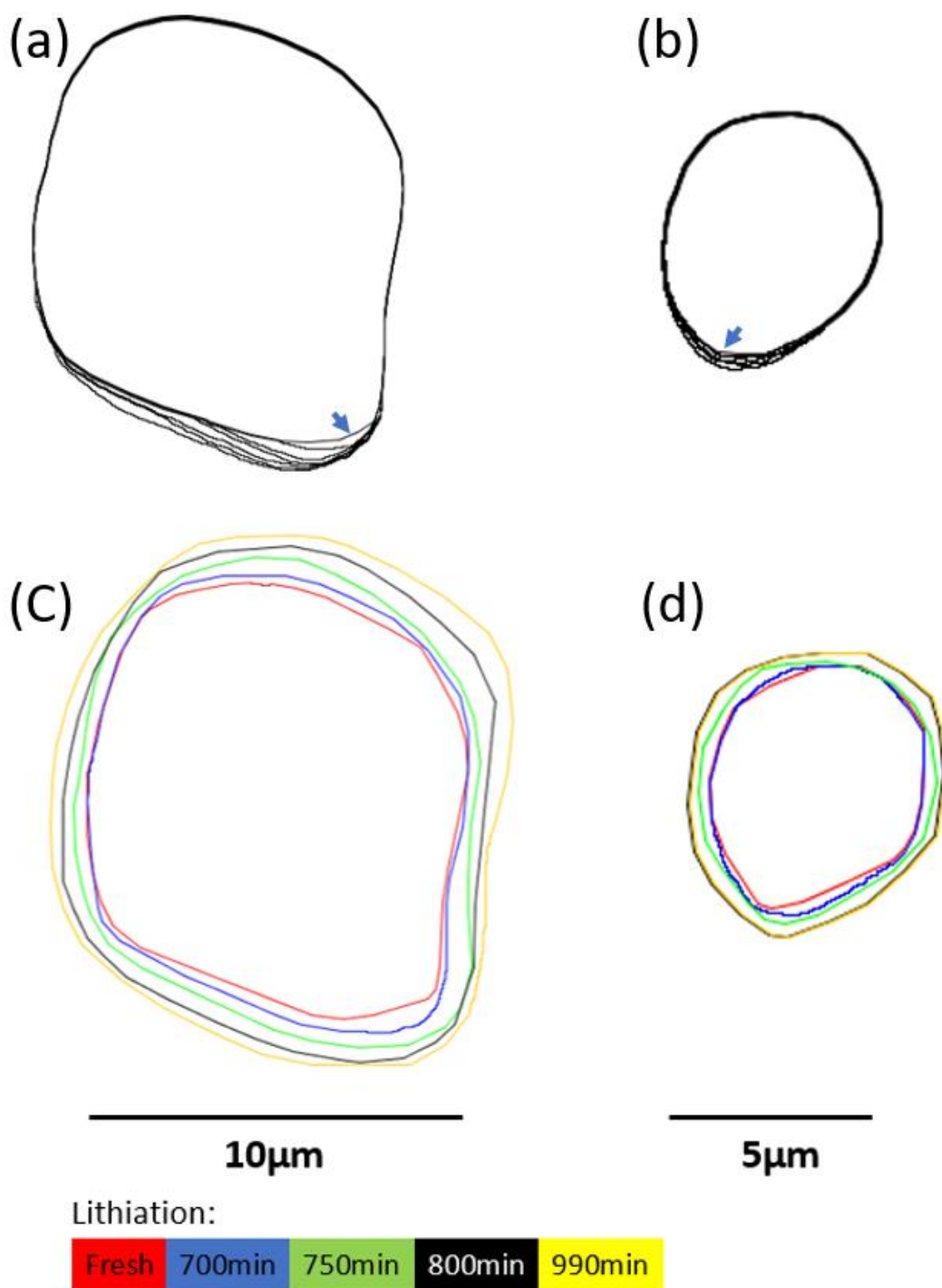
Figure 3.6 Contour plots for two selected Sn particles (a,b) during the first 50 min of volume expansion and (c,d) at the specified time steps during the lithiation process. The arrows in a and b point to the expansion direction.

To investigate the effect of shape on the dynamic morphological change of Sn particles, the curvature related analysis was performed in Avizo® by registering all contour plots into the same coordinate via the combination of contour line and gravitational center. The contours from the 2D operando images in **Figure 3.6a-b** display the dynamic changes during the first 50 min when the volume expansion occurred. The increment between each time step was 10 min. The arrows are pointing to the direction of volume expansion. It reveals that the volume expansion of irregular-shaped Sn particles is more likely to take place at the surface with higher curvature and more details can be found in the video in the supplemental document. We believe that this phenomenon was caused by a slightly higher bulk lithium concentration at the sharp locations. Volume change is mainly determined by the average bulk lithium concentration, not by the surface lithium concentration. The negative feedback mechanism is still valid in different regions of a single particle. The difference between the single particle case and the multiple particle case is the transport of lithium. Lithium can move inside a single particle but cannot move between particles during the lithiation or delithiation processes. Although the lithium concentration should have a small variation on the surface of a single particle, the region with higher curvature will have a larger average bulk lithium concentration, which causes earlier expansion, as shown in **Figure 3.6a-b**.
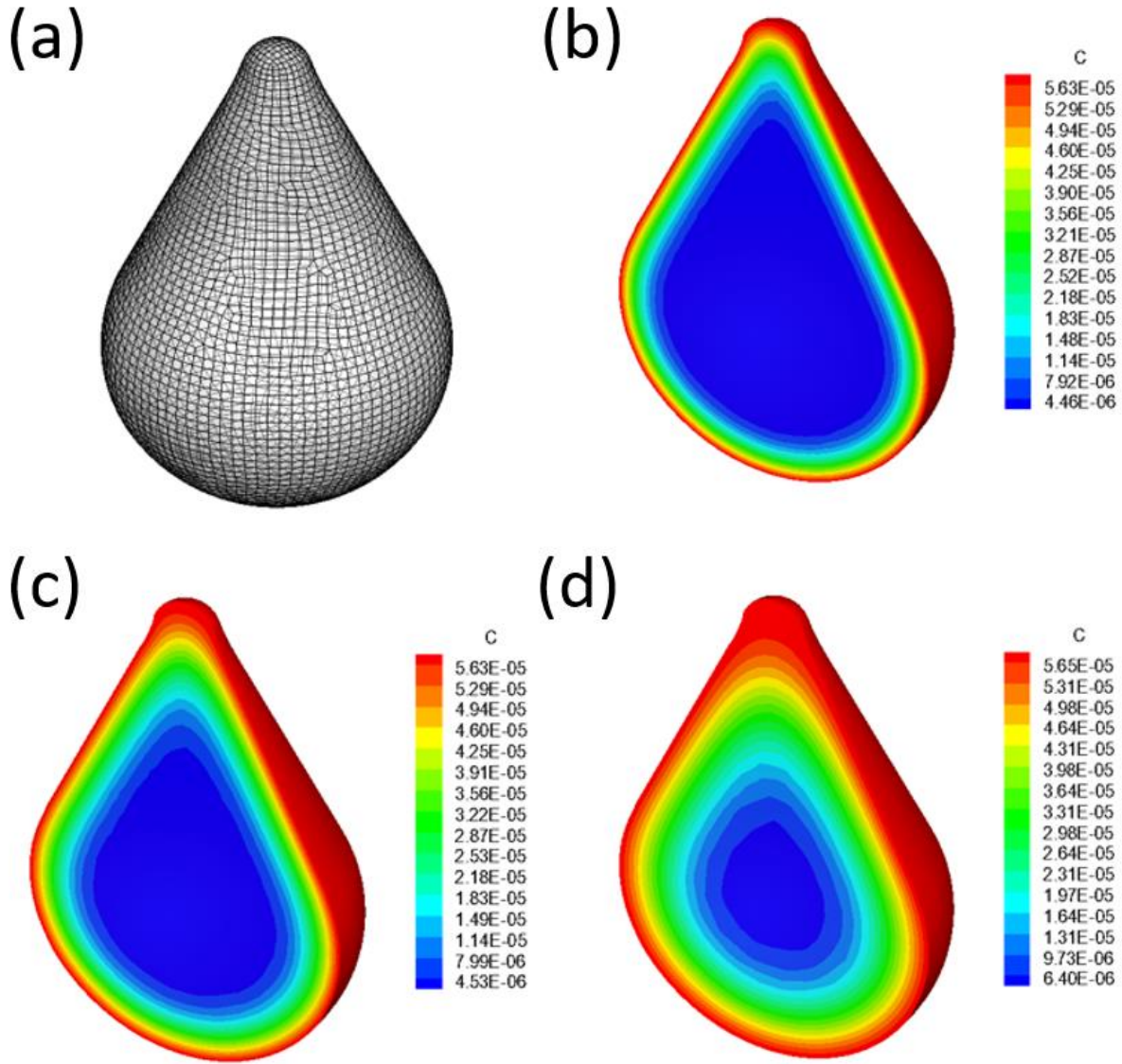
Figure 3.7 (a) Mesh of a water drop-shaped particle and (b-d) lithium ion concentration distribution at 200s, 400s, and 1000s, respectively.

To further explain this phenomenon, we conducted a numerical simulation on lithium transport in a water drop-shaped particle mesh as shown in **Figure 3.7**. The radius of the small curvature end of the particle is 5 µm (0.2 µm^{-1} curvature) and that of the large curvature end is 1 µm (equivalent to 1 µm^{-1} curvature). The finite element method (FEM) is employed to simulate the concentration distribution with time. The diffusivity is 1.0e-9 mm^2 s^{-1}. The time step for the simulation is 2 s. The initial lithium ion concentration is 1.0e-6 mol mm^{-3}. The fixed lithium ion concentration of 5.98e-005 mol mm^{-3} is imposed on the surface of the particle. The lithium ion

diffuses from the surface to the center because of the concentration difference. As shown in **Figure 3.7b-d**, the average bulk lithium ion concentration increases much faster in the large curvature end than it does in the small curvature end, which explains that the large curvature end expands earlier. **Figure 3.6c-d** displayed the contour line of the selected particles at five specific time steps during the lithiation process as indicated in the color bar. After the region with high curvature expanded, it was observed that the entire particle expanded thereafter. Supplementary dynamic videos related to this project are able to provide upon request.
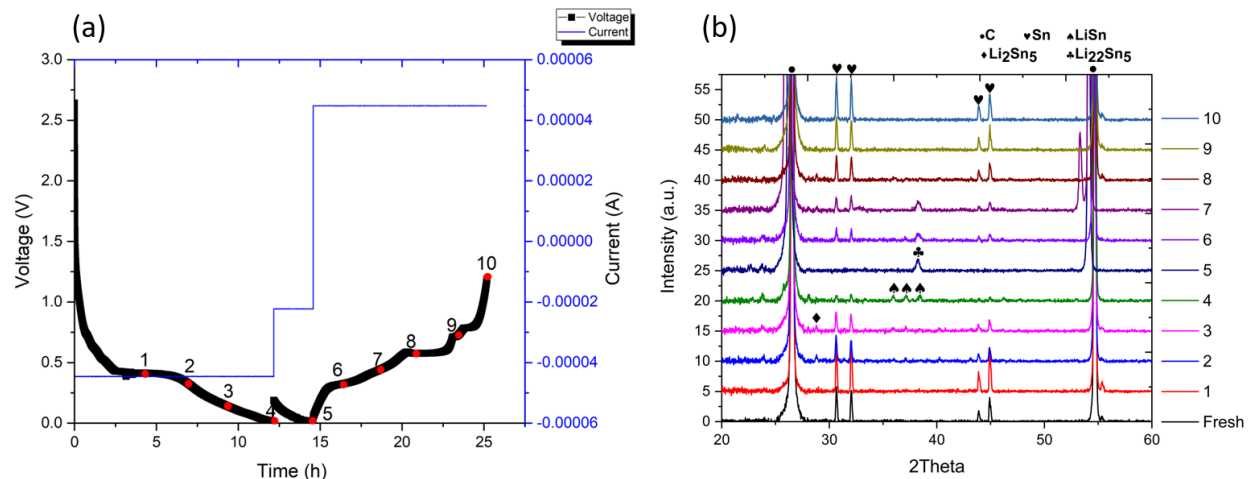
Figure 3.8 Voltage and current profiles of an ex-situ Sn cell and (b) the corresponding XRD patterns at the time steps shown in (a).

An ex-situ XRD experiment was performed to monitor the dynamic crystalline changes during the first cycle. The states of charge at which the XRD data were collected were depicted on the voltage profile shown in **Figure 3.8a**. In this XRD experiment, we applied 0.1 C and 0.05 C for lithiation and 0.1 C for delithiation during the first cycle to duplicate the same situation as the operando TXM experiment. As shown in **Figure 3.8b**, we observed that the lithiation and delithiation processes of Sn particles complied with the following sequence:

$$Sn \rightarrow Li_2Sn_5 \rightarrow LiSn \rightarrow Li_{22}Sn_5 \rightarrow LiSn \rightarrow Sn \qquad (3)$$
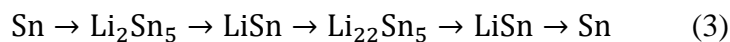
When the cell voltage reaches the first plateau at 0.56 V (DP1), the Sn phase starts to vanish and a crystalline Li_2Sn_5 phase is formed. LiSn was observed at the end of the 0.1 C lithiation, but the $Li_{22}Sn_5$ phase was not observed. Since the LiSn phase (51%) has a relatively smaller volume expansion than the $Li_{22}Sn_5$ phase (260%), this result verifies why the operando TXM experiment did not show clear morphological change after the first 0.1 C lithiation. During the second 0.05 C

38

lithiation, the Sn particles were lithiated to the $Li_{22}Sn_5$ phase. During the 0.1 C delithiation process, the XRD results show that the $Li_{22}Sn_5$ phase disappears and the Sn phase reappears at the end of delithiation. These ex-situ XRD results are in accord with the in situ synchrotron XRD data of the Sn electrode acquired during the first lithiation-delithiation cycle shown in Ref [114]. As shown in **Figure 3.5**, most of the Sn particles did not recover their original size after delithiation, which is not in accord with the ex-situ XRD results. The reasons could be the formation of nanometer-sized pores during delithiation [105, 114-116] and the loss of electrical connection [110, 117, 118].

3.5   Conclusion

In this work, the dynamic morphological evolution of Sn particles during lithiation and delithiation processes was investigated using an operando synchrotron TXM imaging technique. The relative area analysis based on the operando 2D TXM images demonstrates that all the active Sn particles expanded simultaneously with almost the same pace regardless of particle size if the battery cell is operated at constant current mode. This phenomenon is due to a negative feedback mechanism in a heterogeneous battery electrode. If the particle shape is not spherical, the contour analysis results show that the regions with higher curvature in a single particle start volume expansion first at the very beginning of the volume change process. After that, the entire particle expanded almost homogeneously.

4. IN SITU AND OPERANDO INVESTIGATION OF DYNAMIC MORPHOLOGICAL AND PHASE CHANGES OF A SELENIUM-DOPED GERMANIUM ELECTRODE DURING (DE)LITHIATION PROCESSES

4.1 Abstract

To understand the effect of selenium doping on the good cycling performance and rate capability of $Ge_{0.9}Se_{0.1}$ electrode, the dynamic morphological change, and phase transformation of Ge and $Ge_{0.9}Se_{0.1}$ electrodes were investigated by synchrotron-based operando transmission X-ray microscopy (TXM) imaging, X-ray diffraction (XRD), and X-ray absorption spectroscopy (XAS). The TXM results show that the 3D morphology of the $Ge_{0.9}Se_{0.1}$ particle preserves its original shape after the large volume change induced by the (de)lithiation. $Ge_{0.9}Se_{0.1}$ also behaves a more sudden morphological and optical density change than pure Ge during the first lithiation. The difference between $Ge_{0.9}Se_{0.1}$ and Ge is attributed to a super-ionically conductive Li–Se–Ge network formed inside $Ge_{0.9}Se_{0.1}$ particles, which contributes to fast Li-ion pathways into the particle, nano-structuring of the Ge, as well as buffering the volume change of Ge. The XRD and XAS results confirm the formation of the Li–Se–Ge network and reveal that the Li–Se–Ge phase forms at the early stage of lithiation and is an inactive phase. The Li–Se–Ge network also can suppress the formation of the crystalline $Li_{15}Ge_4$ phase. These in situ and operando results reveal the effect of the in situ formed, super-ionically conductive, and inactive network on the cycling performance of Li-ion batteries and shed light on the design of high capacity electrode materials.

4.2 Introduction

Germanium (Ge) has been considered a promising anode active material for high energy density Li-ion batteries (LIBs)[124, 125], due to its high capacity, low voltage, fast Li diffusion, and high electrical conductivity. Similar to other high capacity anode materials, such as silicon (Si) and tin (Sn), Ge electrodes experience large volume changes in the Ge particles during (de)lithiation processes. The repeated large volume change causes particle fracture and electrode delamination from the current collector, thereby leading to a rapid loss of specific capacity. Recently, particle fracture has been alleviated by nano-structuring the alloy-type anode materials, such as Ge, Si, and Sn, due to the facile strain accommodation and the short diffusion path for

electron and Li transport in these nanostructured electrodes[42, 126-129]. However, nanostructured particles have not become commercially relevant due to their high cost, solid electrolyte interface (SEI) issue, and difficulty for scale up[110, 130]. Another approach to withstanding massive strain in high capacity anode materials is to design composites containing a high capacity anode material and a stress-accommodating phase[130]. For instance, Klavetter et al. have shown that μm-sized selenium (Se)-doped Ge particles vastly outperform un-doped Ge particles of similar size in their cycling stability and rate capacity[131]. These results demonstrate the possibility to develop commercially relevant anode materials that can be cast into films with high energy density and cycling stability. It has been hypothesized that the super-ionically conductive inactive phase (Li-Se-Ge) buffers the volumetric change of the active phase (Ge) and increases the rate of Li diffusion during (de)lithiation processes. However, the effect of the active/inactive mixed phases on the mechanical stability of the $Ge_{0.9}Se_{0.1}$ electrode is still elusive. The objective of this paper is to investigate the dynamic morphological evolution and crystalline phase transformations of $Ge_{0.9}Se_{0.1}$ particles during (de)lithiation processes and reveal the effect of the active/inactive mixed phases.

Recently, synchrotron transmission X-ray microscopy (TXM) [89, 132-138], X-ray diffraction (XRD) [92-94, 139], and X-ray absorption spectroscopy (XAS) [92-94, 139] technologies have been utilized to characterize the dynamic morphological and phase changes of high capacity LIB anode materials during (de)lithiation processes. There are several reports which focus on Ge electrodes. For instance, Weker et al. used 44 nm resolution two-dimensional (2D) TXM to observe the volume change and degradation of μm-sized Ge particles during the first two cycles[137]. Lim et al. carried out a combination of operando XRD and XAS to investigate the phase transformations of Ge anodes[92]. They found that crystalline $Li_{15}Ge_4$ is the final lithiation product and the cycling process is between amorphous Ge and crystalline $Li_{15}Ge_4$ after the first cycle. They also studied the effect of cycling rate on Ge phase transformation during the first cycling process. Silberstein et al. studied the phase transformations within Ge nanowires throughout the course of LIB cycling using operando XRD and XAS[94]. They identified more crystalline Li_xGe phases during the cycling process and revealed that amorphous regions within germanium nanowires are preferentially lithiated before crystalline regions.

In this study, we investigated the dynamic morphological change of Ge and $Ge_{0.9}Se_{0.1}$ electrodes during (de)lithiation processes using a combination of 2D operando TXM imaging and

3D in situ TXM tomography. In addition, we carried out operando XRD and XAS to study the dynamic phase transformation of the $Ge_{0.9}Se_{0.1}$ electrode. Synchrotron TXM was implemented for both Ge and $Ge_{0.9}Se_{0.1}$ electrodes under 11.2 keV X-ray at beamline 32-ID-C of the Advanced Photon Source (APS). In situ 3D tomography with 77.6 nm pixel size was implemented at three statuses in the first cycle including pristine, lithiated, and delithiated status, and operando 2D imaging with 38.8 nm resolution was implemented between those three conditions. The Operando XRD experiment was conducted at beamline 11-ID-C of the APS and the operando XAS experiment was conducted at beamline 20-BM of the APS. With the in situ and operando results, the morphological and phase evolutions of Ge and $Ge_{0.9}Se_{0.1}$ electrodes were analyzed and compared. The combination of 2D operando imaging, 3D in situ tomography, and operando XRD and XAS provide new insight into the effect of the active/inactive mixed phases on the mechanical stability of the $Ge_{0.9}Se_{0.1}$ electrode.

4.3   Experimental section

4.3.1   Design of the in situ TXM battery cell

An in situ battery cell was designed to monitor morphological changes of LIB electrodes by employing synchrotron TXM. For the in situ 3D TXM tomography and operando 2D TXM, the cell has to satisfy the following requirements; 1) there are no obstacles to block X-ray through all directions of the targeted material, 2) the targeted material absorbs a sufficient amount of X-ray to be distinguished from the background, 3) Non-targeted components (cell housing, current collector, and electrolyte) are required to have less X-ray absorption through all directions, 4) the battery cell works properly under a high energy X-ray exposure on the TXM stage. **Figure 4.1a** depicts an in situ battery cell. For TXM capturing, a 5 μm thick working electrode (Ge or $Ge_{0.9}Se_{0.1}$) is coated on a carbon wire (Diameter = 30 μm) which is enclosed in the liquid electrolyte with a thin quartz capillary housing (Diameter = 500 μm, wall thickness = 10 μm). The electrochemical performance of the cell is measured by connecting two wires, from the targeted electrode and a Li counter electrode to an external instrument. **Figure 4.1d** shows X-ray transmission rates of the cell components at varying photon energy. The X-ray transmission rate of Ge is dramatically dropped above 11.1 keV of photon energy by exceeding the K-shell absorption edge. At 11.2 keV of photon energy, μm-sized Ge particles absorbed 30% - 60% of irradiated X-ray while around 30% of the

42

X-ray is absorbed in quartz glass housing and EC/DEC electrolyte. As shown in **Figure 4.1c**, Ge particles are clearly identified as bright colors from the background because of their high attenuation.
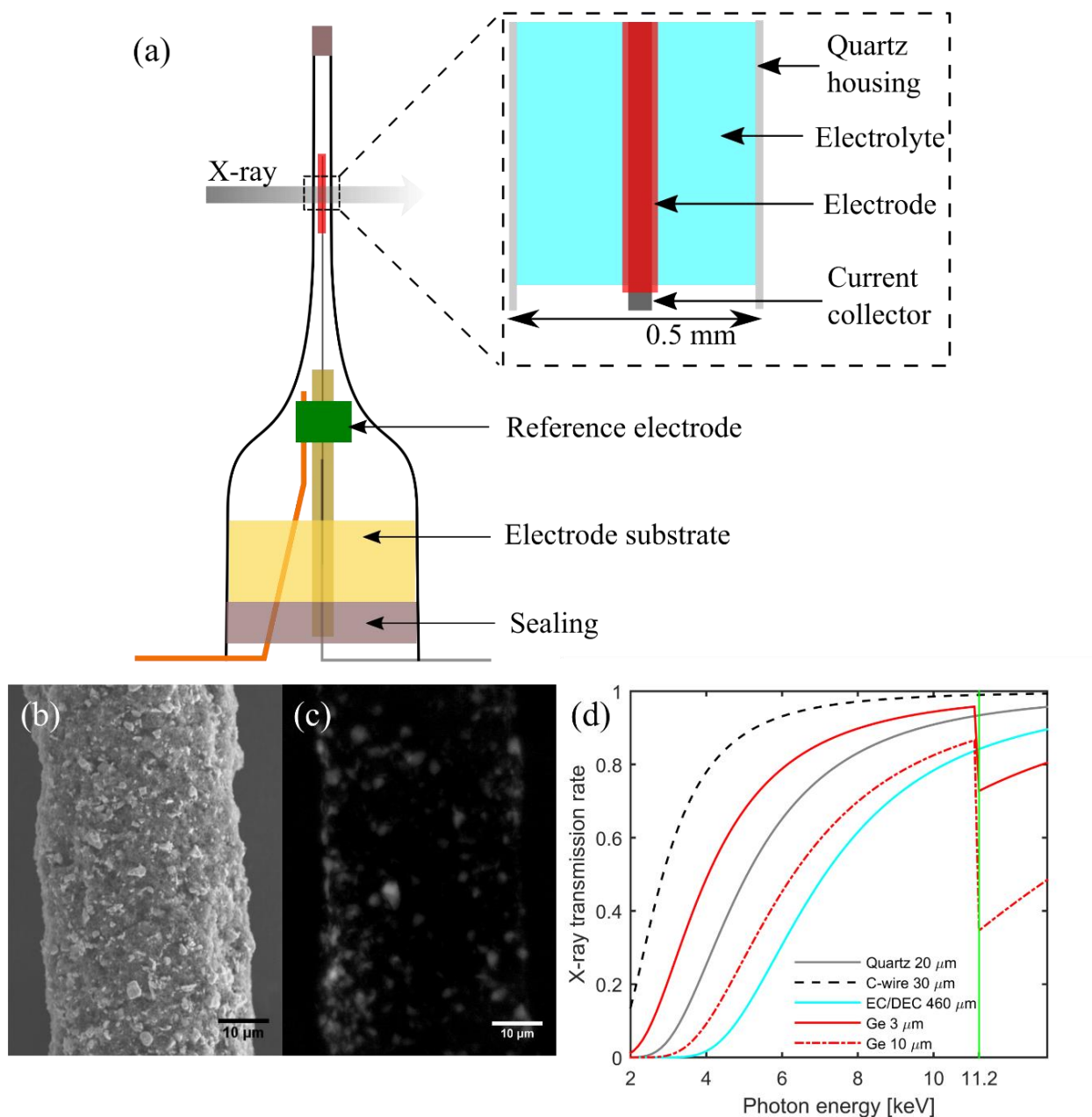
Figure 4.1 In Situ Battery Cell. (a) Schematic of the in-situ battery cell, (b) SEM image of a pristine Ge electrode on a carbon wire (30 μm) current collector, (c) A TXM image of a pristine Ge electrode in the in situ battery cell, and (d) X-ray transmission rate of the cell components. About 30% of X-ray radiation is absorbed by the quartz capillary, carbon wire, and EC/DEC electrolyte at 11.2 keV.

4.3.2 Fabrication of Ge and $Ge_{0.9}Se_{0.1}$ electrodes for in situ TXM

Electrode slurry was composed of 50 wt% active material (Ge or $Ge_{0.9}Se_{0.1}$), 30 wt% Super-P carbon black conductive additive, and 20 wt% carboxymethyl cellulose (CMC) polymer binder from 5% CMC solution. The CMC binder (90 kDa, Sigma-Aldrich, St. Louis, MO, USA) was pre-dissolved in deionized water. µm-sized Ge and $Ge_{0.9}Se_{0.1}$ powders were synthesized as described in Ref[131] and the super-P carbon black (C65) was purchased from TIMCAL. A carbon wire (Diameter = 30 µm, WPI, Sarasota, FL, USA) was selected as the current collector of the working electrode because it has a high X-ray transmission rate and is more rigid in the electrolyte-filled cell. One end of the carbon wire (bottom side) was attached to a nickel alloy wire (Diameter = 75 µm, Alfa Aesar, Reston, VA, USA) in a 1 cm length of fused silica tubing (Diameter = 250 µm, SGE, Australia). The long nickel alloy wire is going to be connected to an external circuit. The two opened ends of the silica capillary were sealed with epoxy. In an oxygen plasma chamber (PE-50, Plasma Etch, Carson City, NV, USA), the carbon wire was etched for 2 min to enhance surface adhesion with the electrode slurry. The surface-treated carbon wire set was laid on a copper sheet and uniformly coated with the electrode slurry via a film casting doctor blade. The wire electrode was separated from the copper sheet when the electrode slurry was partially dried to maintain uniform thickness through the carbon wire. Then, it was dried in a vacuum oven at 110 °C for 10 h. An SEM image of the fabricated Ge electrode is shown in **Figure 4.1b**.

4.3.3 Assembly of the in situ battery cell for TXM

The in situ battery cell was assembled in an argon-filled glovebox (under O_2 < 0.1 ppm, H_2O < 0.1 ppm; Unilab 2000, Mbraun, Stratham, NH, USA). A small piece of Li metal (thickness of 0.6 mm foil, Sigma-Aldrich, St. Louis, MO, USA) was attached to a copper wire (D=200 µm) as the counter electrode. The counter electrode was attached to the silica capillary wall by epoxy. The silica capillary prevents direct contact between the working and counter electrodes. The entire set of electrodes was carefully inserted into a funnel-shaped open-end (Dia = 3 mm) of a quartz capillary (Hampton, Aliso Viejo, CA, USA), and the working electrode was located at the thin capillary region (inner diameter = 500 µm, wall thickness = 10 µm). To mount the electrode on the cell housing, 0.02 ml of PDMS mixture (Sylgard 184, Dow Corning, Auburn, MI, USA) was injected into the funnel-shaped end and cured at 80 °C on a hotplate for 15 min (PDMS electrode

substrate in **Figure 4.1a**). The quartz housing was fully filled with 1 M LiPF$_6$ EC/DEC (1:1 v/v) electrolyte through a micro-syringe. The PDMS sealing was capable of being penetrated by the micro-syringe and preventing leaking of the electrolyte. After injecting electrolyte, the top open end of the capillary was sealed with 5-min epoxy. Both ends of the quartz capillary were sealed with torr epoxy (Torr seal vacuum epoxy, Agilent Technologies, Lexington, MA, USA) to prevent leaking of the electrolyte. The nickel alloy wire of the working electrode and the copper wire of the counter electrode were connected to a battery cycler (BT 2000, Arbin, College Station, TX, USA) during the operando TXM study.

4.3.4   Combined in situ TXM tomography and operando TXM imaging

In situ battery cells were assembled as described above to investigate morphological changes of the Ge and Ge$_{0.9}$Se$_{0.1}$ electrodes by employing in situ TXM tomography and operando TXM imaging. Here, the in situ tomography indicates a 3D scanning of a targeted electrode by capturing TXM images at 720 angles over a 180° rotation when the battery cell is not working. To avoid the hard X-ray induced damage on the carbon-binder matrix, intermittent X-ray exposure during image capturing was used, as shown in Ref [140]. The operando TXM imaging periodically records a series of TXM images for the targeted electrode during cell operation. The experimental procedure was as follows: 1) in situ tomography for a pristine electrode, 2) operando TXM imaging during the first lithiation of the pristine electrode, 3) in situ tomography for the lithiated electrode, 4) operando TXM imaging during the first delithiation of the lithiated electrode, and 5) in situ tomography for the delithiated electrode. The TXM images with 38.8 nm of pixel size were recorded with 1 s exposure time. The in situ battery cells were operated at 0.1 - 0.2 C rates under galvanostatic conditions.

4.3.5   Operando coin cell assembly

Ge and Ge$_{0.9}$Se$_{0.1}$ electrodes for XRD and XAS were fabricated from an 80:10:10 (weight%) mixture of active material, carbon black, and polyvinylidene difluoride (PVDF). The mixture was added into the NMP solution and mixed homogeneously for 20 h. The produced slurries were coated onto a thin pyrolytic graphite sheet and a copper foil for XRD and XAS, respectively. The graphite sheet was used as the current collector to avoid strong X-ray absorption during XRD

collection. The electrodes were dried at 100 °C in a vacuum oven for 12 h. Circular discs with 1.11 cm in diameter were punched out of the electrodes film and stored in an argon-filled glove box for coin cell assembly. The CR2032 coin cells were modified and used in this study. 2 mm diameter holes were punched at the center of both anode and cathode cases. 30 µm thick Kapton tape was adopted to seal the hole on both sides of the case. **Figure 4.2** displayed the order of the operando coin cell assembly. The current collector on top of the anode case with a 2 mm hole was to maximize the contact of the electrode. The electrode was placed on the collector followed by adding 20 µL $LiPF_6$ electrolyte. A Celgard 2400 separator was placed on top of the electrode with an additional 20 µL electrolyte on top of it. A piece of lithium metal with 1.27 mm in diameter was laid on the separator followed by a stainless-steel plate (with a 2 mm hole at the center) and a wave spring. The cell was crimped and taken out of the glove box for electrochemical evaluation.
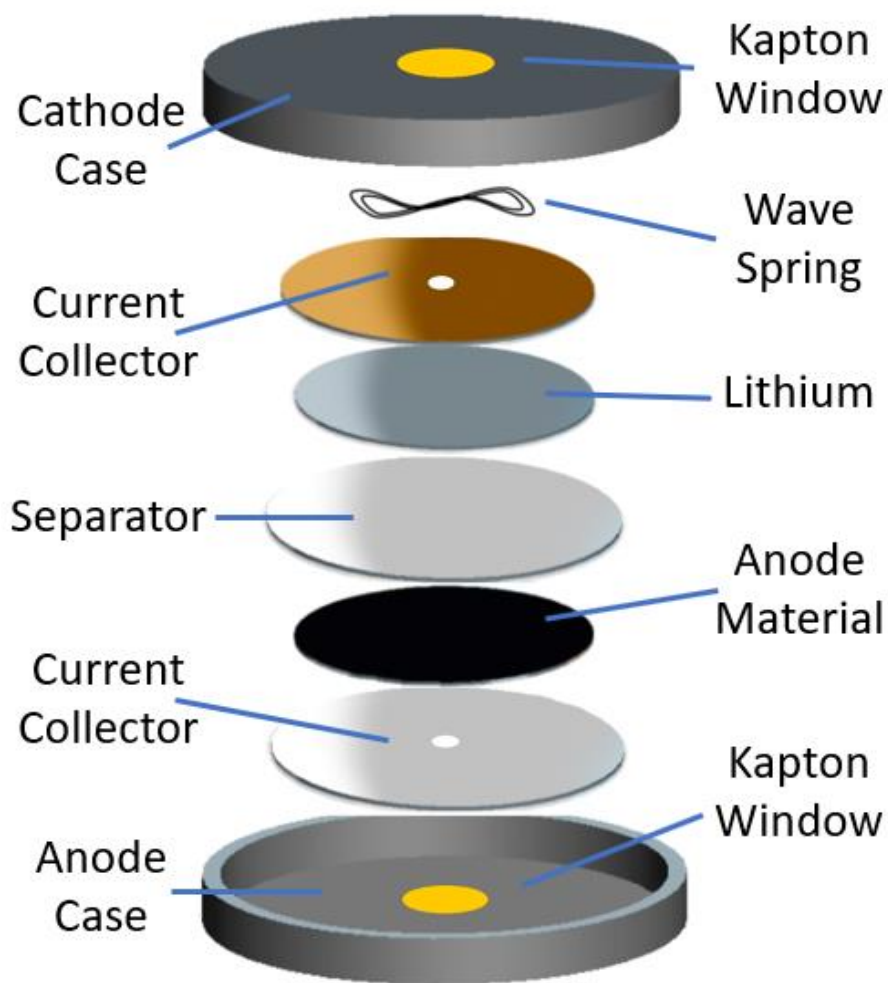
Figure 4.2 Schematic of the operando coin cell assembly for operando synchrotron XRD and XAS experiments.

4.3.6   Synchrotron X-ray diffraction

The operando XRD experiment was conducted at beamline 11-ID-C of the APS with a photon wavelength of 0.1174 Å and an energy of 105.6 keV. The incident beam size on the sample was 50 µm * 50 µm. Measurements were carried out in transmission mode. The detector was located 1800 mm from the sample. The scattering intensity was detected on a 2D Perkin-Elmer detector with a pixel size of 200 µm (2048 * 2048 pixels). The schematic for the synchrotron XRD setup is shown in **Figure 4.3**. Both of Ge and $Ge_{0.9}Se_{0.1}$ coin cells were cycled at a constant current rate of 0.1 C. The diffraction data for each sample were collected each ten minutes interval. The exposure time was 0.5 s and 40 captures were averaged for each data collection. The 2D diffraction patterns generated via operando XRD were calibrated using a standard CeO_2 sample and converted to 1D patterns via Fit2D software. Data were analyzed via Match! software.
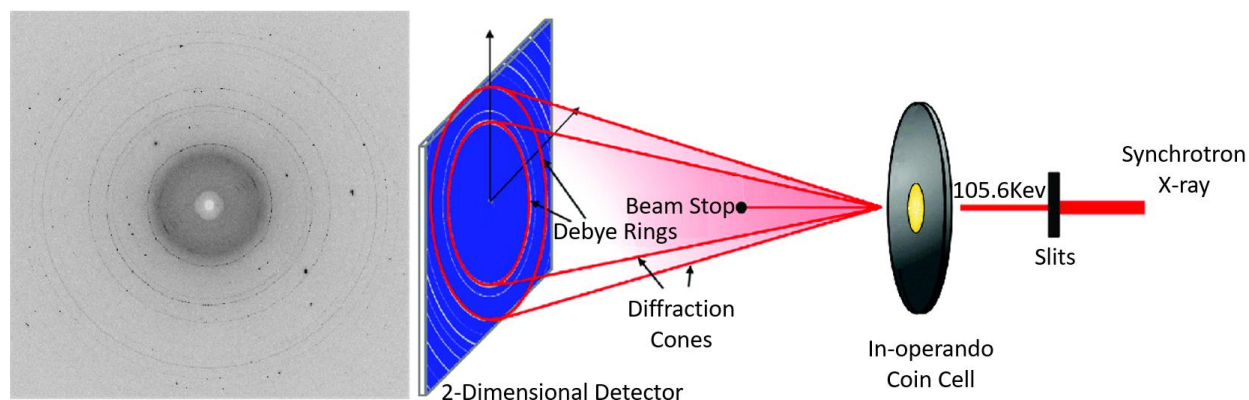
Figure 4.3 The synchrotron X-ray diffraction setup and its resulting diffraction pattern.

4.3.7   Synchrotron X-ray absorption spectroscopy

Germanium and selenium K-edge XAS measurements were performed at beamline 20-BM of the APS. Energy calibration was monitored by the use of Ge standard (11103.0 eV). The beam size employed in this study was 500 µm * 500 µm and the incident beam was monochromatized by using a Si (111) fixed-exit, double-crystal monochromator. The XAS spectra were recorded in transmission for the in situ coin cell with a 34 min interval using the same coin cell setup as in XRD (**Figure 4.2**). The spectra were normalized via ATHENA software to obtain the X-ray absorption near edge structures (XANES) and extended X-ray absorption fine structure (EXAFS).

4.4　Results and discussion

In this study, operando 2D TXM image acquisition was implemented to monitor the dynamic morphological change of Ge and $Ge_{0.9}Se_{0.1}$ electrodes under galvanostatic operation. Ge and $Ge_{0.9}Se_{0.1}$ electrodes were (de)lithiated at approximately 0.2 C (1 μA for Ge and 0.6 μA for $Ge_{0.9}Se_{0.1}$). TXM images were recorded every 10 min during the first cycle. **Figures 4.4a - b** show the dynamic change of one Ge particle and one $Ge_{0.9}Se_{0.1}$ particle (around 3.5 μm in volume equivalent shape diameter (VESD) for both) during the first lithiation. **Figures 4.4c - d** show the voltage profiles of the cycling process of the Ge and $Ge_{0.9}Se_{0.1}$ electrodes, the dynamic optical density (OD) changes of the two active particles shown in **Figures 4.4a – b**, as well as another Ge (5.3 μm in VESD in its pristine condition) and $Ge_{0.9}Se_{0.1}$ particles (3.2 μm in VESD in its pristine condition). **Figure 4.5a** represents the Ge electrode microstructure in the pristine status. The dynamic change includes volume and optical density (OD) changes of the active particles, and electrode cluster changes during the cell operation. **Figure 4.5b** shows the operando dynamic changes of the 5.3 μm Ge particle during the first lithiation (2.62 V ~ 0.01 V) and delithiation (0.13 V ~ 1.5 V) processes. The green outline around the particle at 2.62 V (pristine status) is replicated in the TXM images that were obtained during the lithiation process. The red outlines indicate the boundary of the particle at 0.01 V (lithiated condition). In the TXM images, OD (or pixel intensity) is directly related to the change of particle electron density[137], which can be used to detect the chemical phase changes (α-Li_xGe) of the particle. As shown in **Figure 4.4c**, there are negligible OD changes for the Ge particle for 100 min of the first lithiation until the operating voltage reached 0.31 V, which is in accordance with the results shown in Ref[137]. The capacity result in Ref[137] indicates that approximately one Li-ion has been inserted per Ge atom at this potential. It is possible that the OD changes are below the detection limit of the TXM[137]. It is also possible that Li-Ge alloy has a similar absorbance as pristine Ge. In addition, some of the Li ions could be consumed to form the SEI layer or lithiated into the carbon additive. At 0.28 V, the particle clearly shows an OD drop and volume expansion by Li-ion incorporation and the phase change. **Figure4. 4c** and **Figure 4.5b** also demonstrate the shrinking of the particle and increase of the OD during the first delithiation. At the end of the delithiation (1.5 V), the OD and the overall size of the Ge particle did not return to the pristine condition. As shown in **Figure 4.4c**, the delithiation capacity of the cell is approximately 50% of the lithiation capacity. Thus, the particle might lose the electrical connection from the electrode mentioned in Ref[137]. Another reason is nanopore

formation in the Ge particle during the first delithiation[127, 141]. **Figure 4.5c** shows an aggregated Ge particle cluster in the pristine (2.62 V), lithiated (0.01V), and delithiated (1.5 V) status. It clearly shows that the cluster expanded during lithiation and shrunk during delithiation. The change of the cluster indicates the carbon-binder matrix changes caused by the large volume change of the active particles. The morphological changes of the carbon-binder matrix can lead to the loss of the electrical connection of the active materials.
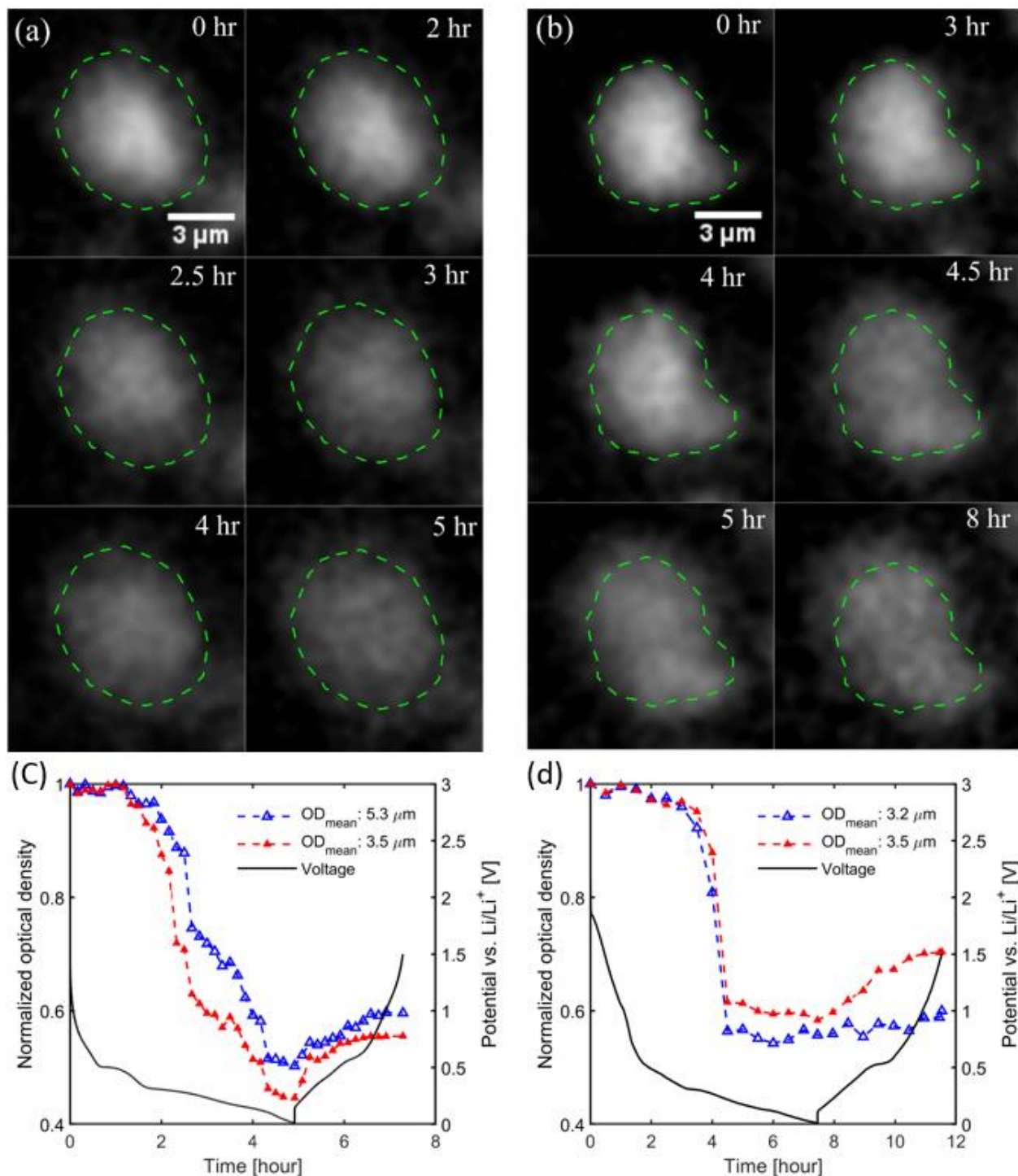
Figure 4.4 Operando TXM. TXM dynamic images of (a) Ge and (b) Ge0.9Se0.1 particles during the first lithiation. Normalized optical density (OD) dynamics of (c) Ge (5.3 μm and 3.5 μm VESD) and (d) Ge0.9Se0.1 (both around 3.5 μm VESD) particles during the first (de)lithiation. The normalized OD data points represent the average OD of the particles by their pristine states. The $Ge_{0.9}Se_{0.1}$ TXM images were captured every 30 mins under 0.6 μA of the constant current condition.
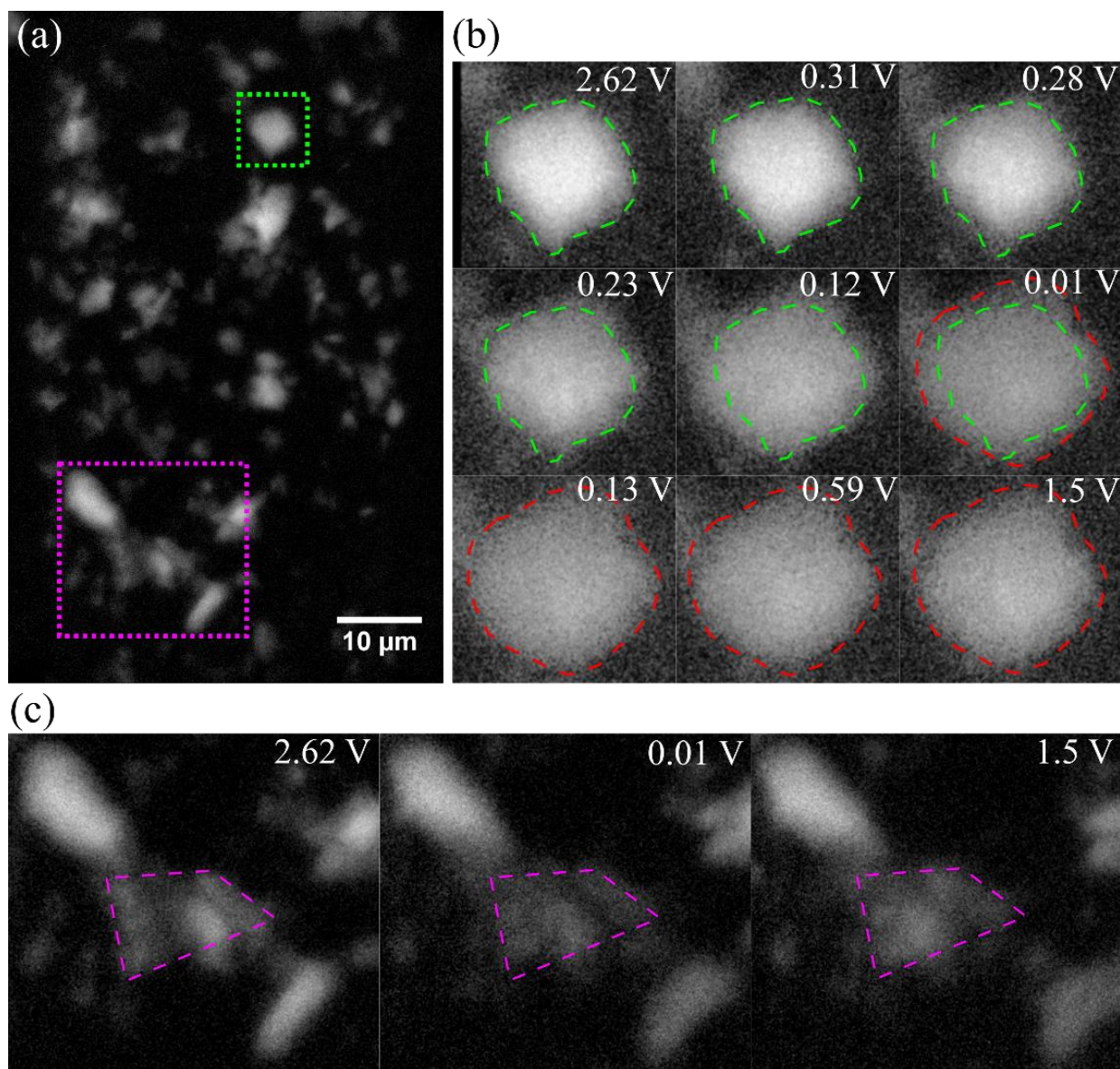
Figure 4.5 Operando TXM of Ge electrode. (a) TXM image with 38.8 nm pixel resolution of the pristine Ge electrode for 1 second irradiation at 11.2 keV, (b) TXM dynamic images of a Ge particle (5.3 μm VESD) during the first (de)lithiation under 1 μA, (c) Ge particle cluster changes at pristine (2.62 V), lithiated (0.01 V), and delithiated (1.5 V) status.

As compared with the dynamic change of the larger Ge particle (5.3 µm VESD) shown in **Figure 4.5b**, the smaller Ge particle exhibits a very similar dynamic change as shown in **Figure 4.4a** and **c**. However, if we compare the Ge and $Ge_{0.9}Se_{0.1}$ particles, they behave different dynamic changes. **Figure 4.4b** and **d** demonstrate the $Ge_{0.9}Se_{0.1}$ particle experienced a sudden expansion and OD decrease between 4 h and 4.5 h. The Ge particle displays a relative smooth expansion and slow OD decrease through the whole lithiation process, though there is still a larger change between 2 and 2.5 h. This phenomenon can be explained by the formation of a heterogeneous network of nm-sized crystalline Ge clusters, surrounded by the network of an amorphous super-ionically conductive inactive phase (Li-Se-Ge) as proposed by Klavetter et al.[131]. They have demonstrated an amorphous phase in a $Ge_{0.9}Se_{0.1}$ particle by employing high-resolution transmission electron microscopy (HRTEM)[131]. In addition, **Figure 4.4d** shows a small decrease in the OD for both of the two $Ge_{0.9}Se_{0.1}$ particles at the very beginning around 1 h that corresponds with a small voltage plateau near 1 V. This plateau has been attributed to the formation of Li-Se-Ge[131] and the slight OD decrease is due to the slight volume increase from this reaction as well as the impact on the absorbance caused by the Li-Se-Ge phase. The superconductive Li-Se-Ge network provides fast Li-ion pathways into the core of the $Ge_{0.9}Se_{0.1}$ particle because of the high ionic conductivity, and the $Ge_{0.9}Se_{0.1}$ particle could have more uniform Li-ion incorporation than the Ge particle. The operando 2D TXM imaging results support the hypothesis of a super-ionically conductive Li-Se-Ge network formed in the $Ge_{0.9}Se_{0.1}$ particle during the first lithiation process. The more sudden dynamic change of the $Ge_{0.9}Se_{0.1}$ particle is attributed to the effect of the Li-Se-Ge network. The encapsulating Li-Se-Ge layer around the nm-sized Ge particles can help them hold the original shape until the balance is broken, therefore, a more sudden change happens in $Ge_{0.9}Se_{0.1}$ particles.
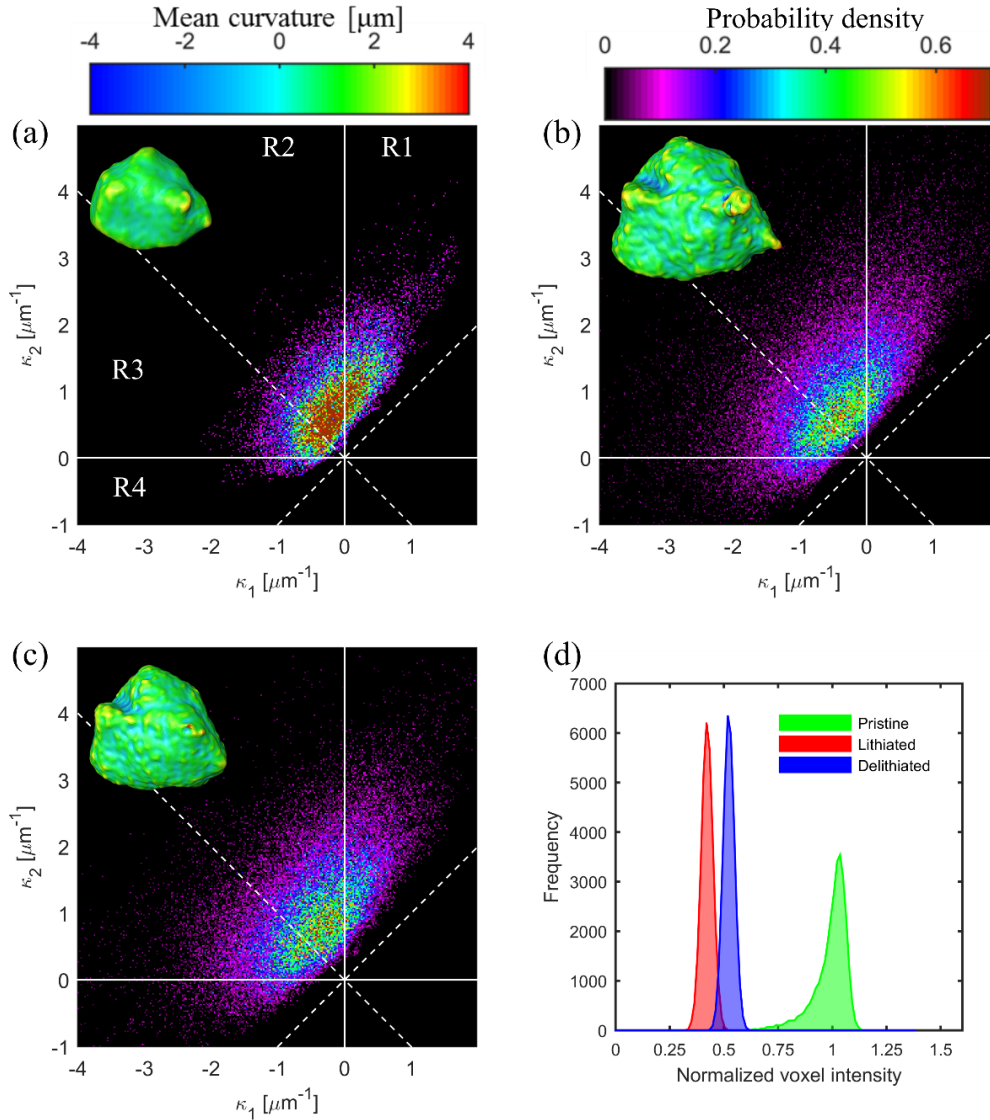
Figure 4.6 In situ TXM tomography. Three-dimensional morphologies of the Ge particle shown in Fig. S1b are color mapped with mean curvature on the surfaces of (a) pristine, (b) lithiated, and (c) delithiated conditions. Principal curvatures on the particle surface at different lithiated status are distributed known as Interfacial Shape Distribution (ISD, κ_1: minimum and κ_1: maximum principal stresses). (d) histograms of X-ray attenuation coefficients in the Ge particle. In (a), R1 region indicates convex surface ($\kappa_2 > \kappa_1 > 0$), R2 region is concave surface ($\kappa_2 < \kappa_1 < 0$). Mean curvature is positive in the R1 and R2 regions.

The in situ tomography measurement was implemented to obtain the 3D morphology of Ge and $Ge_{0.9}Se_{0.1}$ electrode structures of the in situ battery cells in their pristine, lithiated, and delithiated status. The tomographic images of the Ge or $Ge_{0.9}Se_{0.1}$ electrodes contained approximately 50 active particles. **Figure 4.6a - c** display the 3D morphological information of

the 5.3 μm Ge particle displayed in **Figure 4.5b**. The 3D morphologies of pristine, lithiated, and delithiated status are color mapped with mean curvature in the left top corners of the figures. The size of the particle in the pristine state is 5.3 μm in VESD and the surface area is 97.7 $μm^2$. The VESD is increased to 7.5 μm which means a 278% volume expansion achieved and the surface area increased to 212 $μm^2$ via Li-ion incorporation. During the first delithiation, the particle shrinks to 208% in volume and 168% in the surface area under the pristine condition.

Figure 4.6d shows histograms of normalized X-ray attenuation coefficients in the pristine, lithiated, and delithiated states. The low intensity of the delithiated particle could be due to the incomplete delithiation and/or the formation of nanopores. To investigate the surface properties, the probability density of the minimum ($κ_1$) and maximum ($κ_2$) principal curvatures are demonstrated as interfacial shape distributions (ISD)[136, 142] in **Figure 4.6a - c**. Compared with the pristine state, the lithiated particle shows a significant increase of the large curvatures and concave regions (R4, both $κ_1$ and $κ_2$ are negative). Region 4 in **Figure 4.6a** indicates the portion (2.3%) of the concave area of the pristine particle. The concave area increased to 6.8% after the lithiation process and decreased to 5.1% after delithiation. The rougher surface and increased concave area are caused by the inhomogeneous volume expansion of the pristine Ge particle.

The reconstrauted images displayed in **Figure 4.7** demonstrates the three-dimensional morphological changes and curvature information of a Ge particle and a $Ge_{0.9}Se_{0.1}$ particle with similar size in their pristine, lithiated, and delithiated states. The pristine Ge particle is 2.7 μm and the pristine $Ge_{0.9}Se_{0.1}$ particle is 2.6 μm in VESD. For the Ge particle, the volume change is 223% after lithiation and 159% after delithiation. Similarly, the volume change is 251% after lithiation and 141% after delithiation for the $Ge_{0.9}Se_{0.1}$ particle. However, the curvature distribution shows very different surface properties. The $Ge_{0.9}Se_{0.1}$ particle shows a smoother surface and more homogeneous morphological change during the lithiation and delithiation processes than the pure Ge particle, and especially after delithiation (**Figure 4.7f**). Klavetter et al. have demonstrated this phenomenon previously by employing HR-TEM that $Ge_{0.9}Se_{0.1}$ particles do not experience nanopore formation and have smoother surfaces during cycling[131]. This major difference is attributed to the more homogeneous Li-ion transport in the $Ge_{0.9}Se_{0.1}$ particle due to the super-ionically conductive Li-Se-Ge network.
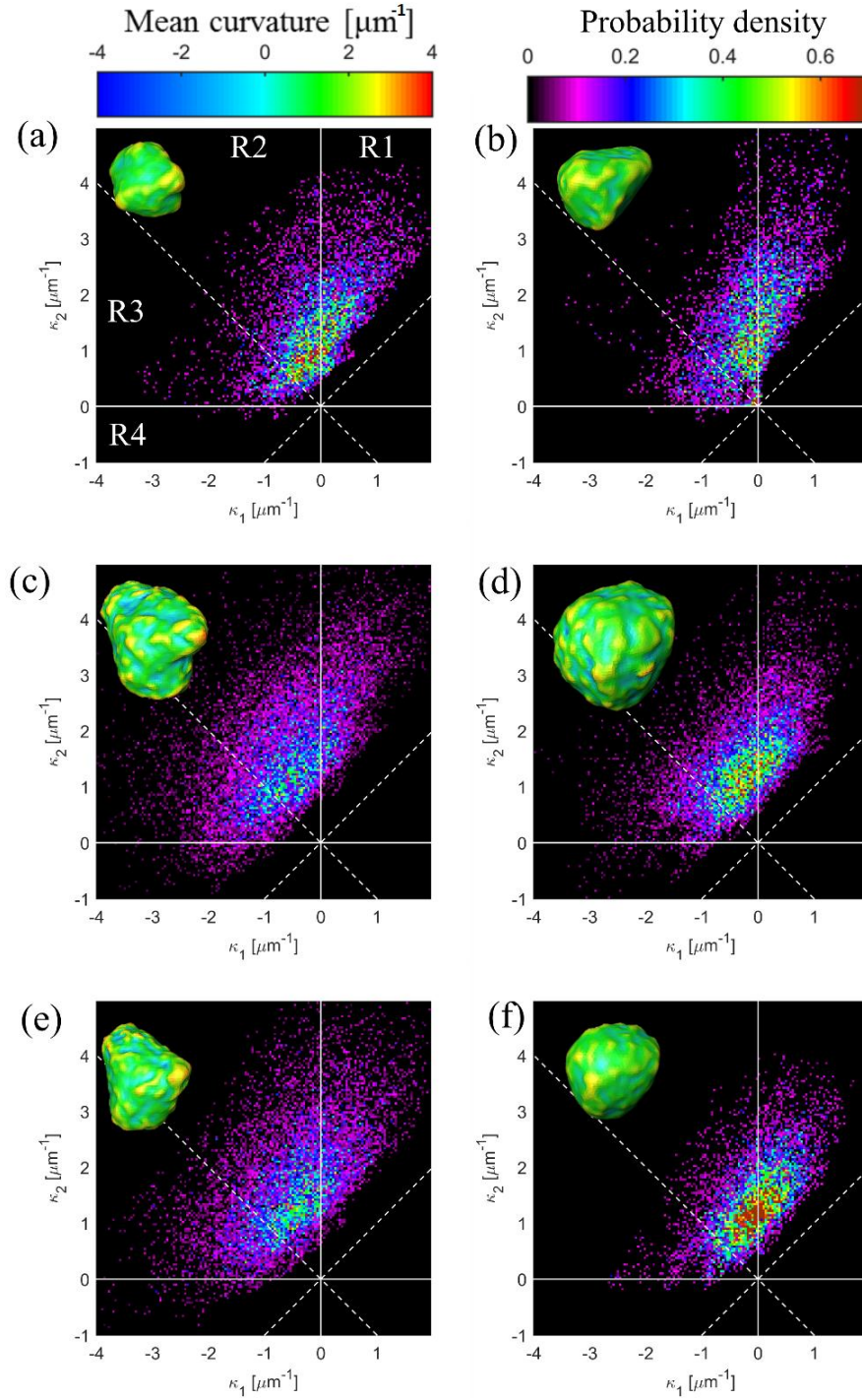
Figure 4.7 In situ TXM tomography. Mean and principal curvature distributions of (a) pristine Ge particle (2.7 μm VESD), (b) pristine $Ge_{0.9}Se_{0.1}$ particle (2.6 μm VESD), (c) lithiated Ge particle, (d) lithiated $Ge_{0.9}Se_{0.1}$ particle, (e) delithiated Ge particle, (f) delithiated $Ge_{0.9}Se_{0.1}$ particle.

To further explain the formation of the super-ionically conductive Li-Se-Ge network and its effect on the electrochemical performance, operando XRD measurements for Ge and $Ge_{0.9}Se_{0.1}$ cells during 0.1 C cycling was conducted at beamline 11-ID-C of the APS to investigate the dynamic phase changes. As shown in **Figure 4.8a - c**, the XRD result for pure Ge electrode has a similar behavior as reported by Ref[92]. We observed the disappearance of Ge peaks after 7 h and the formation of $Li_{15}Ge_4$ as the only crystalline product at the end of the first lithiation process. The crystalline $Li_{15}Ge_4$ phase disappeared during the process of delithiation and no crystalline Ge was observed at the end of delithiation. As shown in **Figure 4.8d - f**, the $Ge_{0.9}Se_{0.1}$ electrode exhibits the peaks of crystalline GeSe alloy and crystalline Ge at the pristine state. During the process of lithiation, we observed the disappearance of the GeSe peak at the very beginning when the voltage reached its first plateau around 1 V. After that, the $Ge_{0.9}Se_{0.1}$ electrode did not regain the GeSe peak during the first cycle. The disappearance of GeSe crystal has been proposed to be the formation of the Li-Se-Ge inactive phase which corresponds to the observation of OD decrease at about 1 V shown in **Figure 4.4d**. The crystalline Ge peaks started to disappear at about 10 h and no $Li_{15}Ge_4$ or other crystalline Li_xGe alloys were observed at the end of lithiation. It is a significant difference between pure Ge and $Ge_{0.9}Se_{0.1}$. As proposed by Ref [143], the formation of the crystalline $Li_{15}Ge_4$ phase from amorphous Li_xGe phases would require not only Ge−Ge bond breakage but also the rearrangement of Ge (Ge migration), which involves a large active barrier. We believe that the Li-Se-Ge network could add a large barrier to the rearrangement of Ge and suppress the formation of crystalline $Li_{15}Ge_4$. At the end of the first delithiation, no crystalline Ge was observed. After the first cycle, the phase change of the $Ge_{0.9}Se_{0.1}$ electrode in the cycling process is between amorphous Ge and amorphous Li_xGe, and no crystalline phases are involved, which could be one of the mechanisms leading to the better mechanical stability of the $Ge_{0.9}Se_{0.1}$ electrode.
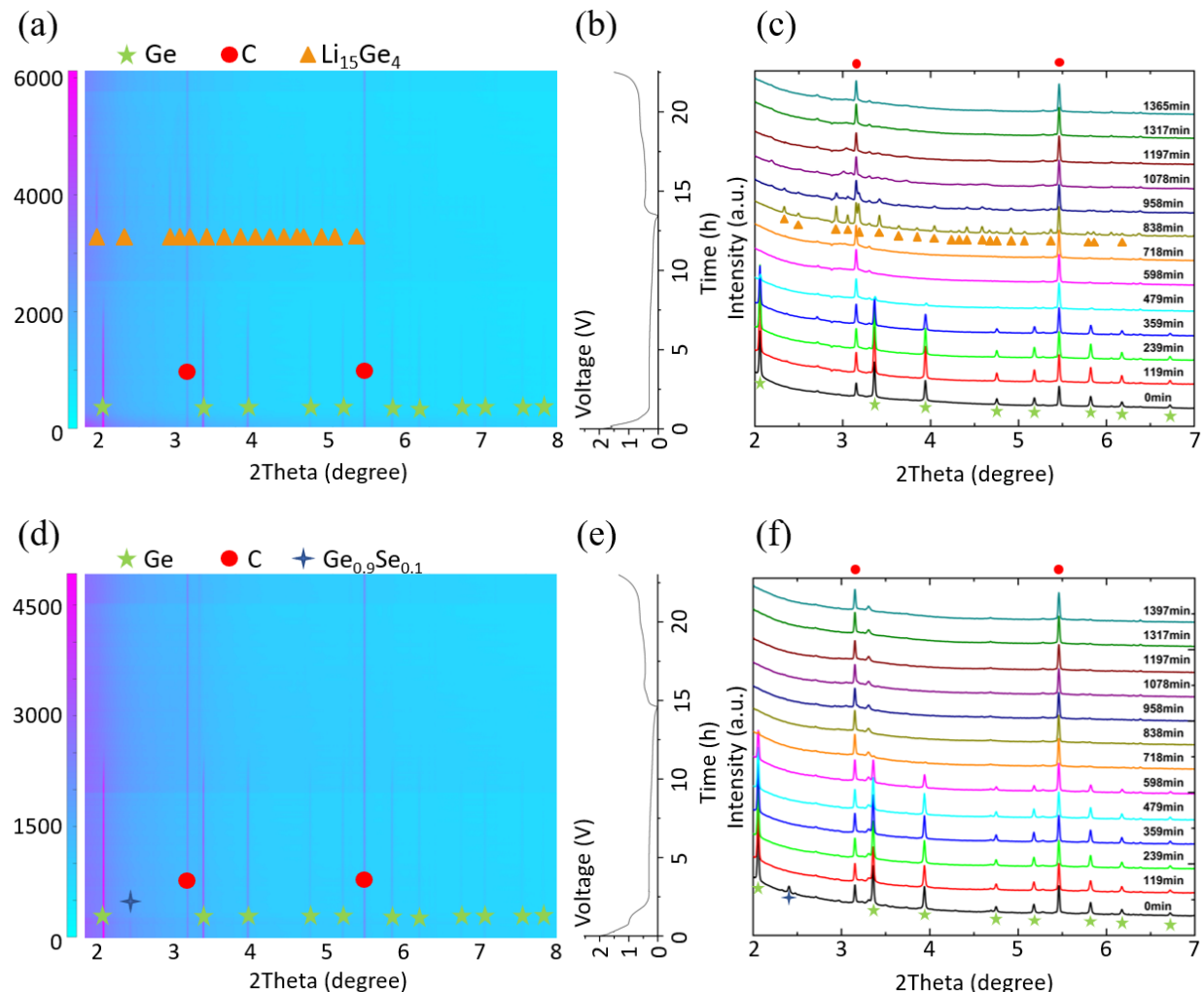
Figure 4.8 Operando XRD results. (a) XRD patterns of a Ge cell during the first cycle at 0.1 C. (b) Voltage profile of the Ge cell. (c) Selected XRD patterns of the Ge cell. (d) XRD patterns of a $Ge_{0.9}Se_{0.1}$ cell during the first cycle at 0.1 C. (e) Voltage profile of the $Ge_{0.9}Se_{0.1}$ cell. (f) Selected XRD patterns of the $Ge_{0.9}Se_{0.1}$ cell. Lithium diffraction patterns have been marked off via Fit2D.

In order to obtain further insights into the amorphous Li-Se-Ge network in the $Ge_{0.9}Se_{0.1}$ electrode, operando X-ray absorption spectroscopy (XAS) of Ge K-edge and Se K-edge measurements during 0.1 C cycling was conducted at beamline 20-BM of the APS. The voltage profile of the operando coin cell is shown in **Figure 4.9a**. The Se K-edge absorption energy for pristine $Ge_{0.9}Se_{0.1}$ matched well with selenium standard (12658 eV) which is assigned to the transition of Se 1s core electrons to the unoccupied 4p state as displayed in **Figure 4.9b**. The lack of data between 10 min and 178 min was due to the unexpected beamline outage at the APS. The

X-ray absorption near edge spectroscopy (XANES) of Se clearly shows the energy shift to higher energy due to the increased oxidation state[144]. The standard K-edge shift for Li_2Se is 12660 eV as reported in Ref[145], which demonstrates a ratio of two Li ions per Se atom. The smaller energy shift of Se K-edge (12659 eV) in this experiment indicates that the oxidation state of Se is not Li_2Se. It accords with the operando XRD result shown in **Figure 4.8b**, which did not show the crystalline Li_2Se phase during the lithiation process. The combination of XAS and XRD results demonstrate the formation of the Li-Se-Ge phase at the very beginning of the lithiation process. The Li-Se-Ge phase has been further proven to be inactive via the operando XAS results. As shown in **Figure 4.9b**, once the Li-Se-Ge phase is formed, its X-ray absorption remains the same during the entire cycling process as its white line is not shifting anymore at 12663 eV while the standard white line positions of Se and Li_2Se are 12660 eV and 12665 eV, respectively. **Figure 4.9c** shows the comparison of the XANES spectra at Ge K-edge between ex-situ pure Ge and operando $Ge_{0.9}Se_{0.1}$ electrodes at the fully lithiated state. Both of their pristine statuses have similar spectra but their spectra after lithiation are different. The spectrum for Ge after lithiation represents the formation of $Li_{15}Ge_4$ while the spectrum for $Ge_{0.9}Se_{0.1}$ indicates it was an amorphous Li_xGe phase. The corresponding normalized first derivatives of XANES (**Figure 4.9c**) spectra are shown in **Figure 4.10**, which clearly demonstrates the difference.
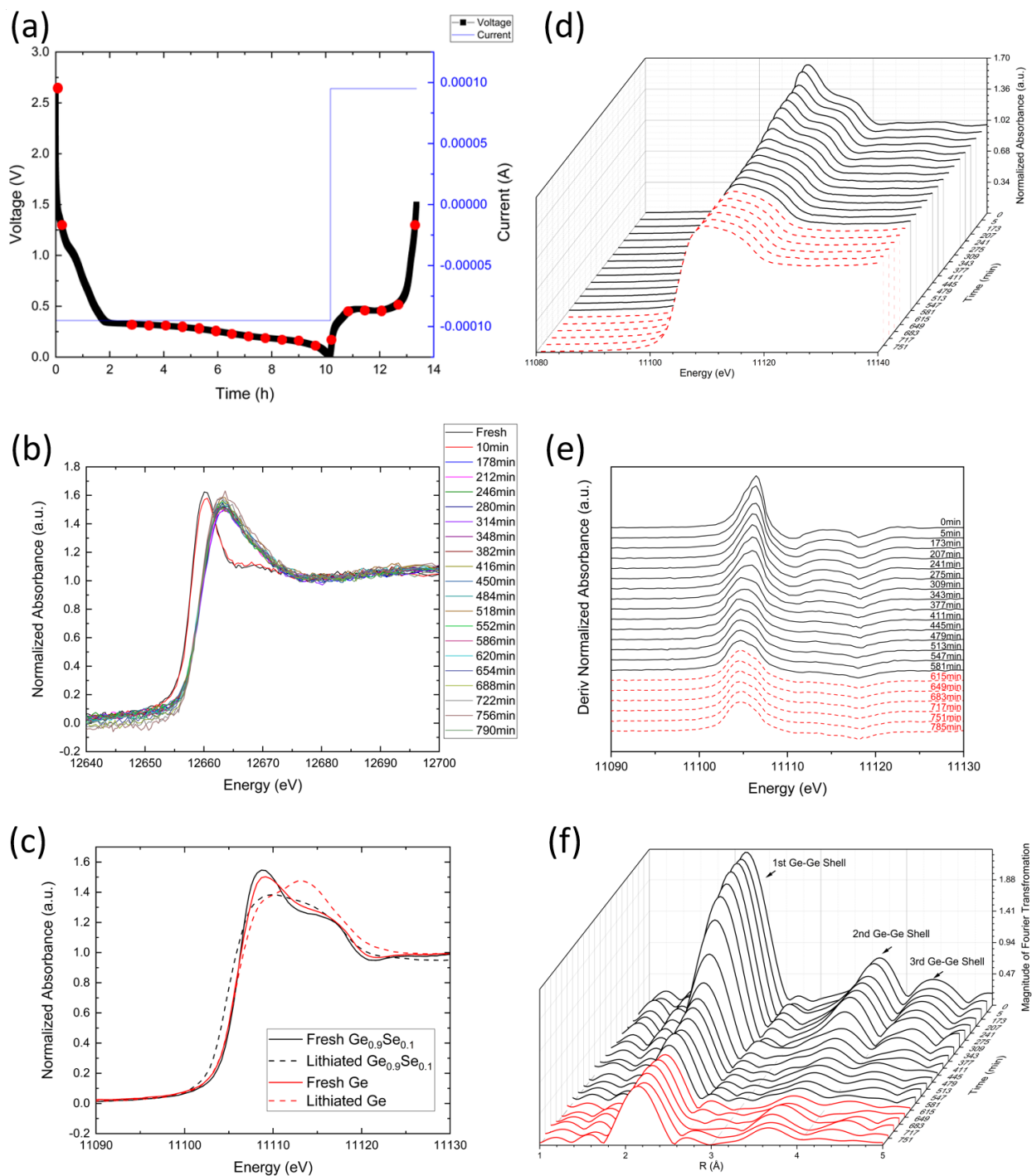
Figure 4.9 Operando XAS results for $Ge_{0.9}Se_{0.1}$. (a) current potential plot with highlighted data collecting points, (b) selected selenium XANES results. (c) comparison of ex-situ Ge (red) and operando $Ge_{0.9}Se_{0.1}$ (black) electrode at pristine (solid) and lithiated status (dash). (d) selected germanium XANES results during lithiation (black solid) and delithiation (red dash). (e) the corresponding normalized first derivative of XANES spectra in (d). (f) Fourier Transforms of EXAFS spectra in (d) during lithiation (black) and delithiation (red).

59
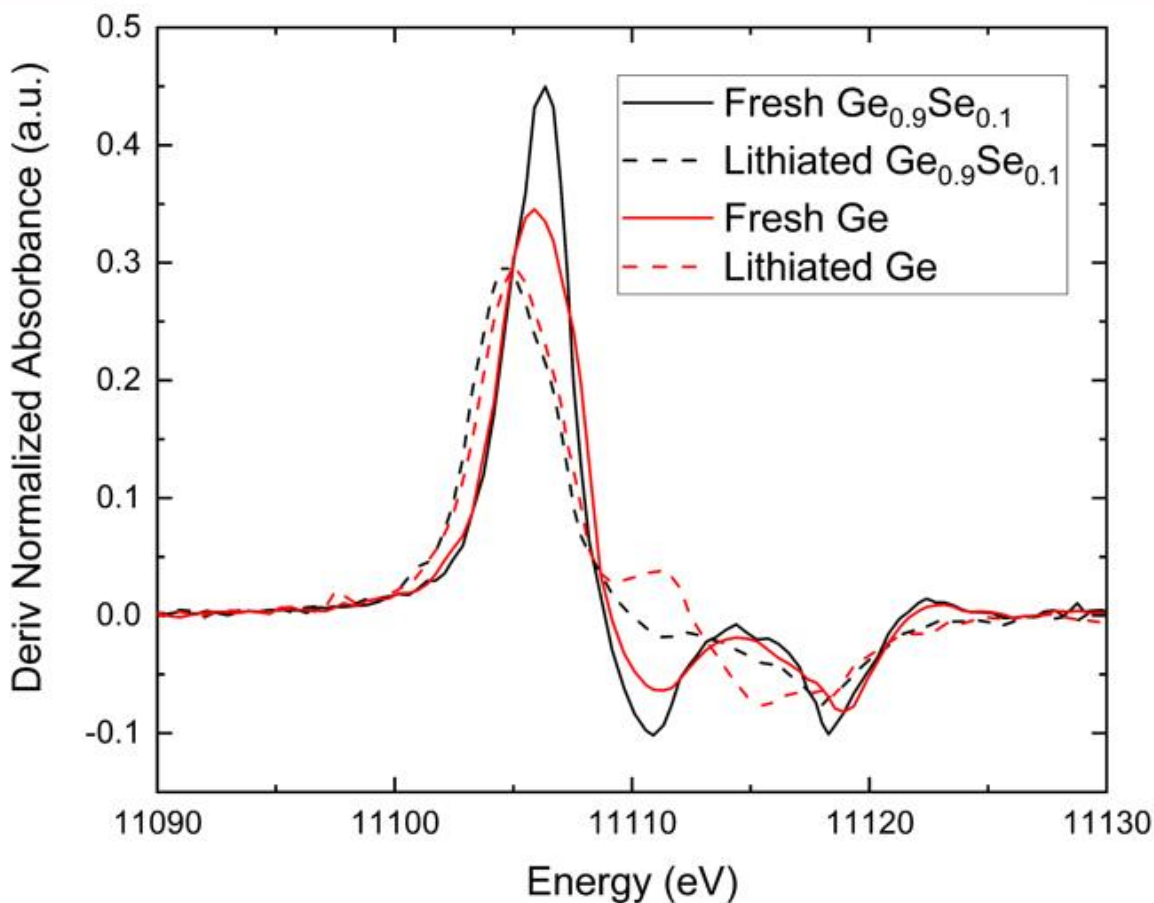
Figure 4.10 Normalized first derivatives of XANES spectra in Figure 4.6c.

The operando X-ray absorption near edge spectroscopy (XANES) of $Ge_{0.9}Se_{0.1}$ electrode and its first-derivative are shown in **Figure 4.9d** and **e**. The Fourier Transforms (FT) of Ge extended X-ray absorption fine structure (EXAFS) spectra of the $Ge_{0.9}Se_{0.1}$ electrode during lithiation and delithiation processes are shown in **Figure 4.9f**. Compared with the previous operando XAS data of pure Ge electrode shown in Ref [92-94], **Figure 4.9b - f** exhibit several different characteristics, which can be attributed to the Li-Se-Ge network. First, there is a clear Ge oxidation state change from 5 min to 173 min as shown in **Figure 4.9d** with a decrease in X-ray absorption at the beginning. **Figure 4.9e** also shows the first-derivative peak shifts to the lower energy during this period. Both characteristics indicate the change of oxidation status. Interestingly, there is no clear change between 173 min and 275 min after the initial change in both XANES spectra and its first derivative which is similar to the pure Ge XANES result at the beginning of

the first lithiation process [92]. This phenomenon indicates that Ge is involved in the reaction between Se and Li at the beginning of the lithiation process and an amorphous Li-Se-Ge network is formed. After the formation of the Li-Se-Ge network, the XANES spectra of the $Ge_{0.9}Se_{0.1}$ electrode behave almost the same as the pure Ge electrode [92-94]. The spectra remain unchanged for some time. Then it starts to change to broader XANES spectra and the first derivative peak starts to shift to lower energy at 309 min. These changes indicate the amorphization of Ge and the formation of amorphous Li_xGe phases. Second, the XANES spectra do not show the formation of crystalline $Li_{15}Ge_4$. As shown in **Figure 4.9c**, at the end of lithiation, the XANES spectrum of Ge is in the transition between Ge and $Li_{15}Ge_4$ with no peak at 11113 eV indicates only amorphous Li_xGe phases present at the end of lithiation. In addition, the first derivative spectra do not show a dramatic line shape change at the end of lithiation and the beginning of delithiation in **Figure 4.9e**, which also indicates that there is no phase transformation from amorphous Li_xGe to crystalline $Li_{15}Ge_4$. The Fourier Transforms of the EXAFS spectra are investigated to better understand the reaction mechanism that occurs during the electrochemical cycling. It can be observed in **Figure 4.9f** that the magnitude of the first, second, and third shell decreased as lithiation proceeded. However, the first and second Ge-Ge shells are preserved and only the third Ge-Ge shell disappeared at the end of lithiation, which is different from the pure Ge data (The intensity of all three shells disappears at the end of lithiation reported by Lim et al. [92]). This result indicates insufficient Ge migration for the formation of crystalline $Li_{15}Ge_4$. Upon delithiation, the third shell did not recover and the intensity of the other two shells almost did not change, which represents the phase transformation during delithiation is between amorphous Li_xGe and amorphous Ge.

4.5   Conclusion

In summary, the morphological evolution of Ge and $Ge_{0.9}Se_{0.1}$ electrodes has been investigated by using high resolution synchrotron TXM. An in situ battery cell was developed for the combined 2D operando TXM imaging and 3D in situ tomography. Unlike pure Ge, the observed 2D dynamic change of $Ge_{0.9}Se_{0.1}$ particles show sudden morphological and OD changes during the first lithiation. Moreover, compared to the Ge particle, the $Ge_{0.9}Se_{0.1}$ particle has a more homogeneous volume change and smoother surface, which results in better mechanical stability for the $Ge_{0.9}Se_{0.1}$ electrode during cycling. The more sudden and homogeneous volume changes in the $Ge_{0.9}Se_{0.1}$ particles are attributed to the super-ionically conductive Li-Se-Ge network, which

contributes to the fast ion transport into the particle as well as buffering the volume change. To verify the formation of the Li-Se-Ge network, operando XRD and XAS experiments were conducted. The results prove several hypotheses regarding the good cycling performance and rate capability of the $Ge_{0.9}Se_{0.1}$ electrode. A super-ionically conductive Li-Se-Ge network was formed at the beginning of the lithiation process and it is inactive during the following cycling processes. The formation of the crystalline $Li_{15}Ge_4$ phase was suppressed due to the encapsulation of the Li-Se-Ge network on nm-sized Ge particles. This fundamental study brings some insights into the design of high capacity LIB electrode materials. An in situ formed, super-ionically conductive, and inactive network in µm-sized active material particles could improve the mechanical stability of the electrode and leads to good cycling performance and rate capability.

Acknowledgment

5. A SELF-HEALING LIQUID METAL ANODE WITH PEO-BASED POLYMER ELECTROLYTES FOR RECHARGEABLE LITHIUM BATTERIES

5.1 Abstract

Ga-Sn liquid metal material is demonstrated as a self-healing anode system due to its fluidity via operando synchrotron-based transmission X-ray microscopy and X-ray diffraction experiments. Cracks formed due to volume expansions can be recovered by the fluidity of the liquid metals. By incorporating with a poly(ethylene oxide) (PEO)-based electrolyte at 60 °C, the Ga-Sn anode shows a reversible lithium insertion and extraction process with a high initial discharge specific capacity of 682 mAh g^{-1}, followed by delivering a capacity of 462 mAh g^{-1} in the second cycle at C/20 rate. Compared with its solid counterparts, the Ga-Sn liquid metal anode demonstrates a better capability to maintain its mechanical integrity and better contact with PEO solid electrolytes due to its advantageous features of the liquid. This study suggests a potential strategy to use liquid metal alloys with polymer solid electrolyte to solve the anode challenges in rechargeable lithium batteries.

5.2 Introduction

Energy storage has become one of the most important research areas in the 21st century owing to fast and significant development in technology. In the past two decades, lithium-ion batteries (LIBs) have been extensively applied in portable electronic devices, electric vehicles (EVs) as well as large-scale energy storage systems favored for their high energy density. However, the graphite used as the anode in current commercial LIBs has limited specific capacity and volumetric capacity (372 mAh g^{-1} and 837 mAh cm^{-3}) [26]. Recently, Li-alloy materials (*e.g.* Si, Ge, and Sn) have attracted much attention as anode materials due to their higher theoretical specific capacity. However, Li-alloy materials have not yet been widely applied in commercial batteries because of some unresolved technical challenges [56, 90, 92, 93, 138, 141, 146, 147]. The primary challenge is their unsatisfied cycling performance resulted from the large volume expansion/contraction during lithiation and delithiation reactions [56, 105, 148, 149]. Such a huge volume change causes mechanical cracks of the anode particles, detachments of the active

63

materials from the current collector, and poor contacts with the electronically conductive networks, which lead to the deactivation of active materials. Besides, the Li-alloy materials usually have insufficient Coulombic efficiency (CE) and dysphoric solid electrolyte interphase (SEI) layer during cycling.

To overcome these challenges, many ongoing efforts have been devoted to developing Li-alloy anode materials with promising cycling performance, such as intermetallic electrode [150-152], doped alloys [56, 138, 153], and nano-structuring active materials [47, 59, 154-160]. Among recent approaches, liquid metals (LM) with low melting points have been proposed as anode candidates due to their self-healing behavior and high theoretical capacity [68, 161, 162]. Gallium (Ga) is a unique metal with a low melting point (29.8 ℃) which can deliver a theoretical capacity of 769 mAh g^{-1} by taking up to two lithium atoms for full lithiation, therefore reported as a promising LM anode material by Deshpande et al. and a few other studies [163-165]. Furthermore, Guo et al. applied Ga-In alloy with a melting point as low as 15 ℃ in both Li-ion and Na-ion batteries showing promising cyclic durability and capacity [166]. Wu et al. stabilized Ga-Sn alloy in reduced graphene oxide and carbon nanotube framework with self-healing ability and remarkable cycling performance [68]. However, the change between liquid and solid states during cycling causes continuous *SEI layer* growth, which leads to a gradual capacity fade. And most importantly, continuous *SEI layer* growth is not practical in a full cell setup with limited lithium resources. To address this issue, the electrolyte used in batteries involving LM anode should be stable on the LM surface. Solid-state electrolytes have shown much better stability than their liquid counterpart. Recently, Jin et al. have reported solid electrolyte-based molten lithium battery systems operates at 200 ℃ constructed with a molten lithium anode, a molten cathode, and a garnet-type $Li_{6.4}La_3Zr_{1.4}Ta_{0.6}O_{12}$ (LLZTO) solid electrolyte tube [167, 168]. Polymer-based solid electrolyte cooperates with cathodes have been studied previously [169, 170]. Compared to the solid-solid interface in traditional solid-state batteries, the liquid-solid interface facilitates rapid ion transport, leading to high power and long cycle life battery systems. To this end, LMs with room temperature melting point in solid electrolyte battery systems have not been widely explored. The objective of this paper is to investigate a liquid Ga-Sn alloy system that has a melting point around room temperature incorporated with a solid electrolyte in rechargeable lithium batteries.

In this study, Poly(ethylene oxide) (*PEO*) was chosen to be the solid electrolyte due to its flexibility and higher safety characteristics [171]. The liquid Ga-Sn alloy has a weight ratio of 92:8,

which yields a eutectic melting point of 25 °C. By using PEO solid electrolyte instead of liquid electrolytes, the safety of the battery is further enhanced. In order to achieve the optimum conductivity of the PEO electrolyte, the cells were tested at 60 °C. The Ga-Sn liquid metal half cells show an initial specific capacity of 682 mAh g^{-1} and a specific capacity of 462 mAh g^{-1} in the 2nd cycle. The morphology change of LM particles during cycling was evaluated by SEM characterizations. The crystalline and chemical evolutions were monitored via operando X-ray diffraction (XRD) and X-ray absorption near edge spectroscopy using synchrotron-based transmission X-ray microscopy (TXM) with energy scan at the Advanced Photon Source (APS) at Argonne National Laboratory (ANL).

5.3   Experimental section

5.3.1   Materials

Lithium bis(trifluoromethanesulfonimide) (LiTFSI, $LiN(CF_3SO_2)_2$, 99%, Acros Organics), gallium-tin alloy (Ga-Sn, 92:8 wt%, Alfa Aesar), Tin powder (Sn, 500 nm, 99.9% trace metals basis, US Research Nanomaterials Inc), MesoCarbon MicroBeads graphite powder (MCMB, ~10 um, 99.96%, MTI corporation), poly(ethylene oxide) (PEO, Mw ~ 600,000, Sigma Aldrich), sodium dodecyl sulfate (SDS, ≥98.5%, Sigma Aldrich), super C65 (conductive carbon black, Timcal), acetonitrile (C_2H_3CN, 99%, Acros Organics) and silica (SiO_2, fumed powder, 0.007 μm, Sigma Aldrich) were purchased and used as received.

5.3.2   Preparation of liquid alloy anode, Sn and MCMB electrodes

The LM alloy was added into a small vial followed by adding sodium dodecyl sulfate (SDS) as surfactant and acetonitrile as solvent (1 mg SDS added cooperated with 50 mg LM alloy). The SDS surfactant was used to reduce the size of the LM particles during sonication reported in the literature [166]. The mixture was heated at 40 °C on a hot plate for 30 min. Then the large LM droplets were ultrasonicated into small LM particles by using a probe ultrasonication (sonics vibracell VC505 sonicator) for 5 min by setting each pulse of 2 s followed by 2 s off. After the ultrasonication, the suspension was further sonicated in a beaker for 20 min with cold water for cooling down. Then super C65 carbon black and PEO binder were added into the suspension with

a mass ratio of 5: 3: 2. Then LiTFSI was added into the slurry with an appropriate ratio of EO: Li = 20:1 in an Ar-filled glovebox. The slurry was magnetically stirred for 24 h on a stir plate. The slurry was cast onto a copper (Cu) foil using a doctor blade and then dried at 75 ℃ for 24 h in a vacuum oven. For comparison, Sn and MCMB electrodes were fabricated from a 5: 3: 2 (mass ratio) mixture of active material (Sn or MCMB), carbon black, and PEO binder. A Ga-Sn LM composition test was performed for comparison as well by utilized a mass ratio of 8: 1: 1 and 3: 4: 3. The slurry was homogeneously blended by a magnetic stir bar for 24 h, cast on a copper foil using a doctor blade, and dried at 75 ℃ for 24 h under vacuum condition. All the dried electrodes were cut into ~0.97 cm^2 discs (D=11 mm) and transferred into an Ar-filled glovebox for further handling and testing.

5.3.3 Preparation of PEO solid electrolyte

0.88 g PEO and 0.287 g LiTFSI (amounts based on the ratio of EO: Li = 20:1) were dissolved in 9 mL acetonitrile followed by adding 58 mg SiO_2 nanoparticles and stirred for 24 h at room temperature in an Ar-filled glovebox. The mixture was poured onto a PTFE plate and then cast by a doctor blade, then dried inside the Ar-filled glovebox for 6 h. The dried membrane was taken out of the glovebox and cut into 2.83 cm^2 circular disks (D = 19 mm) and further dried at 60 ℃ for 24 h in a vacuum oven. The dried PEO solid electrolyte was transferred into an Ar-filled glovebox for further handling.

5.3.4 Cell fabrication and electrochemical evaluation

CR2032 Coin cells were used and cells were fabricated in an Ar-filled glove box. First, a stainless-steel plate was placed in a coin cell case. A Ga-Sn electrode was placed on the plate with the copper side facing down. Then a PEO solid electrolyte was placed on the top of the electrode followed by adding a piece of lithium metal on the PEO solid electrolyte. Finally, a stainless-steel plate covered the lithium metal with a piece of spring as the spacer. The cell was crimped reaching the pressure of 1000 psi and taken out of the glove box for electrochemical evaluation.

Cells were tested at 60 ℃ in an Espec environmental chamber connected to an Arbin BT2000 battery cycler. Cells were initially rested for 30 min, then galvanostatically cycled at C/20 rate (1C = 787 mA g^{-1} for Ga-Sn alloy (92:8 by weight), based on the mass of material in the cells)

and in voltage ranges of 0.005-2.0 V. Cyclic voltammetry (CV) was performed at 60 °C on a BioLogic VSP potentiostat connected to the Espec environmental chamber. The potential was swept from open-circuit voltage to 0.005 V and then swept back to 2.0 V at a scanning rate of 0.02 mV s^{-1}. AC impedance was scanned via BioLogic VSP from 500kHz to 0.1Hz with an amplitude of 5 mV.

5.3.5 Operando coin cell assembly

The CR2032 coin cells were modified and used in this study. 2 mm diameter holes were punched at the center of both anode and cathode cases with 30 µm thick Kapton tape sealed the hole on both sides of the case. The current collector with a 2 mm hole was to maximize the contact of the electrode. The electrode was placed on the collector followed by adding 15 µL 1M LiTFSI in DME/DOL electrolyte. A Celgard 2400 separator was placed on top of the electrode with an additional 15 µL electrolyte on top of it. A piece of lithium metal with 1.27 mm in diameter was laid on the separator followed by a stainless-steel plate (with a 2 mm hole at the center) and a wave spring. The cell was crimped and taken out of the glove box for electrochemical evaluation. Operando coin cells were cycled at room temperature.

5.3.6 Synchrotron-based X-ray diffraction

The operando XRD experiment was conducted at beamline 11-ID-C of the APS with a photon wavelength of 0.1174 Å and an energy of 105.6 keV. The incident beam size employed on the sample was 50 µm * 50 µm. Measurements were carried out in transmission mode. The detector was located 1500 mm from the sample. The scattering intensity was detected on a 2D Perkin-Elmer detector with a pixel size of 200 µm (2048 * 2048 pixels). Both of Ga-Sn and pure Ga coin cells were cycled at a constant current rate of 0.1 C. The diffraction data for each sample were collected each 32 min interval. The exposure time was 0.5 s and 40 captures were averaged for each data collection. The 2D diffraction patterns generated via operando XRD were calibrated using a standard CeO_2 sample and converted to 1D patterns via Fit2D software.

5.3.7 Synchrotron-based transmission X-ray microscopy

The operando transmission X-ray microscopy experiment was conducted at beamline 32-ID-C of the APS equipped with a Si 111 double crystal monochromator which enables an energy resolution of $\triangle E/E$ equals 10^{-4}. The transmission X-ray radiographs periodically record a series of TXM images at different energies with a pixel size of 32.3 nm for the targeted electrode during cell operation. The energy steps were 5 eV for pre-edge from 10300 to 10335 eV, 1.5 eV for XANES range between 10335 and 10420 eV, and 4 eV for post-edge after 10420 eV. Each TXM dataset contains an overall 78 images for TXM-based XANES analysis. Flat and dark images were also recorded at each energy for normalization followed by a $2 \times 2 \times 2$ three dimensional median filter. The XANES spectra were obtained by using the optical density changes of the active materials and analyzed via Athena software.

5.3.8 Scanning electron microscope

The morphological characterization of the electrodes was conducted with a JEOL JSM-7800F field emission SEM. The elemental mapping was performed with energy-dispersive X-ray spectroscopy (EDS) attached to the SEM with 7 keV.

5.4 Results and discussion

Both Ga and Sn have high theoretical specific capacities of 769 mAh g^{-1} and 993 mAh g^{-1}, respectively. Therein, the Ga-Sn LM alloy with its weight ratio of 92:8 for Ga over Sn applied in this contribution has a calculated theoretical capacity of 787 mAh g^{-1}, which is slightly higher than twice that of commonly used graphite anode. The Ga-Sn LM alloy has a melting point of 25 ℃, which is exactly at the typical room temperature (RT). Also, it has been mentioned that the Ga-Sn LM alloy usually has a super-cooling capability for 5-6 ℃ below its melting point in ref [68], in which the alloy can remain as a liquid at RT conditions even though its melting point is 25 ℃. The liquid Ga-Sn LM alloy was originally placed in a coin cell case at RT, as shown in **Figure 5.1a**. It was initially a bulk liquid metal with a smooth and glittery surface because of light reflections. After discharge, the Ga-Sn alloy faded into ragged and black solid cracks due to the large volume expansion during the full lithiation process. The volume expansion is 160% and 260% for Ga and Sn, respectively. Therefore, it is expected to have an approximate twice expansion for the Ga-Sn

alloy after lithiation. The Ga-Sn alloy was partially recovered to smooth and glittery liquid metals after the delithiaton process with parts of the alloy remains at expanded and fractured status due to the loss of connection with PEO solid electrolyte after full lithiation, therefore, fails to release lithium during the delithiation process. Using bulk Ga-Sn LM alloy will cause difficulty and deterioration for alloy recovery after lithiation. Therefore, making Ga-Sn LM alloy into Ga-Sn liquid metal nanoparticles (LMNPs) via super ultrasonication and surfactant additives helps nanoparticles maintain contact with conductive carbon and LiTFSI salt. After ultrasonication of bulk liquid metals into LMNPs, the small particles help to effectively accelerate the diffusion process and reinforce contacts as described in **Figure 5.1b**. The LMNPs expand to larger particles due to the volume expansion after lithiation. During the delithiation process, the particles deform into random shapes because of the large volume changes and inhomogeneity of lithium concentration inside the LMNPs. However, after full delithiation where the condition returns to the formation of liquid metal, the particles reach liquid phases and self-heal themselves to regenerate LMNPs.
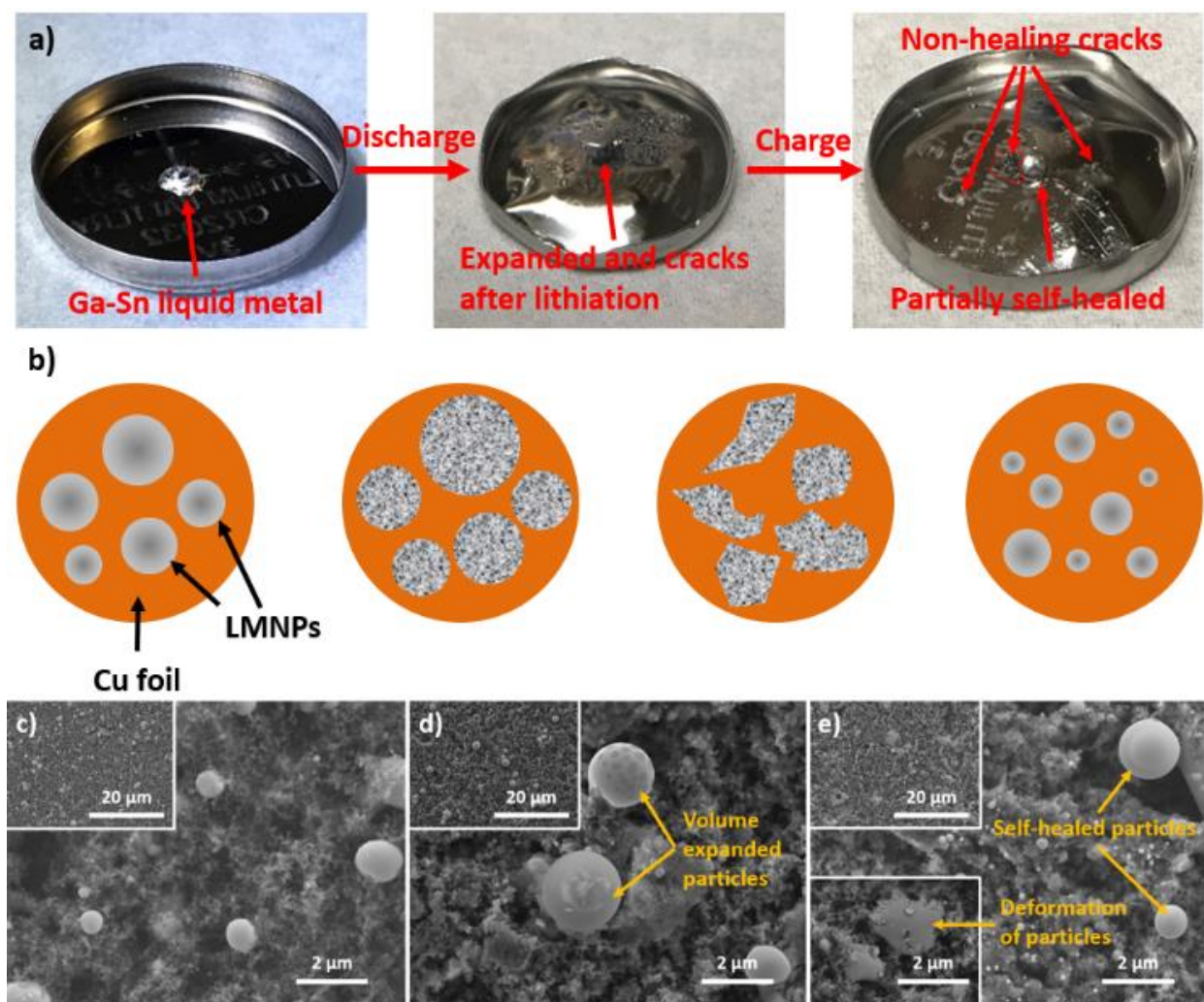
Figure 5.1 (a) Ga-Sn liquid metal at the pristine, discharged, charged state. (b) Reaction schematics of LMNPs during lithiation and delithiation processes. SEM images of (c) pristine Ga-Sn LMNPs electrode, (d) lithiated Ga-Sn LMNPs electrode, and (e) delithiated Ga-Sn LMNPs electrode with a low magnified image at the upper left corner.

The morphological changes during lithiation and delithiation were observed by SEM. The initial as-prepared LMNPs electrode was observed to have multiple nm-sized spherical particles as shown in **Figure 5.1c** with an inset image showing low magnified electrode morphology. The EDS scanning in **Figure 5.2** shows the overlap mapping, elemental mapping of carbon, oxygen, and Ga-Sn alloy, respectively. The formation of spherical nanoparticles is due to the high surface tension of the Ga-Sn alloy droplet. The SEM image shows that the Ga-Sn particles were well connected to carbon additives, LiTFSI salt, and PEO, which provides the transport of lithium ions and electrons. After full lithiation, the LNMPs were observed to have large volume expansions by

70

assimilating lithium into the Ga-Sn alloy lattice as shown in **Figure 5.1d**. The SEM image in **Figure 5.1e** displays the formation of smaller and glittery surfaced Ga-Sn particles after the delithiation process with some of the delithiated Ga-Sn particles occupied non-spherical shape highlighted in the bottom left image. The lower inset SEM image reveals the deformed particles could be potentially due to the reduced surface tension by partially dealloying lithium ions.
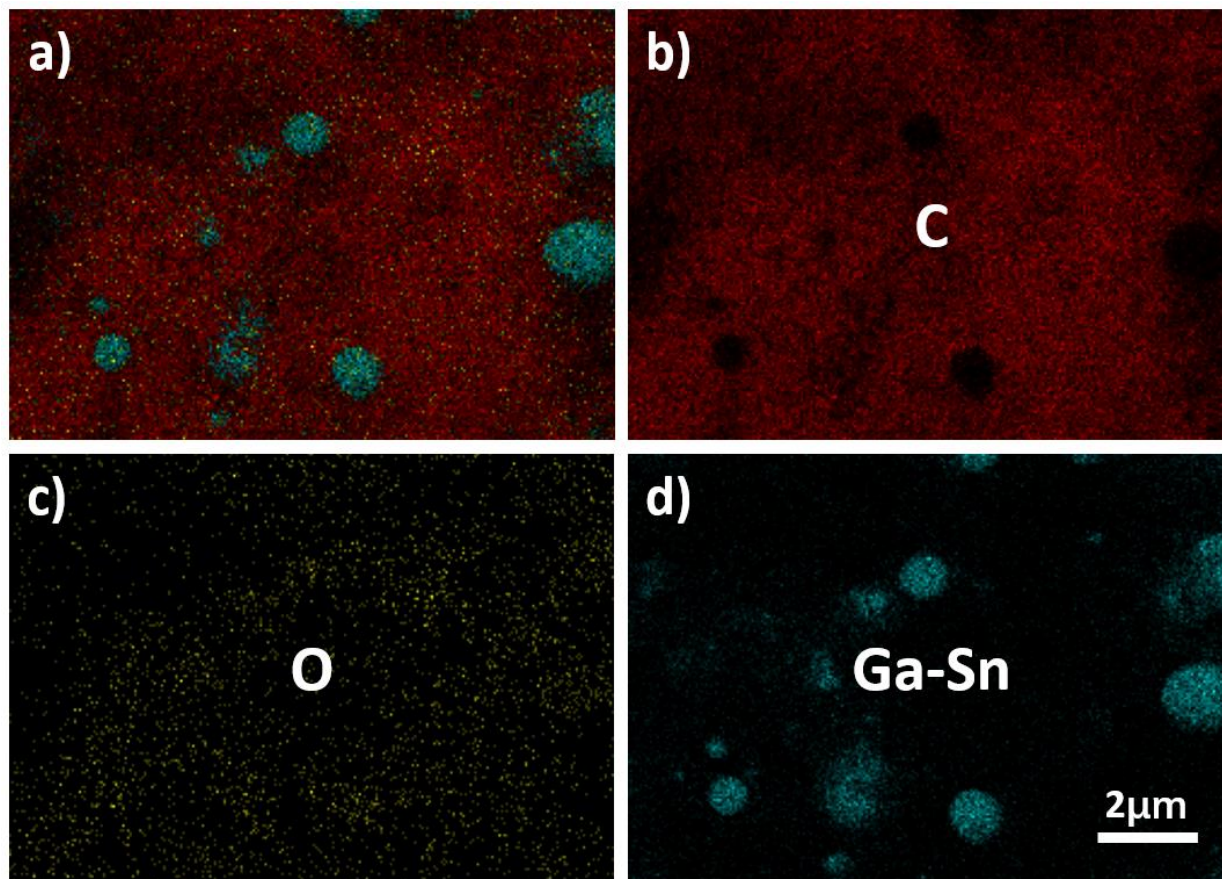
Figure 5.2 EDS images of a fresh Ga-Sn electrode collected at 7 keV. (a) overlap EDS mapping. (b-d) EDS scan for carbon, oxygen, and gallium-tin.

To understand the lithiation mechanism for Ga lattice in Ga-Sn alloy nanoparticles, synchrotron-based TXM and XRD were employed under the operational condition as advanced characterizations. Because of the lack of heating capability at the synchrotron X-ray stations at the APS, 1 M LiTFSI in DME : DOL (50:50) liquid electrolyte was used for the operando XRD and TXM experiments. The voltage profile in **Figure 5.3a** shows the first cycling process at 0.1 C of the LMNP electrode with red dots indicating when the TXM images were collected. Each image stack contains a series of two-dimensional transmission X-ray microscopy images as well as the

energy information where each frame was collected. The intensity spectrum at each energy was normalized to generate the X-ray absorption near edge spectroscopy (XANES) datasets as shown in **Figure 5.3b**. The XANES spectrum with a white line position of 10372 eV at the pristine state rather than 10375 eV for gallium (III) indicates the LMNPs were gallium (O) after preparation [74, 172]. Once the lithiation proceeded, the normalized intensity of XANES spectra shifted to higher energy and became broader gradually after the voltage reached 0.75 V plateau as lithium ion intercalated with a formation of Li_2Ga_7. After the voltage reached 0.5 V, the spectra displayed an even broader shape corresponding to the formation of the LiGa phase. After the 0.5 V plateau, the voltage gradually reduced to 0 V without a plateau for Li_2Ga, which indicates that Li_2Ga crystal was not formed. The shift of Ga K-edge to higher energy from Ga to Li_2Ga_7 and LiGa could be due to the increased oxidation state and /or reduced screening effect, which is similar to the lithiation process of selenium [145, 173]. The XANES spectrum also shows that the absorption peak continuously broadens until the end of lithiation. We believe that lithium was still inserted into Li_xGa to make x greater than 1. However, crystalline Li_2Ga was not formed. The diminishing of the peak at 10372 eV is an indicator of lithium ion intercalation and the formation of Li_xGa type alloy. The broadening of the peak shape means that the electrons in Ga are less confined [174], which could be due to the amorphization process or crystal lattice increase. The spectrum after lithiation does not have a bimodal appearance demonstrates the final product is not Li_2Ga yet. During the process of delithiation, the lithium ion was extracted from the system, The Li_xGa phase was first delithiated back to LiGa and Li_2Ga_7 thereafter as the spectra were reinstated back to a sharper shape. The last gallium spectrum was able to recover back to its original sharp appearance at the end of the delithiation process with an identical shape and white line position as its pristine state, which indicates the chemical composition of Ga-Sn LMNPs has been fully recovered.
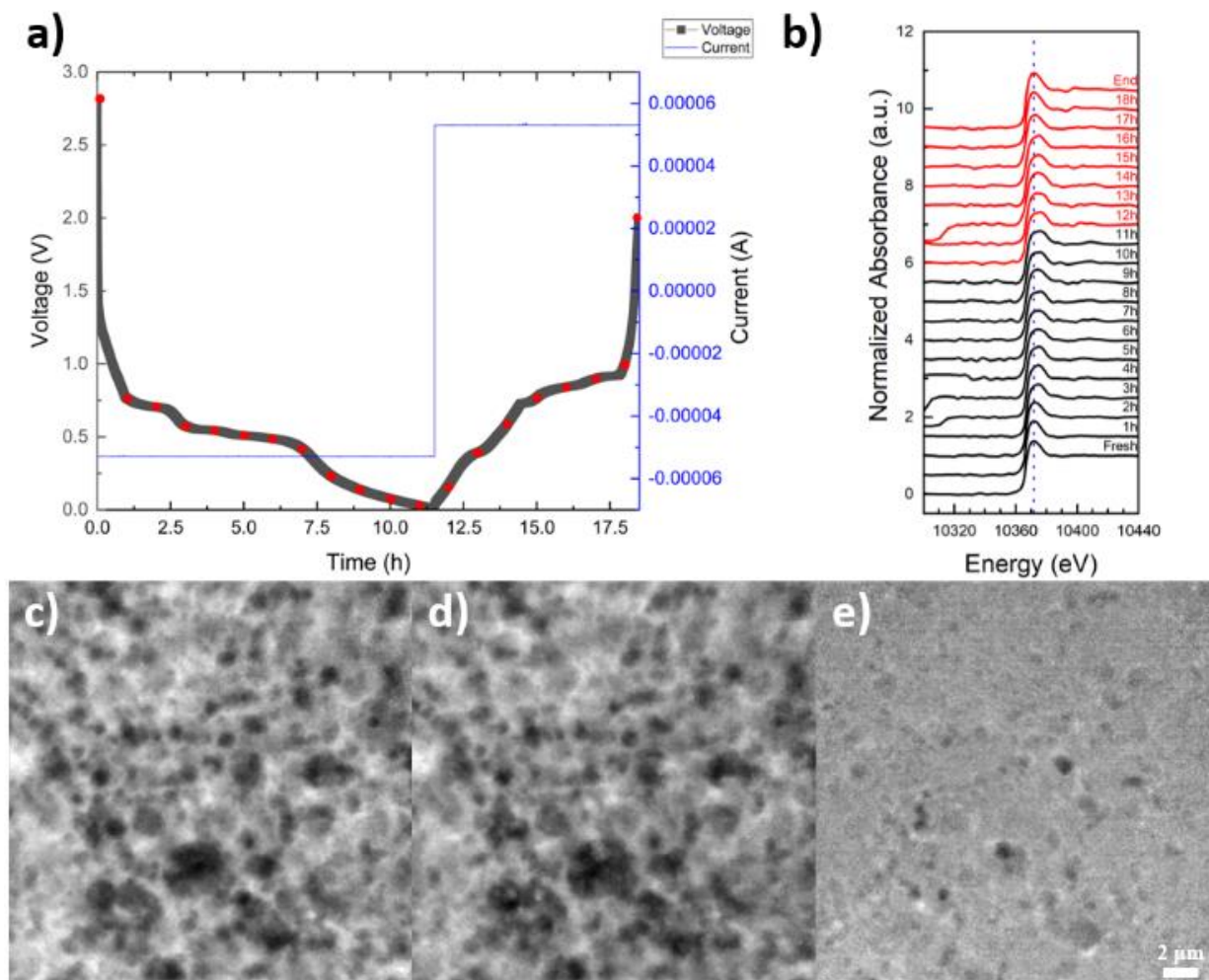
Figure 5.3 Operando TXM results for Ga-Sn LMNPs. (a) Voltage and current plots with highlighted data collecting points. (b) gallium XANES results during lithiation (black) and delithiation (red) processes. (c) TXM image of the pristine Ga-Sn LMNPs electrode. (d) TXM image of the delithiated Ga-Sn LMNPs electrode. (e) differences between (c) and (d) by image registration and subtraction.

To investigate the morphological changes of LMNPs, image registration and subtraction were performed by using two images (one of each as shown in **Figure 5.3c-d**) from the pristine and the end of delithiation. The differences between these two images (black spots in **Figure 5.3e**) indicate only a few large particles possess irregular shape after delithiation while most of the LMNPs were able to restore their original shape and positions during the cycling process, which is consistent with the SEM results shown in **Figure 5.1**. The particle size analysis based on ex-situ SEM images is shown in **Figure 5.4**. Before lithiation, the fresh Ga-Sn alloy electrode contains

mostly small nm-sized particles. The nm-sized particles were initially obtained from the Ga-Sn alloy bulk via the ultrasonication process and surfactant which ensure possible good contact with the carbon and lithium salt (LiTFSI), as well as effective lithiation reactions. The amount of nm-sized Ga-Sn particles decreases as lithiation proceeded, which was due to their volume expansions. Once the battery was fully charged, the population of small particles increased again. This ex-situ experiment contains discrepancies due to the variations on each different electrode but provides some insights into morphological evolutions of the Ga-Sn system. The overall morphological changes indicate a promising reversible lithiation/delithiation process for the use of LMNP electrodes.
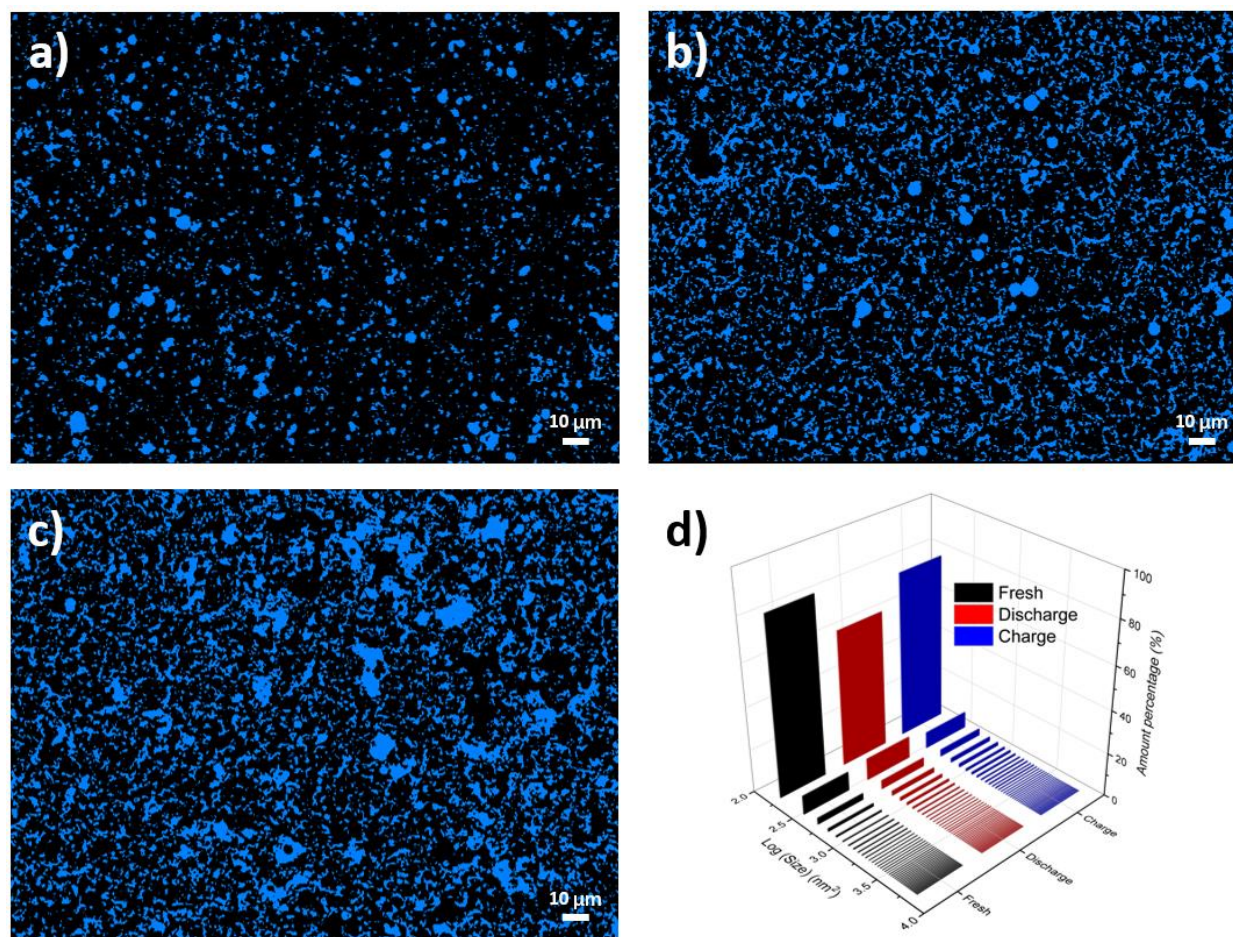
Figure 5.4 Estimations of particle size distributions based on two-dimensional SEM images at (a) pristine, (b) discharged, (c) and charged status. (d) particle size distributions are shown as percentages.
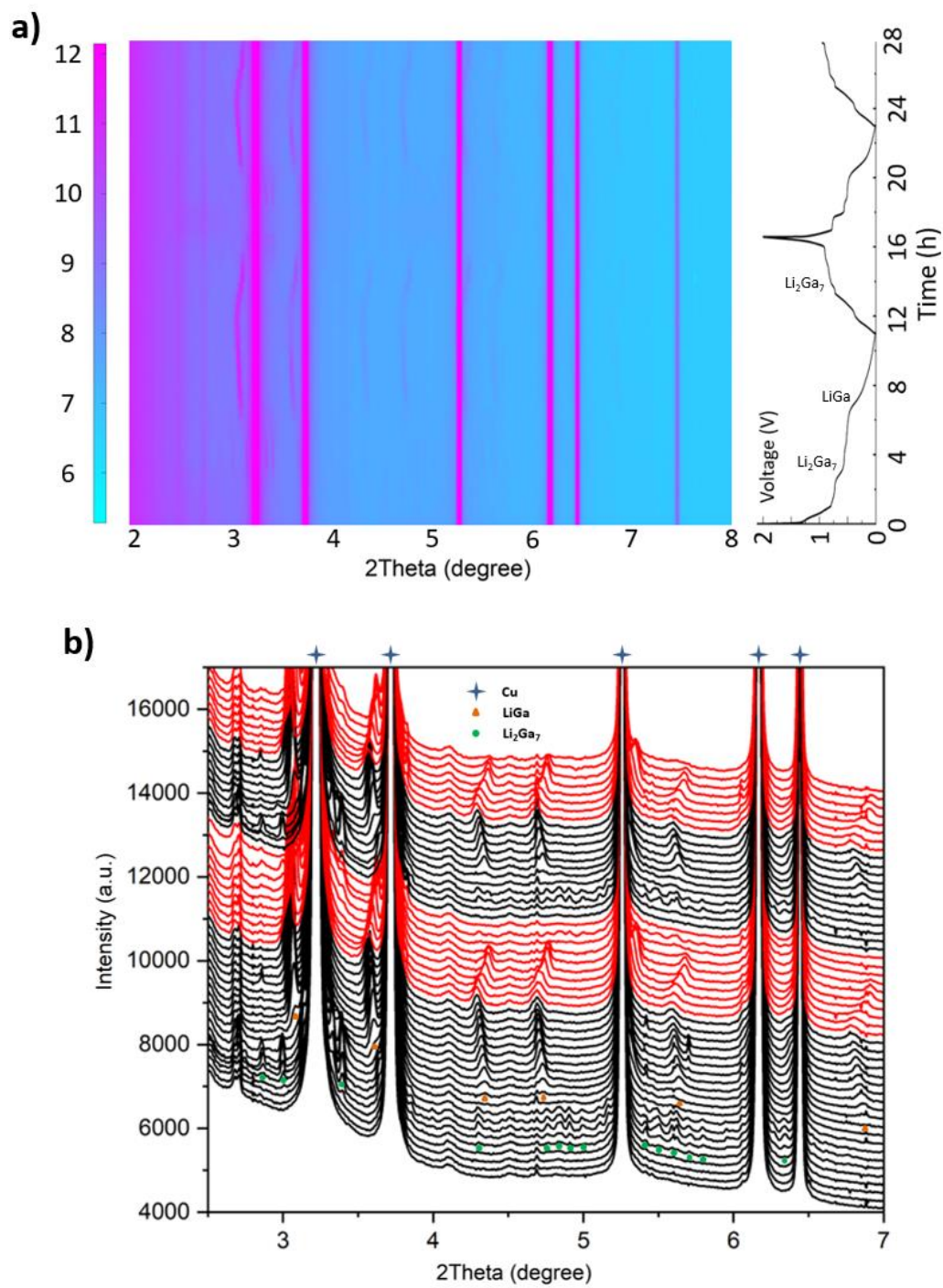
Figure 5.5 (a) The operando XRD results with potential plot and (b) elected XRD patterns by 32 min time step.
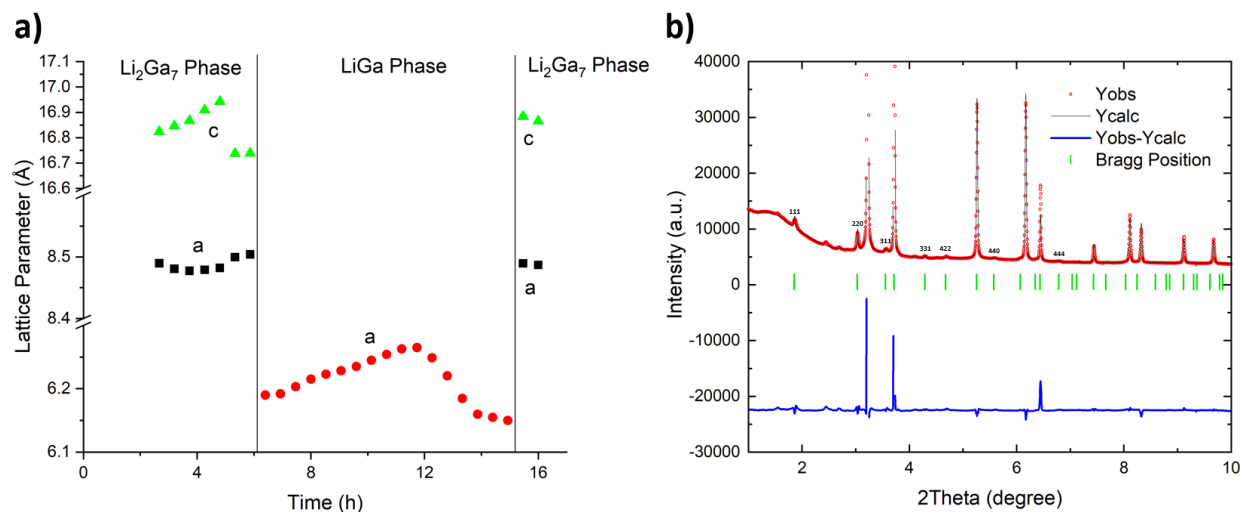
Figure 5.6 (a) Lattice calculations of Li_2Ga_7 and LiGa phases. (b) confirmation of the LiGa phase at the end of lithiation.

To further understand the phase and morphological changes observed via the TXM experiment, an operando XRD experiment was conducted. As shown in **Figure 5.5**, the Ga-Sn LMNPs do not have diffraction patterns due to the nature of liquid metal at the very beginning. The LMNPs started to form Li_2Ga_7 as the lithiation process proceeded to below the plateau of 0.75 V. Afterward, we observed the disappearance of Li_2Ga_7, and thereafter the formation of the LiGa phase at 0.5 V. Both of these two observations were consistent with the TXM results. Instead of forming the orthorhombic Li_2Ga phase at the end of the discharge process based on the calculations shown in **Figure 5.6**, we found that all the LiGa patterns shifted to smaller two theta values. This phenomenon indicates the increases of the lattice parameter of LiGa crystal during lithiation, which is also consistent with the peak broadening after the 0.5 V plateau in the XANES spectrum. Previous studies had demonstrated the formation of Li_2Ga from LiGa is a structural transition from a three-dimensional structure to a two-dimensional structure. This transition could cause atomic bond breakage and rearrangement of atoms which means a reaction of this kind is not likely to take place without enough kinetic conditions such as very low current and high temperature [175, 176]. The formation of a new discrete phase yields a steady potential over the range in which one solid phase is being converted into another followed by an abrupt change in potential when the reaction is completed. In contrast, the lithiation process with a gradual change in potential from 0.5 V to the end of lithiation is a process of solid solution formation [175]. The operation conditions were constant current at 0.1 C and room temperature for the TXM and XRD

76

experiments, which cannot form the Li_2Ga phase. During the process of delithiation, the extraction of lithium ions from the LiGa phase leads to the decrease of its lattice parameter that is demonstrated by the shifting of LiGa patterns to the larger two theta values. It also indicates that the solid solution formation in LiGa crystal is reversible. Li_2Ga_7 phase was formed after the disappearance of LiGa at the end of delithiation. The operando XRD of the second cycle behaves identically as the first cycling performance. There was no observation of any Li_xSn phases among its first two cycles implies either the small portion of Sn is below the detecting limit or the main effect of 8% Sn is to reduce the melting point of LMNPs without influencing the crystal structures of Ga or participating in the electrochemical reaction during cycling. For verification, we have also conducted another operando XRD experiment by employing pure Ga LMNPs under the same operational condition showing the same result as displayed in **Figure 5.7**.
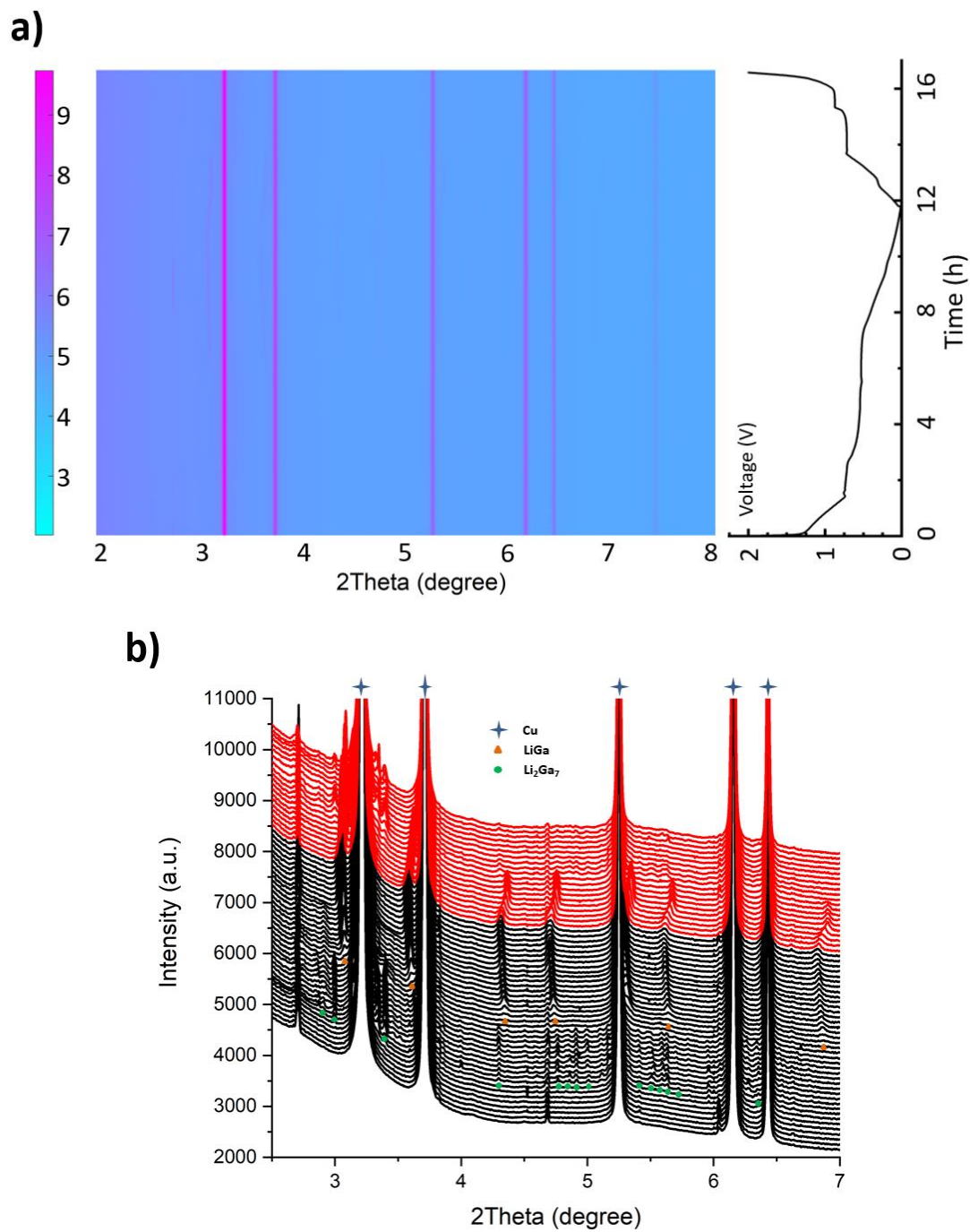
Figure 5.7 (a) Operando XRD result for pure gallium electrode cycled at 0.1 C rate with potential plot and (b) selected XRD patterns by 32 min time interval.
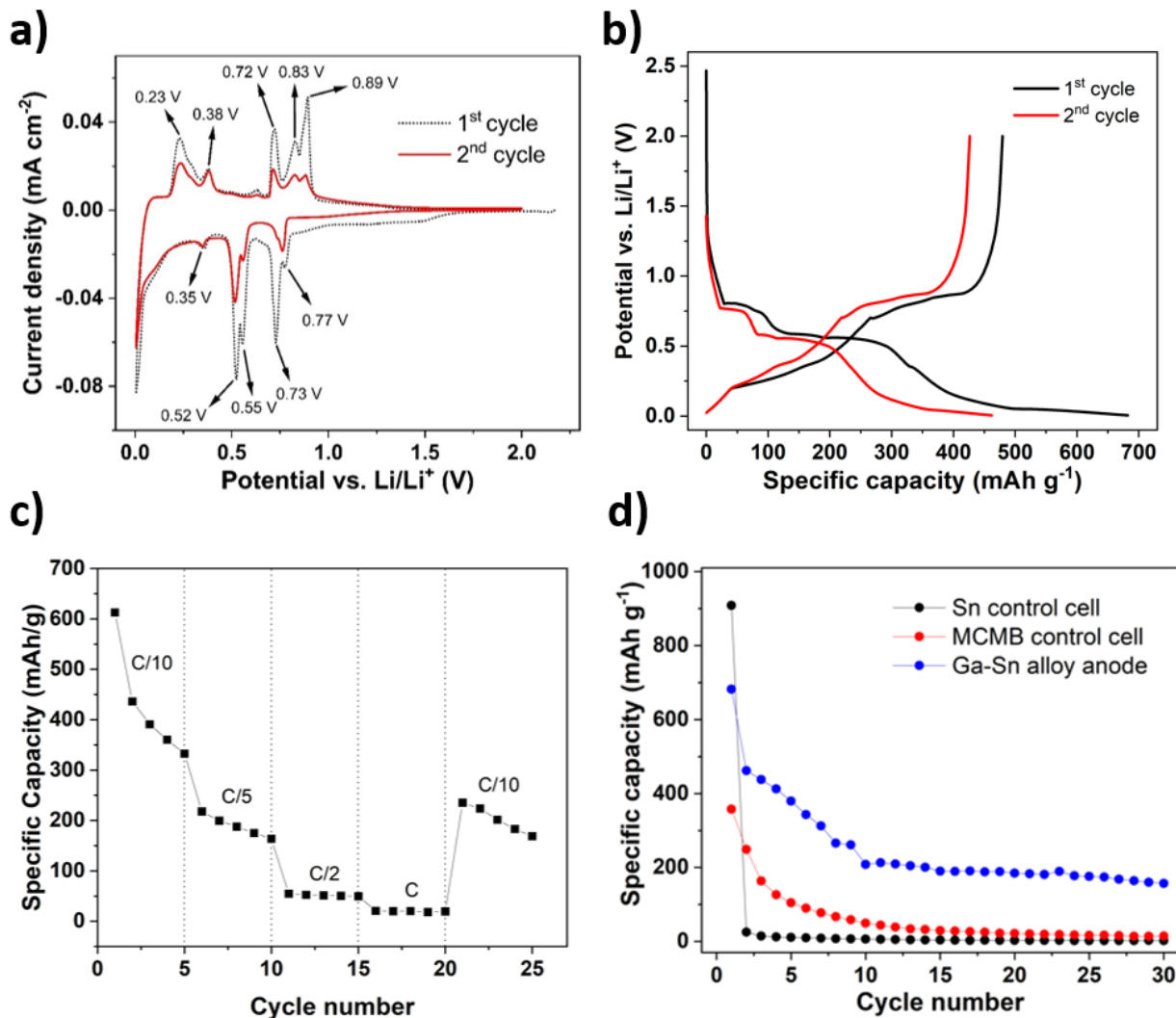
Figure 5.8 (a) Cyclic voltammetry of a Ga-Sn LMNPs electrode tested at 60 °C. The potential was swept from open-circuit voltage to 0.005 V and then swept back to 2.0 V at a scanning rate of 0.02 mV s-1. (b) Potential capacity plots of the Ga-Sn LMNPs electrode tested at 60 °C. The cell was galvanostatically cycled at C/20 rate in a voltage range of 0.005-2.0 V. (c) Rate performance of the Ga-Sn LMNPs electrode tested at 60 °C. (d) Comparison of Ga-Sn LMNPs electrode with Sn and MCMB electrodes under the same operating conditions.

The electrochemical behavior of the LMNPs with a PEO solid electrolyte was evaluated by cyclic voltammetry (CV) in lithium half cells operated under 60 °C swept at 0.02 mV s^{-1}, as shown in **Figure 5.8a**. In the cathodic scan from the open-circuit voltage (OCV) to 0.005 V, the first obvious difference is the lack of a peak at 1.2 V for SEI formation, which is different from the CV curve using the liquid electrolyte. The lithium insertion mainly occurs at 0.73 and 0.52 V for Ga with another three small peaks at 0.77, 0.55, and 0.35 V correspond to the gallium bond

cleavage associated with the formation of Li_2Ga_7, LiGa, and Li_2Ga, respectively. The anodic lithium extraction processes occur at 0.23, 0.38, 0.72, 0.83, and 0.89 V for the reverse process from Li_2Ga to LiGa followed by Li_2Ga_7 and eventually back to Ga-Sn LM. The high-temperature CV result with PEO electrolyte shows Sn does not participate in any electrochemical reactions, which is consistent with the operando XRD experiment. We also conducted ex-situ XRD to understand the phase changes of LMNPs in the solid electrolyte cell. As shown in **Figure 5.9**, only the Li_2Ga phase appeared after full lithiation and no Li_xSn phases were observed during cycling. The lithium ion diffusion rate is two orders of magnitude higher in Ga LM compared to that in Sn at 60 ℃ [163]. Therefore, it is difficult for this small amount of Sn to form any Li_xSn phases during cycling processes. If the 8% Sn does not participate in the electrochemical reaction, the theoretical capacity of the Ga-Sn LM is reduced to 707 mAh g^{-1}. As shown in **Figure 4.8b**, a small dip was observed during the first discharge when the potential reaches 0.77V, which means activation energy was required for bond cleavage between Ga-Ga bond and phase formation of Li_xGa as reported in ref [176]. This small portion of Sn doping has the ability to reduce the melting point of Ga-Sn LMNPs which benefits the crystalline evolutions of the Ga phase. Compared with the previous study reported by Saint et al., the formation of the Li_2Ga phase mainly occurs once the voltage reaches 0.01V, which needs more kinetic energy satisfied by either very low current or high temperature. Consequently, we are able to observe the formation of Li_2Ga as shown in **Figures 5.8a** and **5.9** when we operate the cells at 60 ℃ but not for the operando experiments conducted at room temperature. The Ga-Sn anode electrode was also tested under variable C-rates as shown in **Figure 5.8c**. The electrode shows an initial specific capacity of 614 mAh g^{-1} at C/10 followed by 437 mAh g^{-1} for the second cycle. The cell exhibits stable cycling performance with a specific capacity of 218 mAh g^{-1} at C/5. The capacity reduced to 55 mAh g^{-1} and 21 mAh g^{-1} at a higher C-rate of C/2 and C, respectively. The capacity was able to recover back to 236 mAh g^{-1} at C/10 thereafter. The low capacity at C/2 and 1 C rates are mainly because of the low ionic conductivity of PEO solid electrolyte and the high interface resistance between the Ga-Sn particles and the PEO solid electrolyte.
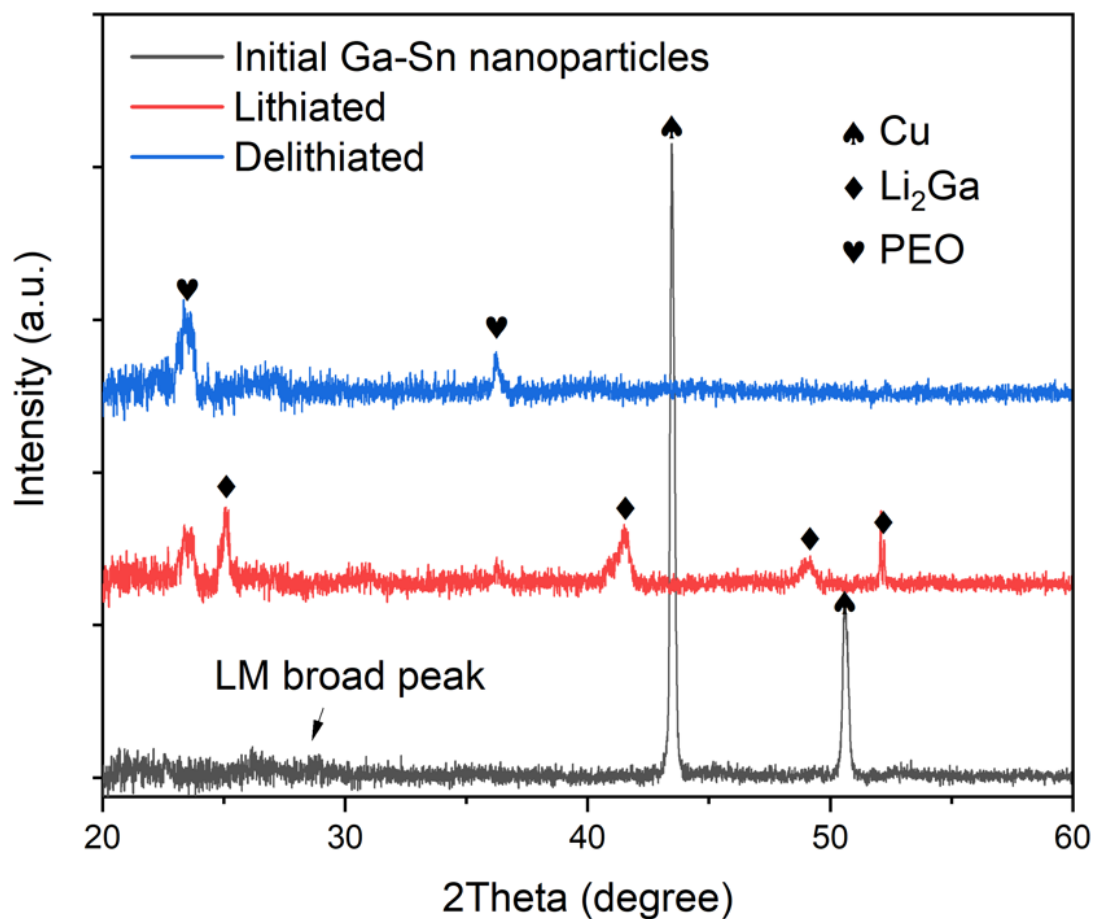
Figure 5.9 Ex-situ XRD results for Ga-Sn LMNPs tested at 60 °C. For the lithiated and delithiated samples, the copper current collector was removed from the electrode to avoid the interference of the strong Cu peaks.
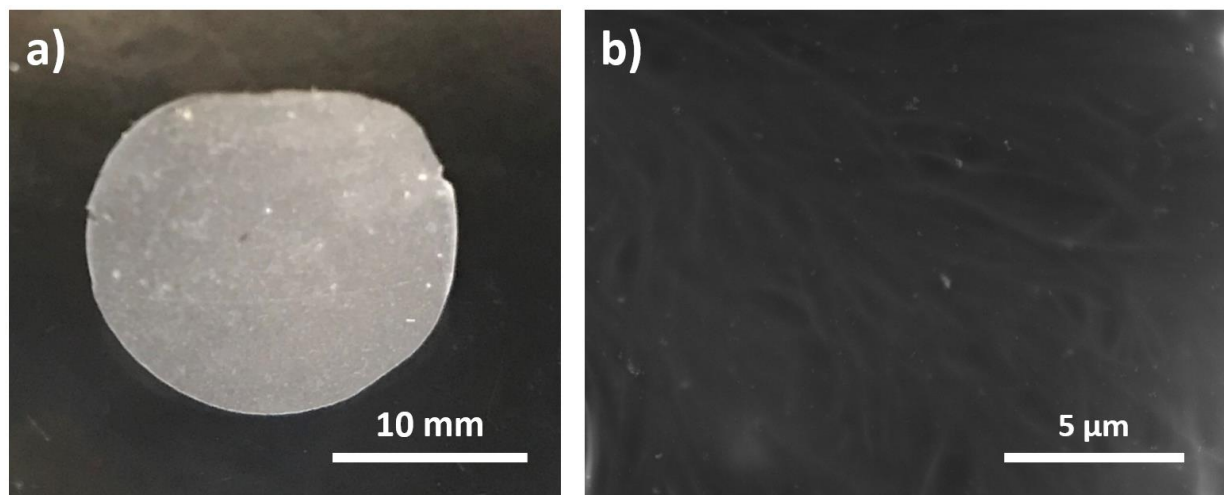
Figure 5.10 (a) A PEO solid polymer electrolyte and (b) its corresponding SEM image.
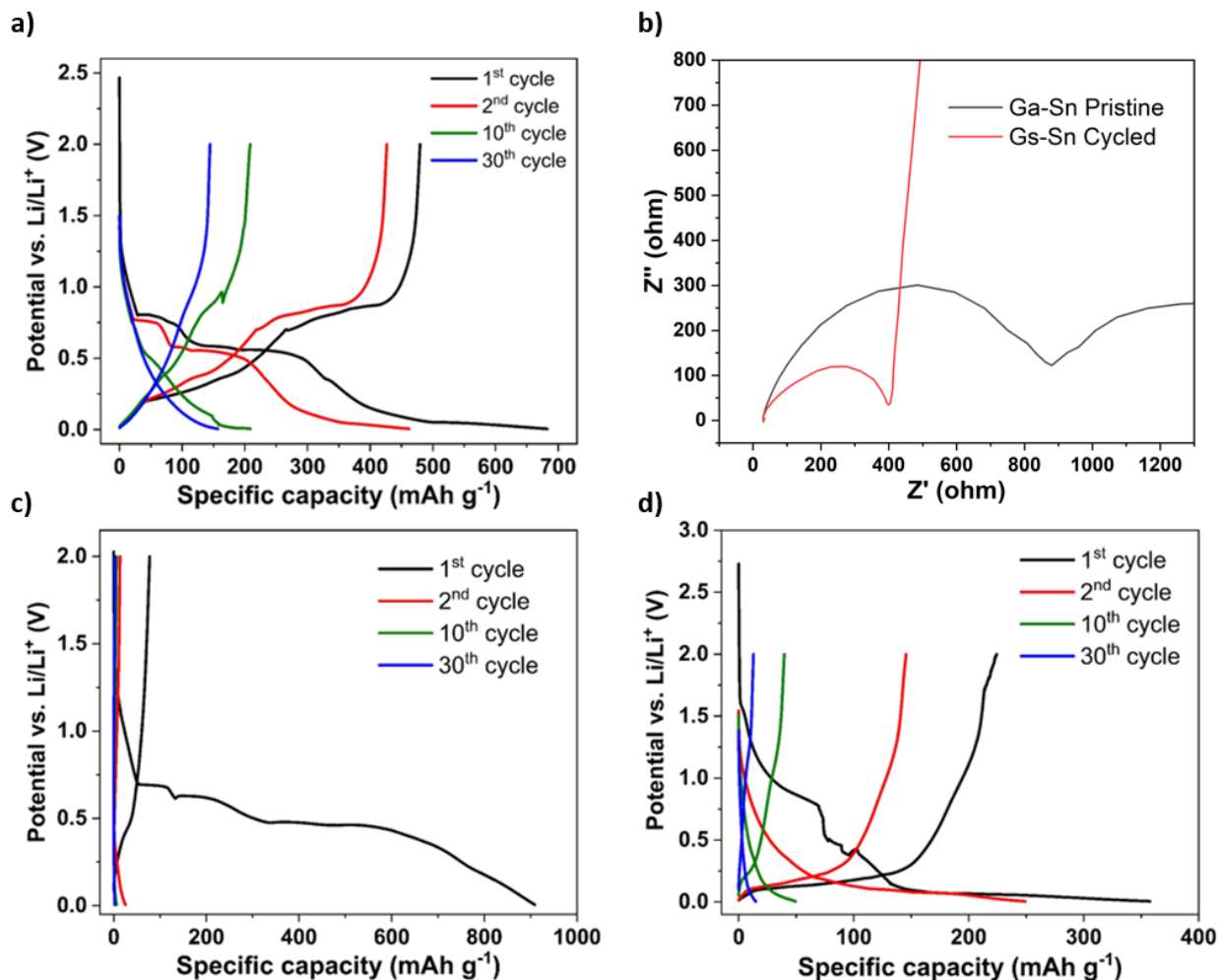
Figure 5.11 The voltage capacity plot of a (a) Ga-Sn LMNP, (c) Sn, (d) MCMB electrode tested at 60 °C for the selected cycles and (b) the electrochemical impedance spectroscopy of a Ga-Sn LMNP electrode before cycling and after 20 cycles tested at 60 °C.

The cycling performance for LMNPs was evaluated by combining a LMNPs electrode with a PEO solid electrolyte to form a full solid half cell tested in an Espec environmental chamber maintained at 60 °C during cycling. The picture of the PEO solid electrolyte is shown in **Figure 5.10** with the SEM image showing its morphology. To highlight the electrochemical advantages of the Ga-Sn LMNPs, its cycling test was compared with the Sn particle electrode (with large volume change) and MCMB electrode (without large volume change) under the same conditions respectively, as shown in **Figure 5.8d**. The selected voltage-capacity plots of Ga-Sn LMNPs, Sn particles, and MCMB electrodes are shown in **Figure 5.11**. The Ga-Sn LMNPs have an initial lithiation capacity of 682 mAh g^{-1} which is corresponding to approximately 87% of the theoretical

capacity. After that, it fades to a lithiation capacity of 462 mAh g^{-1} at second lithiation and retains at 208 mAh g^{-1} in the first 10 cycles. Afterward, it continuously fades to 158 mAh g^{-1} with an increase of resistance after 30 cycles. There is a fast capacity drop (about 70%) during the first 10 cycles. We believe that many Ga-Sn LMNPs lost contact with the PEO solid electrolyte and became inactive. Although the Ga-Sn electrode has the advantageous features of liquid, such as flexibility and fluidity, the large volume change upon cycling is still a big challenge for maintaining the contact between active materials and solid electrolytes. **Figure 5.11b** shows the electrochemical impedance spectroscopy (EIS) of a Ga-Sn LMNP electrode before cycling and after 20 cycles tested at 60 °C. The charge transfer impedance (the first semi-circle) increased about 100% after the cycling, which indicates that many Ga-Sn particles lost the connection with the PEO electrolyte and become inactive during cycling. The cycling results also show that the capacity drop is mitigated after the first 10 cycles. The capacity drops from the 10th cycle to the 30th cycle is about 7% of its originally delivered. It indicates that Ga-Sn LMNPs have a possibility to maintain contact with PEO solid electrolytes with a future optimized microstructural design of the electrode. For instance, we can optimize the nano-particle fabrication method to narrow the distribution of the particle size and add more pressure to the electrode. The Sn particle electrode was tested as a baseline. It has an initial lithiation capacity of 909 mAh g^{-1} and then rapidly fades to 25 mAh g^{-1} at the 2nd cycle. The capacity drop is over 97%. It is not surprising because of the large volume change of Sn during the first cycle deactivated most of the particles. MCMB was also tested as a baseline experiment, in which the MCMB electrode has an initial lithiation capacity of 358 mAh g^{-1}. Subsequently, it fades to 249 mAh g^{-1} at the 2nd cycle with continuous capacity fading to 49 mAh g^{-1} in the first 10 cycles and eventually retains at 15 mAh g^{-1} after 30 cycles. The capacity drop is about 86% during the first 10 cycles and another 9% was lost from the 10th cycle to the 30th cycle. By comparing with Sn and MCMB electrodes, it is clear that the liquid metal electrode can maintain better contact with PEO solid electrolytes, mainly due to its advantageous features of the liquid. However, the liquid metal undergoes a liquid-solid-liquid transition during cycling, which can lead to the gradual loss of contact upon cycling. A different mass ratio of Ga-Sn electrodes was conducted to investigate their cycling performances. The batteries were tested under the same temperature and rate conditions as mentioned previously. As shown in **Figure 5.12**, all the samples delivered similar initial specific capacities for their first and second cycles. Reducing the mass ratio of Ga-Sn to 30% slightly increases its reversible

capacity after 10 cycles. On the opposite, increasing the percentage of Ga-Sn to 80% results in a much larger capacity decay after the third cycle and delivered a limited capacity after 10 cycles. Therefore, maintaining good contact between Ga-Sn LMNPs and the PEO solid electrolyte during cycling is a potential problem for high loading liquid metal anodes. These problems could be solved by several potential approaches, such as optimizing the microstructure of the electrode and maintaining larger pressure on the electrode.
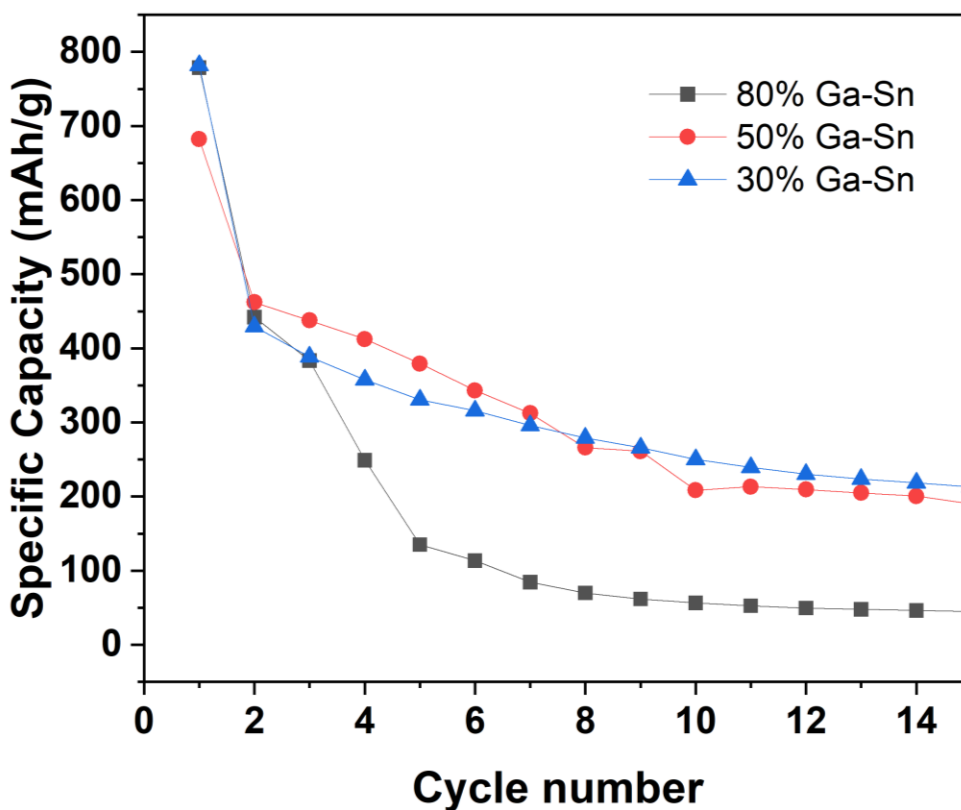
Figure 5.12 Cycling performance of Ga-Sn anodes with 30%, 50%, and 80% active materials tested under 60 °C.

5.5 Conclusion

In this study, we demonstrate the concept of using Ga-Sn LMNPs as low melting point anode materials for lithium ion batteries with PEO solid electrolyte. The morphological evolutions were investigated via ex-situ SEM and operando TXM, which indicate the reversibility of nm-sized active materials during cycling. The Ga-Sn LMNPs demonstrate self-healing ability at room

temperature, which avoided the cracking and delamination issues caused by volume expansion during cycling. The operando and ex-situ XRD results revealed that the crystalline evolution of the Ga-Sn electrode is Ga-Sn liquid metal - Li_2Ga_7 - LiGa - Li_2Ga. There is a solid solution formation process when lithium is inserted into LiGa crystal. Li_2Ga will be formed only with very low current or high temperatures. The 8% Sn was not observed to participate in the electrochemical reaction to form Li_xSn alloys reversibly by both operando XRD and the CV test. By employing a PEO-based solid electrolyte at an elevated temperature of 60 °C, the liquid metal anode showed reversible lithium insertion and extraction and a better cycling capability than the control cells with Sn and MCMB anodes. Besides, the mass ratio of active material is another factor that influenced its cycling performance. These results indicate that the liquid metal electrode can maintain the mechanical integrity of the electrode and better contact with PEO solid electrolytes, due to its advantageous features of liquid, such as self-healing ability and fluidity. This study offers a new strategy to employ a combination of liquid metal alloys and polymer solid electrolytes to address some challenges in rechargeable lithium ion batteries with solid electrolytes.

6. IN SITU SINGLE PARTICLE CHARACTERIZATION OF DYNAMIC MORPHOLOGICAL AND PHASE CHANGES IN SELENIUM-DOPED GERMANIUM ANODE DURING (DE)LITHIATION PROCESSES

6.1 Abstract

The electrochemical kinetics and dynamic morphological changes of selenium-doped germanium ($Ge_{0.9}Se_{0.1}$) at the single particle scale were investigated via synchrotron-based in situ X-ray computed tomography coupled with transmission X-ray microscopy with an energy scan. This method provides both morphological and chemical information during cycling processes. A newly developed single particle cell has been implemented to investigate the performance of $Ge_{0.9}Se_{0.1}$ without the impacts caused by X-ray damage and the limitations of the traditional coin cell. The results provide insights into both morphological and compositional characteristics of $Ge_{0.9}Se_{0.1}$ under operating conditions, which helps understand the outstanding cycling performance of $Ge_{0.9}Se_{0.1}$. This in situ and operando technique based on a single particle battery cell provides an approach to understanding the intrinsic electrochemical kinetics and dynamics of the active material without the interference of the inactive materials in the battery electrode as well as the X-ray-induced damage.

6.2 Introduction

Lithium ion batteries (LIBs) have emerged as a leading energy storage technology for electric vehicles and electronics. The continuing need for higher energy density and better rate capability requires a fundamental understanding of electrochemical kinetics in battery electrodes at multiple length scales. The electrochemical kinetics of LIB electrode materials involve lithium ion diffusion between the liquid electrolyte and each individual active particle, the electrochemical reaction at the interface of the electrolyte and active material particles, and the transport of Li ions and electrons within particles [177]. Although it has been established that the structural, morphological, and chemical evolution are critical factors for the capacity, rate capability and cycling lifetime of LIBs, the detailed dynamic processes during charging and discharging have not been understood thoroughly, which require advanced operando measurement to investigate chemical information at high spatial resolution. Recently, X-ray computed tomography with

nanometers resolution has been used for tracking the degradation in LIBs and has provided valuable microstructural images in three-dimensions (3D). However, the traditional in situ coin cell with Kapton windows used for operando transmission X-ray microscopy (TXM) [138] and X-ray diffraction (XRD) [92, 94] does not have uniform stack pressure and electrical conductance along the punched holes, which can cause the active material particles in the area in contact with the Kapton window to have different electrochemical kinetics compared to the majority of active material particles in other areas. To address this problem, a multipurpose X-ray (AMPIX) cell has been developed recently at the Argonne National Laboratory to provide a more reliable electrochemical setup due to its homogeneous stack pressure and rigid electrically conductive windows [79]. However, these setups have rotating limitations that make tomography experiments difficult. Besides, the coin cell not only suffers from X-ray-induced damage problems to the binder [178] but also involves interactions between additives and active materials [138].

To develop a working cell compatible with tomography is challenging because the cell must function normally as a working battery without blocking the X-ray beam over 180 degrees of rotation. Wang et al. synthesized carbon-coated tin particles on carbon paper via a chemical vapor deposition method [147, 179]. The electrode was modified and fabricated into a Kapton capillary cell they designed for X-ray nanotomography analysis. Regardless of what counter electrode they employed, whether lithium or sodium, the interaction between different active material particles on the same electrode was inevitable. Lim et al. employed a carbon wire electrode coated by a germanium (Ge) microparticle slurry for operando transmission X-ray microscopy and in situ computed tomography. In this experiment, some of the active material particles were active while a few of them were inactive due to the intensive X-ray exposure [146]. The low stiffness of the carbon wire electrode induced slight movement and rotation during the entire measurement, which makes reconstruction and analysis difficult. Zhou et al. developed an in situ focused ion beam - scanning electron microscopy (FIB-SEM) technique and employed it to investigate the microstructural evolution of a variety of high capacity battery materials [105, 141, 180-184]. However, the irreversible damage to the material due to the focused ion beam polishing is permanent and unavoidable. In addition, an ionic liquid electrolyte has to be used in the vacuum environment of the FIB-SEM chamber, which is different from the organic solvent-based electrolyte used in commercial LIBs. There exists a need for techniques that can investigate the properties of electrode materials in a manner that can avoid interference from the other factors.

The electrodes of LIBs include active material particles, carbon additives, polymer binders, and current collectors. These complicated architectures and components of the conventional electrodes lead to interactions between each component and variations in both particle size and shape distributions. It is difficult to extract the intrinsic kinetics and properties of the active material itself. Tsai et al. recently reported the three-dimensional microstructural evolution of $LiNi_{1/3}Mn_{1/3}Co_{1/3}O_2$ (NMC) and $LiNi_{0.8}Co_{0.15}Al_{0.05}O_2$ (NCA) cathode materials in a single particle cell via ex-situ synchrotron TXM nanotomography [177]. They used similarly sized spherical particles and performed cycling experiments at C/3 in an argon-filled glovebox to each specific voltage and an ex-situ tomography image was collected. Although the particles have similar size, there are variances including shapes, manufacturing differences, and chemical distributions inside each individual object. These diversities have potential influences on the phenomena observed.

To address these challenges, we developed a single particle battery for in situ transmission X-ray microscopy with energy scan and X-ray computed tomography measurements for the pristine, lithiated, and delithiated states. In this study, selenium-doped germanium ($Ge_{0.9}Se_{0.1}$) was tested using the developed in situ single particle battery. Klavetter et al. had demonstrated by doping a small portion of selenium into germanium, the network formed during cycling has the ability to alleviate strain and enhance lithium diffusion, and therefore, increase its electrochemical performance [56] and this phenomenon was further proven by operando XRD, TXM, and X-ray absorption spectroscopy (XAS) as reported in ref [146]. In this study, we selected micron-sized $Ge_{0.9}Se_{0.1}$ to ensure the practical relevance of the results to the traditional coin cell. The single particle cell was galvanostatically cycled between 0.01 and 1.5 V. The operando TXM was employed periodically to monitor the morphological changes under operating conditions while in situ transmission X-ray microscopy with energy scan and computed tomography was conducted at each critical state. Using these combined techniques, the dynamic morphological changes, volumetric expansion in 3D, and chemical compositions are characterized at the single particle scale for the first time.

6.3 Experimental section

6.3.1 Fabrication of operando cell

The synthesis of $Ge_{0.9}Se_{0.1}$ has been reported previously in ref [56]. The working electrode was fabricated by attaching a $Ge_{0.9}Se_{0.1}$ particle to a precoated tungsten probe via ion beam carbon deposition performed on a Zeiss Nvision 40 FIB-SEM at the Center of Nanoscale Materials, Argonne National Laboratory. The tungsten probe (Ted Pella, Inc. Redding, CA, USA) was coated with polydimethylsiloxanes (PDMS, Sylgard 184, Dow Corning, Auburn, MI, USA) that suppressed the tungsten oxidation side reaction. A thin layer of carbon was deposited where the particle contacts the conductive probe using the sputtering function of the FIB to ensure a stable and low-resistance electrical contact. A small piece of lithium metal (thickness of 0.6 mm foil, Sigma-Aldrich, St. Louis, MO, USA) was attached to a copper wire (Alfa Aesar, Reston, VA, USA) as a counter electrode. Both electrodes were placed inside a quartz capillary tube (Hampton, Aliso Viejo, CA, USA) with a diameter of 3 mm. The wall thickness is 10 µm where the particle is located. 1M $LiPF_6$ electrolyte in a 1:1 volume ratio mixture of ethylene carbonate and dimethyl carbonate solution (Sigma-Aldrich, St. Louis, MO, USA) was injected into the capillary tube via a micro-syringe. The open end of the quartz capillary housing was sealed via 5 min epoxy followed by torr epoxy (Torr seal vacuum epoxy, Agilent Technologies, Lexington, MA, USA) to prevent leaking of the electrolyte. The entire in situ cell assembly was performed in an argon-filled glovebox (under O_2<0.1 ppm, H_2O<0.5 ppm, Unilab 2000, Mbraun, Stratham, NH, USA). The $Ge_{0.9}Se_{0.1}$ cell was cycled at a constant current (approximately 1 C) controlled by a Keithley 6430 subfemtoamp sourcemeter (Tektronix, Beaverton, OR, USA). The in situ cell assembly is depicted in **Figure 6.1**.
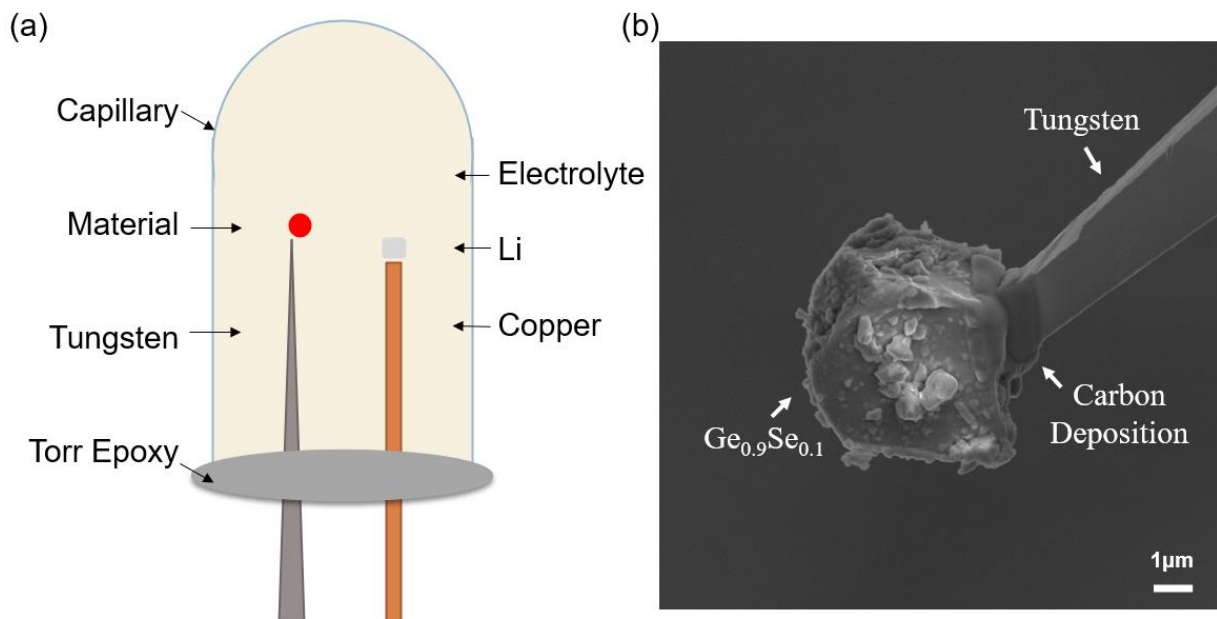
Figure 6.1 (a) Schematic of the operando cell assembly. (b) An SEM image of a $Ge_{0.9}Se_{0.1}$ particle attached to a tungsten probe by carbon deposition.

6.3.2 In situ coin cell assembly

The $Ge_{0.9}Se_{0.1}$ electrode for XANES was fabricated from a 50:30:20 (weight%) mixture of active material, carbon black, and polyvinylidene difluoride (PVDF). The mixture was added into the NMP solution and mixed homogeneously for 12 h. The produced slurries were coated onto a thin copper foil and dried at 100 °C in a vacuum oven for 12 h. Circular discs with a 1.11 cm diameter were punched out of the electrode films and stored in an argon-filled glove box for coin cell assembly. Traditional CR2032 coin cells were modified and used in this study. 2 mm diameter holes were punched at the center of both anode and cathode cases and sealed with 30 µm thick Kapton tape on both sides of the case. **Figure 6.2** displays the order of the operando coin cell assembly. The stainless-steel current collector on top of the anode case with a 2 mm hole was to maximize the contact of the electrode. The electrode was placed on the collector followed by adding 20 µL $LiPF_6$ electrolyte. A Celgard 2400 separator was placed on top of the electrode with an additional 20 µL electrolyte placed on top of it. A piece of lithium metal with a 1.27 mm diameter was laid on the separator followed by another stainless-steel plate (with a 2 mm hole at the center) and wave spring. The cell was crimped and taken out of the glove box for electrochemical evaluation.
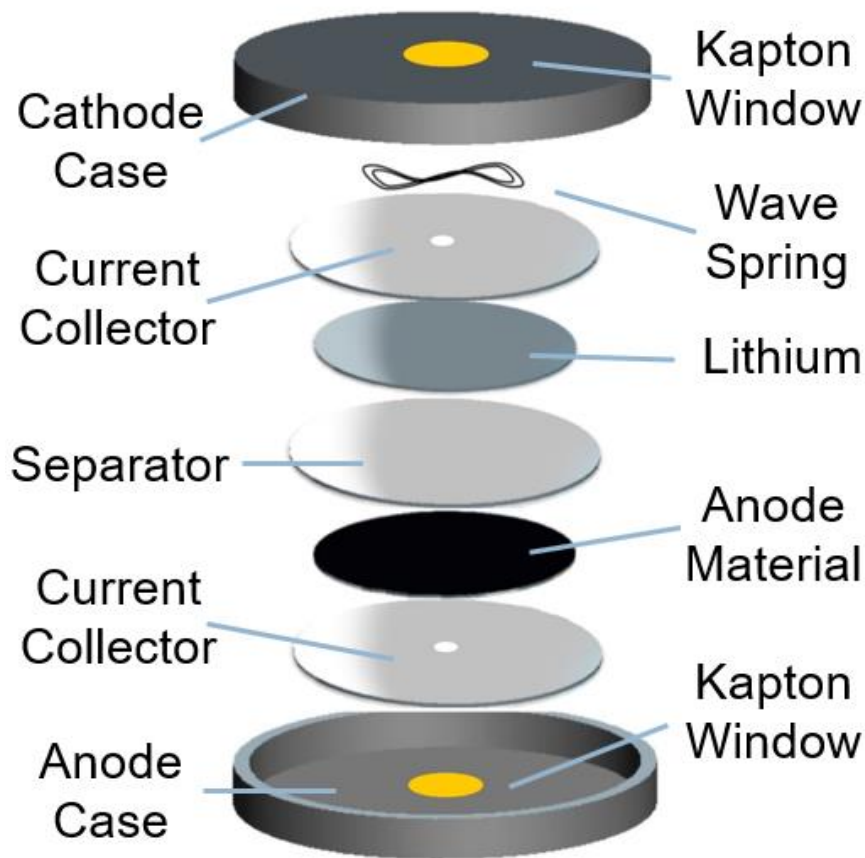
Figure 6.2 In situ coin cell assembly

6.3.3 Operando transmission X-ray microscopy and in situ tomography measurements

Transmission X-ray microscopy has been increasingly used in the field of battery research during the past few years. The operando synchrotron-based TXM with a field of view of 94 µm by 78 µm at 38.4 nm pixel size was implemented periodically to capture the morphological information in real-time for the $Ge_{0.9}Se_{0.1}$ cell. The experiment was conducted at beamline 32-ID-C at the Advanced Photon Source of the Argonne National Laboratory equipped with a Si 111 double crystal monochromator which enables an energy resolution of $\triangle E/E = 10^{-4}$. Two-dimensional operando TXM images were consecutively collected to monitor the single particle under operating conditions. We employed a 2.5 min time interval between data acquisition with an exposure time of 1 s. A schematic of the TXM is depicted in **Figure 6.3**. The X-ray beam is focused down to micrometers by the condenser. The beam stop and pinhole are used to block unfocused X-ray beams. The transmitted photons can illuminate the sample, thereafter, generating

magnified images by the Fresnel zone plate and collected by the detector. In order to perform 3D visualization and quantification analysis, we captured a series of 361 images over a 180° rotation with an exposure time of 1s and step size of 0.5° to generate a computed tomographic dataset.
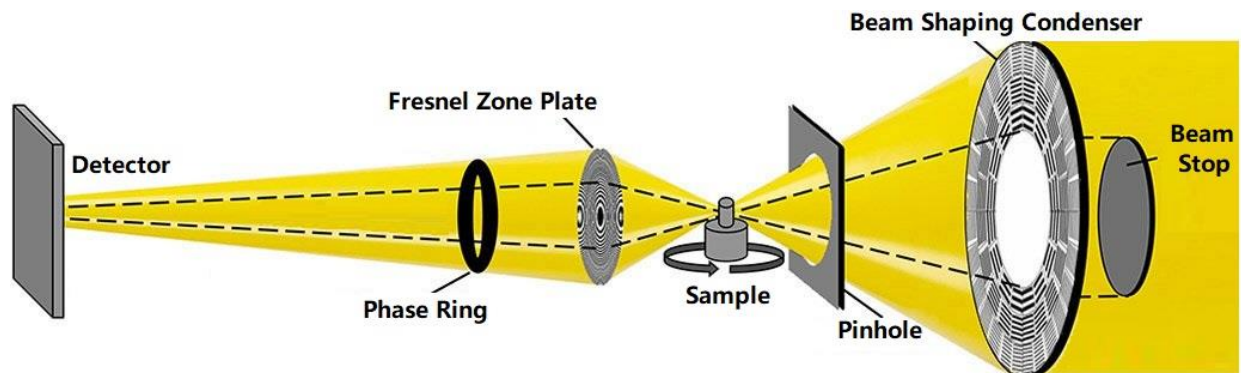
Figure 6.3 Schematic of the synchrotron-based transmission X-ray microscopy setup [183]

6.3.4 Transmission X-ray microscopy with energy scan

The absorption contrast is the most common TXM imaging mode for material research based on X-ray attenuation changes through a sample being imaged. The Beer-Lambert Law relates the X-ray absorption to the composition and thickness of the sample through which the beam is traveling. X-ray absorption occurs when the photon energy approaches a defined energy shell of a specific element. The energy values applied and their corresponding spectrum imaged could be utilized as an indicator of the chemical composition and its oxidation status. To obtain spectroscopy imaging, a set of images at different energies from 11050 to 11200 eV across the K-edge of germanium were collected. Different step sizes were adopted with 5 eV for pre-edge before 11075 eV, 4eV for post-edge after 11150 eV, and 1.5 eV between 11075 to 11150 eV for the Ge XANES range. Flat and dark images were collected for normalization followed by a $2 \times 2 \times 2$ three dimensional median filter.

6.3.5 Image processing

The series of nanotomography images were reconstructed using Tomopy [185] with a combination of simultaneous iterative reconstruction techniques via the ASTRA Toolbox [186]. A 3D Median filter was employed for both the reconstructed and XANES images via the commercial software Avizo® to remove random noise caused by sharp and sudden disturbances in

the image signal. Image registration which is the process of aligning all the images into the same coordinates based on the gravitational center and intensity gradient of each image was conducted after the noise removal. The result images were subject to further analysis. OD analysis was performed in the same manner as in ref [146].

6.4   Results and discussion

To understand the dynamic morphological and chemical changes of the active materials without the interference of carbon and binder additives, we have developed a single particle battery cell for operando TXM and in situ computed tomography. This binder-free operando single particle cell eliminates discrepancies caused by particles overlapping in the in-situ coin cell during TXM and the impact of X-ray damage to the binder [178], which provides chemical and morphological information in 3D. The $Ge_{0.9}Se_{0.1}$ single particle cell was cycled at 1 C rate.
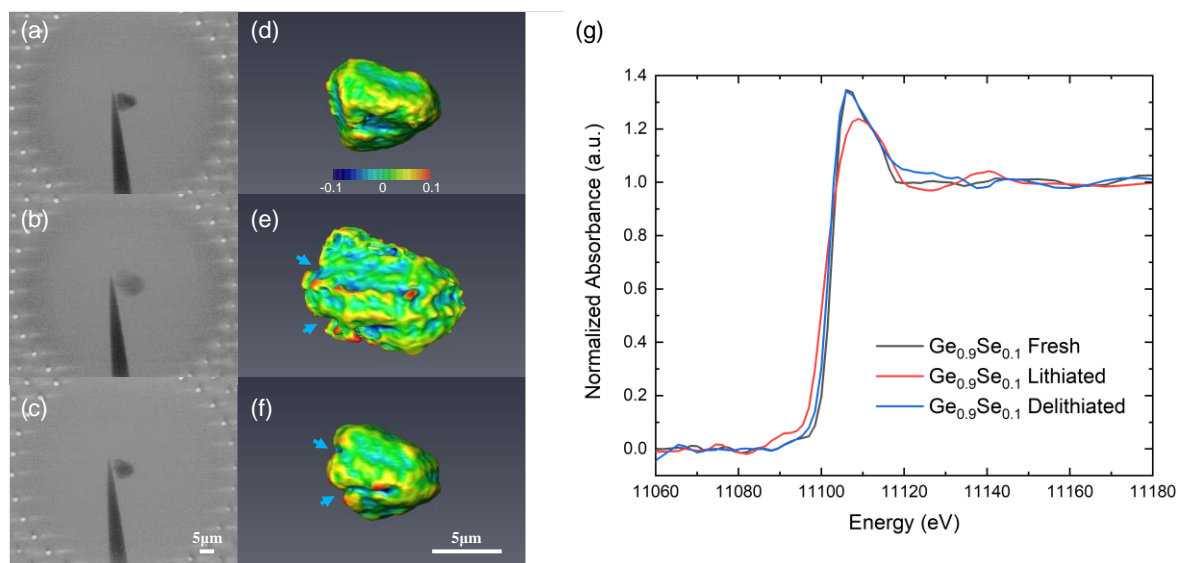
Figure 6.4 The TXM and corresponding 3D morphological evolutions of a single $Ge_{0.9}Se_{0.1}$ particle cell at the (a,d) pristine, (b,e) lithiated, and (c,f) delithiated states. (g) XANES spectra generated via transmission X-ray microscopy images.

Figure 6.4 displays the 2D TXM images (a-c) and the corresponding 3D mean surface curvature view (d-f) of a $Ge_{0.9}Se_{0.1}$ particle attached to a tungsten probe captured at 11200 eV while the tungsten probe was set to be invisible during visualization. The volume expansion of the $Ge_{0.9}Se_{0.1}$ particle is about 293% after lithiation, which is close to the theoretical volume expansion of Ge [141]. After delithiation, the particle recovered back to its original shape and the volume is

slightly larger (4%) than its pristine state. As pointed to by the arrows in **Figure 6.4e** and **f**, there are two cracks generated during the lithiation process and retained during the delithiation process. These two cracks were initiated from the defects caused by the focused ion beam during the carbon deposition. **Figure 6.4g** shows the X-ray absorption near edge structure (XANES) spectra of the $Ge_{0.9}Se_{0.1}$ particle at pristine, lithiated, and delithiated states. After lithiation, the white line shifted to higher energy, which indicates the formation of Li_xGe. The XANES spectra also show that the chemical composition after delithiation has the same white line position and almost identical shape compared with its pristine state. The XANES results and the volume change of the $Ge_{0.9}Se_{0.1}$ particle demonstrate that almost all the lithium ions are reversible during the lithiation and delithiation processes at a 1 C rate in the $Ge_{0.9}Se_{0.1}$ single particle cell. The XANES results of the single particle cell are different from previous studies via operando XAS or TXM for coin cells in which the white line positions of the pristine and delithiated states are slightly different. The in situ coin cells suffer from the interactions between complex architectures of the electrode, volume expansion, and the formation of cracks that might cause delamination of the active materials from the current collector, therefore limiting the intercalation and extraction of lithium ions.

The dynamic morphological change of the $Ge_{0.9}Se_{0.1}$ particle is shown in the video in the supporting information. By selecting the contour line of its pristine state as the area of interest (**Figure 6.5a**), the optical density (OD) of the single $Ge_{0.9}Se_{0.1}$ particle changed from 1 at its pristine state to 0.4 after lithiation and recovered back to 1 when delithiation was completed as shown in **Figure 6.5b**. Comparing with the OD results in ref [146], the operando single particle cell exhibits an OD value close to 1 at its pristine state, and a minimum OD value of 0.4 after lithiation was completed. The lower OD value compared to ref [146] indicates that a more completed reaction was acquired. The OD value of $Ge_{0.9}Se_{0.1}$ was able to recover back to 1 further illustrating its outstanding performance which is consistent with the TXM and XANES results shown in **Figure 6.4**. The single particle-based OD analysis is linear for both lithiation and delithiation processes which differs from the traditional coin cell result presented in ref [146]. These differences may due to the inhomogeneous stack pressure along the X-ray pathway through the punched holes for the traditional modified coin cell as well as the interactions between individual active material particles on the electrode. Previous studies have demonstrated the outstanding cycling performance of $Ge_{0.9}Se_{0.1}$ material by testing coin cells for different characterizations such as operando XRD and XAS [56, 146]. The selenium doping not only has

the ability to accelerate lithium diffusion and suppress the formation of $Li_{15}Ge_4$ as reported in ref [146] but also preserves the morphological and volumetric characteristics. Based on the line profile analysis shown in **Figure 6.5d**, an obvious intensity change was observed during lithiation when the time frame reaches 20 min. The intensity gradient becomes smaller between the particle and the background as well as the tungsten probe due to the propagation of lithium ions from the outside to the core of the $Ge_{0.9}Se_{0.1}$ particle. At the end of lithiation, the boundary of the particle expands 120 pixels and the line profile becomes flat with an intensity value close to the background corresponding to the OD drop to 0.4 as in **Figure 6.5b**. The line profile was recovered back to its original state after delithiation, which demonstrates its good reversibility.
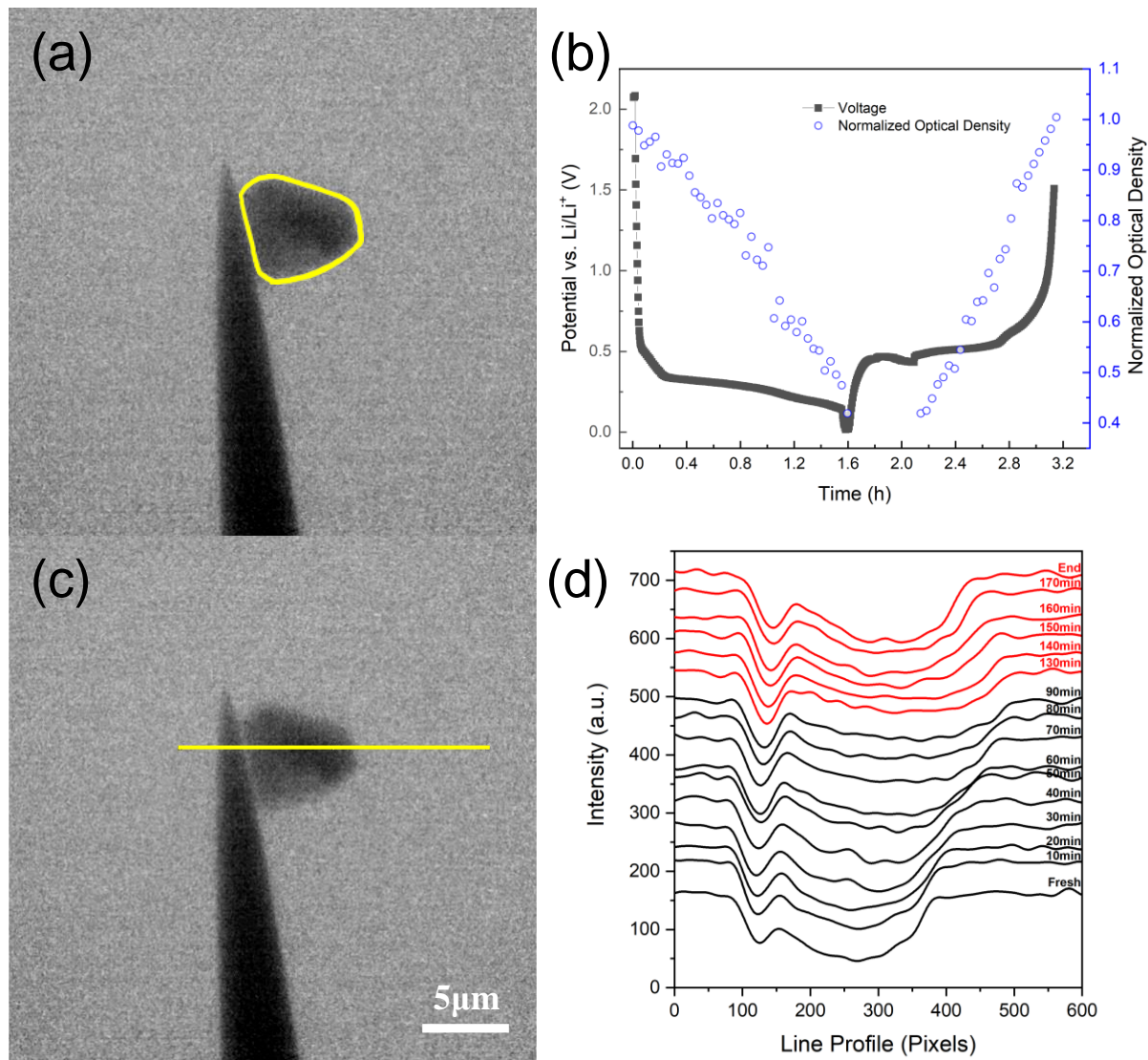
Figure 6.5 (a, c) Area of interest as highlighted in yellow of the single particle $Ge_{0.9}Se_{0.1}$ cell and (b, d) the corresponding optical density and line profile analysis results at the selected time frame. The cell was under relaxation with no current between 1.6-2.1 h during imaging for in situ tomography and XANES.

To compare with the single particle cell, an in situ $Ge_{0.9}Se_{0.1}$ coin cell with Kapton window was fabricated and cycled at a 1 C rate and in situ XANES experiments were conducted for the pristine, lithiated, and delithiated states. As shown in **Figure 6.6a**, the voltage profile shows the reaction plateaus of Ge in both the discharge and charge processes. However, the shape of the XANES spectra at lithiated and delithiated states shown in **Figure 6.6b** is mostly identical to its

pristine state, which indicates limited lithium ions were consumed by the active material particles during the high current reactions for the area where images were captured. To investigate the morphological changes of $Ge_{0.9}Se_{0.1}$ particles, image registration and subtraction were performed by using three images from the pristine, the end of lithiation, and the end of delithiation as shown in **Figure 6.6c-e**. **Figure 6.6f** and **g** show the differences between these images. Since there are almost no black areas in **Figure 6.6f** and **g**, it indicates that most of the $Ge_{0.9}Se_{0.1}$ particles in the image did not have volume change during the 1 C cycling process, which is consistent with the XANES results shown in **Figure 6.6b**. Similar phenomena were previously observed in ref [138, 187], which is due to the nonuniform stack pressure and current inhomogeneities caused by the punched holes. The area of the punched holes is 0.0003 cm^2 compared to the entire electrode of 1 cm^2 which represents only 0.03% of the area. Therefore, incomplete reactions along the X-ray pathway may not affect the entire performance significantly. Hence, the complex architecture of the electrode with multiple variables influences the performance of the active material itself. The proposed single particle cell isolates uncertainties caused by additives in the traditional electrode, which provides more accurate and reliable experiment results.
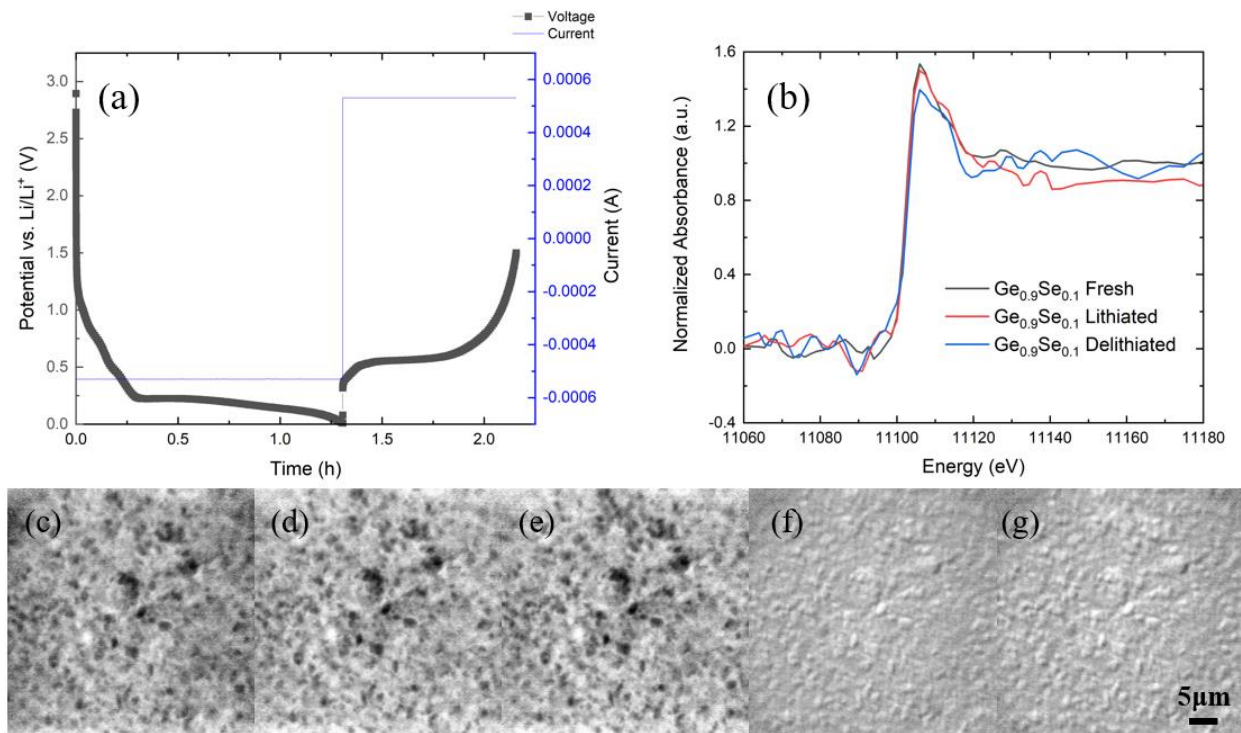
Figure 6.6 (a) Potential plots of a $Ge_{0.9}Se_{0.1}$ electrode cycled at a 1 C rate in the in situ coin cell and (b) the corresponding transmission X-ray microscopy-based germanium XANES spectra. (c) TXM image of the pristine $Ge_{0.9}Se_{0.1}$ electrode. (d) TXM image of the lithiated $Ge_{0.9}Se_{0.1}$ electrode. (e) TXM image of the delithiated $Ge_{0.9}Se_{0.1}$ electrode. (f) differences between (c) and (d) by image subtraction. (g) differences between (d) and (e) by image subtraction.

To validate the coin cell performance at 1 C, a smaller current was employed for the in situ coin cell for comparison as well. Images were captured periodically to monitor the chemical and morphological changes for the $Ge_{0.9}Se_{0.1}$ electrode at 0.1 C. The radiographs were recorded each 60 min interval during their first cycle. There are some missing data, which is due to the unexpected beam outage at the APS during the battery cycling process. The $Ge_{0.9}Se_{0.1}$ XANES spectra shown in **Figure 6.7** were calculated and normalized based on the entire electrode visualized in each TXM image sequence. The white line of the Ge spectrum is sharp at the beginning and becomes broader as lithiation proceeds (after 7 hours) for the $Ge_{0.9}Se_{0.1}$ electrode. The broadening of the peak shape means that the electrons in Ge are less confined, which is due to either the amorphization process or crystal lattice increase [174]. The shape transformation of Ge spectra without a distinct peak at 11113 eV indicates the formation of amorphous Li_xGe phases. At the end of delithiation, the Ge spectrum was partially recovered but it does not exhibit the same

shape as its pristine state, which demonstrates the formation of amorphous Ge after delithiation and residual Li_xGe phases due to the impact of X-rays on the carbon binder matrix as reported in ref [92]. These observations were previously reported in references [92, 146] via operando XAS measurements and are now validated through the TXM experiments reported here. The current rate applied to the in situ coin cells plays an essential role during the operando experiment. Comparing the XANES spectra between **Figure 6.6** and **Figure 6.7**, the high current rate applied upon cycling with weak stack pressure along the X-ray route may lead to a large resistance and lagged electrochemical reaction, and therefore, influence the reaction phenomenon observed. The slow current rate diminished the current inhomogeneity which alleviates the impact of resistance and reinforces a more complete reaction. **Figure 6.7** exhibits similar results compared with the single particle $Ge_{0.9}Se_{0.1}$ anode material in **Figure 6.4g** during lithiation with differences in the delithiation process, which is mainly caused by the complex architecture and the incomplete delithiation reaction in the coin cells. The TXM images from the pristine, lithiated, and delithiated states are shown in **Figure 6.7 b-d**. The black spots displayed in **Figure 6.7e** demonstrate the differences between its pristine and lithiated states. Most of the active material particles have been lithiated during the discharge process. As shown in **Figure 6.7f**, only a few active material particles were delithiated and partially recovered. Although the coin cell may represent a real-world battery, it exhibits different phenomena compared with the single particle cell. Nevertheless, the electrochemical kinetics of the active materials in the coin cell was affected by the complicated architecture and components of the conventional electrodes. The single particle cell can reveal the electrochemical kinetics of the material and benefit the understanding of the active material itself.
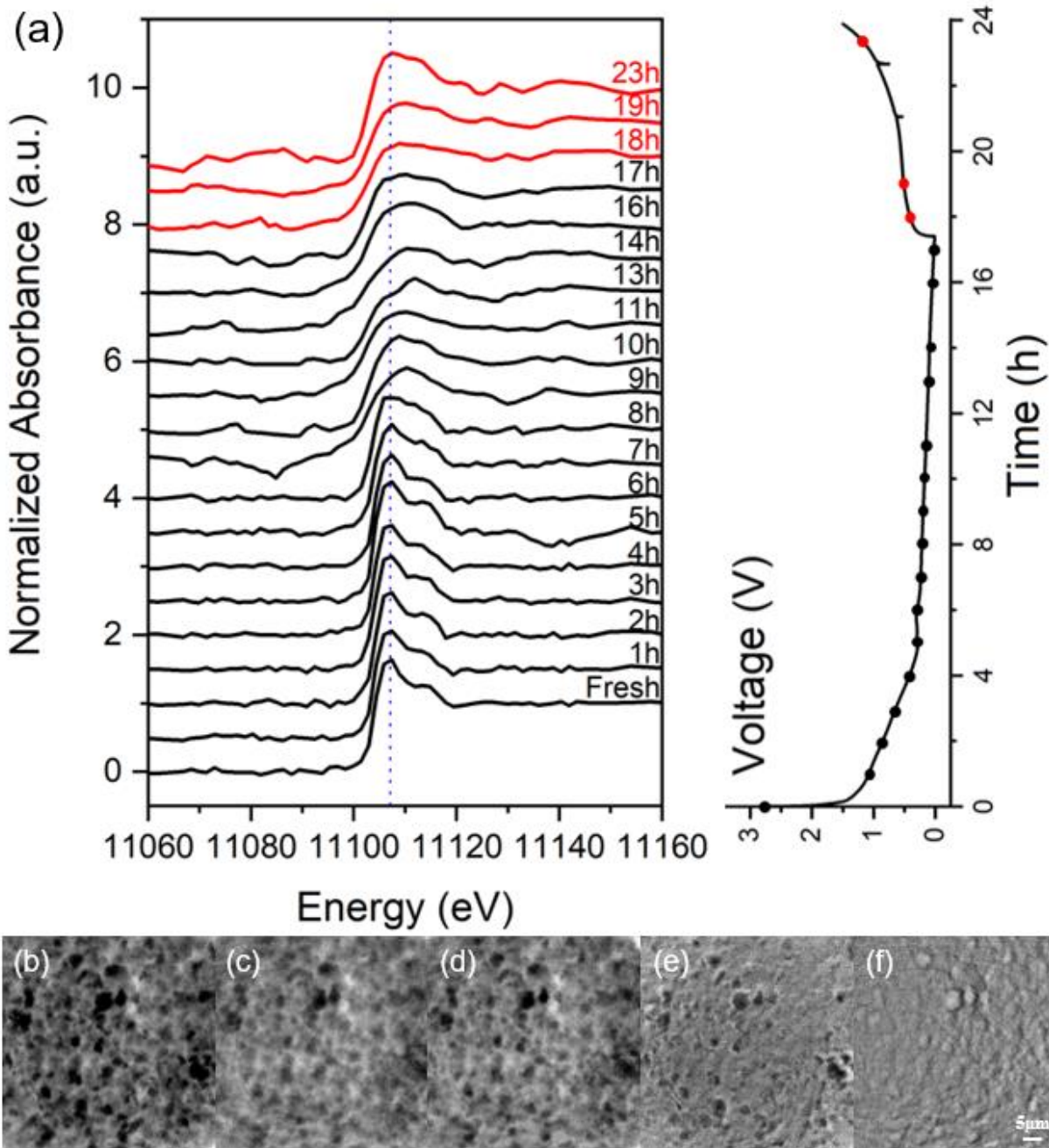
Figure 6.7 (a) Transmission X-ray microscopy-based germanium XANES spectra and potential plots for $Ge_{0.9}Se_{0.1}$ electrodes cycled at 0.1 C rate. TXM image from (b) pristine, (c)lithiated, (d)delithiated status, and (e) image subtraction between (b) and (c), (f) image subtraction between (c) and (d).

6.5   Conclusion

The electrochemical kinetics and morphological evolution of battery electrodes at the single particle scale are examined and measured via operando TXM, in situ TXM with energy scans and X-ray computed nanotomography for the first time. The same $Ge_{0.9}Se_{0.1}$ material at the coin cell scale is tested for comparison as well. The traditional coin cells with complex architectures lead to interactions between each component, therefore, limiting the understanding of the intrinsic kinetics of the active material. The multicomponent mixtures that suffer from X-ray damage make the operando experiment even more difficult. The single particle cell presented in this experiment avoids translational and rotational artifacts which provide a stable and reliable method to investigate the active material itself. Without the impact from X-rays and the complicated structures in the traditional cells, $Ge_{0.9}Se_{0.1}$ exhibits outstanding performance at a 1 C rate. This operando experiment successfully demonstrates applications to the single particle cell for anode materials with promising potential for cathode particles as well, which will assist in understanding the intrinsic electrochemical kinetics and dynamics of the active material under study.

7. CONCLUSIONS

Different high capacity anode materials have been investigated and analyzed in this dissertation. Regardless of particle size variations, a simultaneous volume expansion phenomenon was observed by employing a galvanostatically cycled tin anode, which due to the negative feedback mechanism in the heterogeneous battery electrode. Volume expansion is more likely to be initiated at the highly curved region for nonspherical active tin materials because of its increased average bulk lithium ion concentration at the large curvature end compared to the spherical end. Thereafter, the entire particle expanded almost homogeneously. Compared to the Ge material, $Ge_{0.9}Se_{0.1}$ has a more homogeneous volume change and smoother surface which are attributed to the super-ionically conductive Li-Se-Ge network that contributes to the fast ion transportation and the ability to alleviate volume expansion. The formation of the crystalline $Li_{15}Ge_4$ phase was suppressed due to the encapsulation of the in-situ formed Li-Se-Ge network on the nanosized Ge particles that explains the good mechanical stability, outstanding cycling performance, and rate capability of $Ge_{0.9}Se_{0.1}$ material. In order to mitigate cracking issues caused by volume expansion, a liquid metal nanoparticle Ga-Sn anode was proposed and validated. This Ga-Sn anode material demonstrates the self-healing ability at room temperature which maintained the mechanical integrity of the electrode and better contact with PEO solid electrolyte, prevented the cracking and delamination issues caused by volume expansion during cycling. Whether cathode or anode consists of active materials, carbon, and binder additives which may not represent the property of the material itself. A newly designed single particle schematic was developed and validated by cycling a $Ge_{0.9}Se_{0.1}$ particle alone without any interferences caused by the complex architecture of the electrode. The dynamic results reveal the extraordinary chemical and morphological reversibility of $Ge_{0.9}Se_{0.1}$ compared to the Ge material. This dissertation provides some fundamental understandings regarding the reaction mechanisms of anode materials and the effect of doping, as well as a potential strategy to overcome pulverization and delamination caused by volume expansion, and a novelty designed schematic capable of testing the active material itself.

8. FUTURE WORK

Gallium liquid metal with a low melting point has been proposed as an anode candidate which delivers a theoretical capacity of 769 mAh g^{-1} by taking up two lithium ions for full lithiation. Liquid metal anode coupled with solid electrolyte provides a potential solution for unstable SEI especially for full cell setup with limited lithium resources. But there are still several challenges waiting for optimization before being widely commercialized. The fabrication of electrode includes particle size distribution and mass loading of active materials, as well as the selection and properties of solid electrolyte influences the cycling performance together. Making gallium an alloy with other metals (eg. Sn, In, etc.) exhibits an even lower melting point comparing with gallium stand alone. The impact of the amount of doping is still elusive which needs further investigations. The architecture of a real battery is complicated and therefore it is hard to extract the intrinsic characteristics and kinetics for the active material itself. The single particle schematic proposed has been validated by employing several anode materials and has the potential to be expanded to the cathode as well. A few concerns need to be addressed as well when switching to cathode materials including the selection of quartz capillary and liquid electrolyte. $LiNi_{0.8}Co_{0.1}Mn_{0.1}O_2$ (NMC 811) is a promising cathode material with high specific capacity and low cost with problems to be solved before commercialization include thermal instability, gas formation, and the generation of microcracks. Nickle is the most reactive atom which needs special studies. The interference and absorption between X-ray and electrolyte are not negligible due to the relatively low energy of Ni K-edge. Research regarding the selections of electrolytes and optimizations of the single particle setup is necessary when introducing this schematic to cathode materials for the operando experiments.

REFERENCES

[1]   M. Li, J. Lu, Z. Chen, and K. Amine, "30 Years of Lithium-Ion Batteries," *Advanced Materials,* vol. 30, no. 33, p. 1800561, 2018/08/01 2018, doi: 10.1002/adma.201800561.

[2]   D. Pimentel *et al.*, "Food Production and the Energy Crisis," *Science,* vol. 182, no. 4111, p. 443, 1973, doi: 10.1126/science.182.4111.443.

[3]   J. B. Goodenough, "Evolution of Strategies for Modern Rechargeable Batteries," *Accounts of Chemical Research,* vol. 46, no. 5, pp. 1053-1061, 2013/05/21 2013, doi: 10.1021/ar2002705.

[4]   V. Etacheri, R. Marom, R. Elazari, G. Salitra, and D. Aurbach, "Challenges in the development of advanced Li-ion batteries: a review," *Energy & Environmental Science,* 10.1039/C1EE01598B vol. 4, no. 9, pp. 3243-3262, 2011, doi: 10.1039/C1EE01598B.

[5]   M. S. Whittingham, "Electrical Energy Storage and Intercalation Chemistry," *Science,* vol. 192, no. 4244, p. 1126, 1976, doi: 10.1126/science.192.4244.1126.

[6]   K. Mizushima, P. C. Jones, P. J. Wiseman, and J. B. Goodenough, "LixCoO2 (0<x<-1): A new cathode material for batteries of high energy density," *Materials Research Bulletin,* vol. 15, no. 6, pp. 783-789, 1980/06/01/ 1980, doi: https://doi.org/10.1016/0025-5408(80)90012-4.

[7]   R. Yazami and P. Touzain, "A reversible graphite-lithium negative electrode for electrochemical generators," *Journal of Power Sources,* vol. 9, no. 3, pp. 365-371, 1983/01/01/ 1983, doi: https://doi.org/10.1016/0378-7753(83)87040-2.

[8]   J. O. Besenhard and H. P. Fritz, "Cathodic reduction of graphite in organic solutions of alkali and NR4+ salts," *Journal of Electroanalytical Chemistry and Interfacial Electrochemistry,* vol. 53, no. 2, pp. 329-333, 1974/06/25/ 1974, doi: https://doi.org/10.1016/S0022-0728(74)80146-4.

[9]   A. N. Dey and B. P. Sullivan, "The Electrochemical Decomposition of Propylene Carbonate on Graphite," *Journal of The Electrochemical Society,* vol. 117, no. 2, p. 222, 1970, doi: 10.1149/1.2407470.

[10]   G. Eichinger, "Cathodic decomposition reactions of propylene carbonate," *Journal of Electroanalytical Chemistry and Interfacial Electrochemistry,* vol. 74, no. 2, pp. 183-193, 1976/12/10/ 1976, doi: https://doi.org/10.1016/S0022-0728(76)80234-3.

[11]   J. B. Goodenough and K.-S. Park, "The Li-Ion Rechargeable Battery: A Perspective," *Journal of the American Chemical Society,* vol. 135, no. 4, pp. 1167-1176, 2013/01/30 2013, doi: 10.1021/ja3091438.

[12]   M. S. Whittingham, "Lithium Batteries and Cathode Materials," *Chemical Reviews,* vol. 104, no. 10, pp. 4271-4302, 2004/10/01 2004, doi: 10.1021/cr020731c.

[13]   M. Wohlfahrt-Mehrens, C. Vogler, and J. Garche, "Aging mechanisms of lithium cathode materials," *Journal of Power Sources,* vol. 127, no. 1, pp. 58-64, 2004/03/10/ 2004, doi: https://doi.org/10.1016/j.jpowsour.2003.09.034.

[14]   S. R. Gowda, K. G. Gallagher, J. R. Croy, M. Bettge, M. M. Thackeray, and M. Balasubramanian, "Oxidation state of cross-over manganese species on the graphite electrode of lithium-ion cells," *Physical Chemistry Chemical Physics,* 10.1039/C4CP00764F vol. 16, no. 15, pp. 6898-6902, 2014, doi: 10.1039/C4CP00764F.

[15]   C. H. Chen, J. Liu, M. E. Stoll, G. Henriksen, D. R. Vissers, and K. Amine, "Aluminum-doped lithium nickel cobalt oxide electrodes for high-power lithium-ion batteries," *Journal of Power Sources,* vol. 128, no. 2, pp. 278-285, 2004/04/05/ 2004, doi: https://doi.org/10.1016/j.jpowsour.2003.10.009.

[16]   Y. Itou and Y. Ukyo, "Performance of LiNiCoO2 materials for advanced lithium-ion batteries," *Journal of Power Sources,* vol. 146, no. 1, pp. 39-44, 2005/08/26/ 2005, doi: https://doi.org/10.1016/j.jpowsour.2005.03.091.

[17]   S. K. Martha *et al.*, "On the Thermal Stability of Olivine Cathode Materials for Lithium-Ion Batteries," *Journal of The Electrochemical Society,* vol. 158, no. 10, p. A1115, 2011, doi: 10.1149/1.3622849.

[18]   P. Mukherjee *et al.*, "Surface Structural and Chemical Evolution of Layered LiNi0.8Co0.15Al0.05O2 (NCA) under High Voltage and Elevated Temperature Conditions," *Chemistry of Materials,* vol. 30, no. 23, pp. 8431-8445, 2018/12/11 2018, doi: 10.1021/acs.chemmater.7b05305.

[19]   J. W. Fergus, "Recent developments in cathode materials for lithium ion batteries," *Journal of Power Sources,* vol. 195, no. 4, pp. 939-954, 2010/02/15/ 2010, doi: https://doi.org/10.1016/j.jpowsour.2009.08.089.

[20]   W. Cho *et al.*, "Improved electrochemical and thermal properties of nickel rich LiNi0.6Co0.2Mn0.2O2 cathode materials by SiO2 coating," *Journal of Power Sources,* vol. 282, pp. 45-50, 2015/05/15/ 2015, doi: https://doi.org/10.1016/j.jpowsour.2014.12.128.

[21]   N. N. Sinha and N. Munichandraiah, "Synthesis and Characterization of Carbon-Coated LiNi1/3Co1/3Mn1/3O2 in a Single Step by an Inverse Microemulsion Route," *ACS Applied Materials & Interfaces,* vol. 1, no. 6, pp. 1241-1249, 2009/06/24 2009, doi: 10.1021/am900120s.

[22]   P. He, H. Yu, D. Li, and H. Zhou, "Layered lithium transition metal oxide cathodes towards high energy lithium-ion batteries," *Journal of Materials Chemistry,* 10.1039/C2JM14305D vol. 22, no. 9, pp. 3680-3695, 2012, doi: 10.1039/C2JM14305D.

[23]   S. B. Chikkannanavar, D. M. Bernardi, and L. Liu, "A review of blended cathode materials for use in Li-ion batteries," *Journal of Power Sources,* vol. 248, pp. 91-100, 2014/02/15/ 2014, doi: https://doi.org/10.1016/j.jpowsour.2013.09.052.

[24]   W.-J. Zhang, "Structure and performance of LiFePO4 cathode materials: A review," *Journal of Power Sources,* vol. 196, no. 6, pp. 2962-2970, 2011/03/15/ 2011, doi: https://doi.org/10.1016/j.jpowsour.2010.11.113.

[25]   M. Winter, J. O. Besenhard, M. E. Spahr, and P. Novák, "Insertion Electrode Materials for Rechargeable Lithium Batteries," *Advanced Materials,* vol. 10, no. 10, pp. 725-763, 1998/07/01 1998, doi: 10.1002/(SICI)1521-4095(199807)10:10<725::AID-ADMA725>3.0.CO;2-Z.

[26]   W.-J. Zhang, "A review of the electrochemical performance of alloy anodes for lithium-ion batteries," *Journal of Power Sources,* vol. 196, no. 1, pp. 13-24, Jan 1 2011, doi: 10.1016/j.jpowsour.2010.07.020.

[27]   Z. Chen, I. Belharouak, Y. K. Sun, and K. Amine, "Titanium-Based Anode Materials for Safe Lithium-Ion Batteries," *Advanced Functional Materials,* vol. 23, no. 8, pp. 959-969, 2013/02/25 2013, doi: 10.1002/adfm.201200698.

[28]   B. Zhao, R. Ran, M. Liu, and Z. Shao, "A comprehensive review of Li4Ti5O12-based electrodes for lithium-ion batteries: The latest advancements and future perspectives," *Materials Science and Engineering: R: Reports,* vol. 98, pp. 1-71, 2015/12/01/ 2015, doi: https://doi.org/10.1016/j.mser.2015.10.001.

[29]   T. Ohzuku, A. Ueda, and N. Yamamoto, "Zero-Strain Insertion Material of Li [Li1 / 3Ti5 / 3] O 4 for Rechargeable Lithium Cells," *Journal of The Electrochemical Society,* vol. 142, no. 5, pp. 1431-1435, 1995/05/01 1995, doi: 10.1149/1.2048592.

[30]   W. Xu *et al.*, "Lithium metal anodes for rechargeable batteries," *Energy & Environmental Science,* 10.1039/C3EE40795K vol. 7, no. 2, pp. 513-537, 2014, doi: 10.1039/C3EE40795K.

[31]   J. Liu *et al.*, "Pathways for practical high-energy long-cycling lithium metal batteries," *Nature Energy,* vol. 4, no. 3, pp. 180-186, 2019/03/01 2019, doi: 10.1038/s41560-019-0338-x.

[32]   L. Grande *et al.*, "The Lithium/Air Battery: Still an Emerging System or a Practical Reality?," *Advanced Materials,* vol. 27, no. 5, pp. 784-800, 2015/02/01 2015, doi: 10.1002/adma.201403064.

[33]   A. Manthiram, S.-H. Chung, and C. Zu, "Lithium–Sulfur Batteries: Progress and Prospects," *Advanced Materials,* vol. 27, no. 12, pp. 1980-2006, 2015/03/01 2015, doi: 10.1002/adma.201405115.

[34]   R. Tao *et al.*, "Kinetics Tuning the Electrochemistry of Lithium Dendrites Formation in Lithium Batteries through Electrolytes," *ACS Applied Materials & Interfaces,* vol. 9, no. 8, pp. 7003-7008, 2017/03/01 2017, doi: 10.1021/acsami.6b13859.

[35]   Z. Tu, Y. Kambe, Y. Lu, and L. A. Archer, "Nanoporous Polymer-Ceramic Composite Electrolytes for Lithium Metal Batteries," *Advanced Energy Materials,* vol. 4, no. 2, p. 1300654, 2014/01/01 2014, doi: 10.1002/aenm.201300654.

[36]   R. Chen, W. Qu, X. Guo, L. Li, and F. Wu, "The pursuit of solid-state electrolytes for lithium batteries: from comprehensive insight to emerging horizons," *Materials Horizons,* 10.1039/C6MH00218H vol. 3, no. 6, pp. 487-516, 2016, doi: 10.1039/C6MH00218H.

[37]   Z. Li, J. Huang, B. Yann Liaw, V. Metzler, and J. Zhang, "A review of lithium deposition in lithium-ion and lithium metal secondary batteries," *Journal of Power Sources,* vol. 254, pp. 168-182, 2014/05/15/ 2014, doi: https://doi.org/10.1016/j.jpowsour.2013.12.099.

[38]   L. Beaulieu, K. Eberman, R. Turner, L. Krause, and J. Dahn, "Colossal reversible volume changes in lithium alloys," *Electrochem. Solid-State Lett.,* vol. 4, no. 9, pp. A137-A140, 2001.

[39]   J. W. Choi and D. Aurbach, "Promise and reality of post-lithium-ion batteries with high energy densities," *Nature Reviews Materials,* vol. 1, no. 4, p. 16013, 2016/03/31 2016, doi: 10.1038/natrevmats.2016.13.

[40]   J. R. Szczech and S. Jin, "Nanostructured silicon for high capacity lithium battery anodes," *Energy & Environmental Science,* 10.1039/C0EE00281J vol. 4, no. 1, pp. 56-72, 2011, doi: 10.1039/C0EE00281J.

[41]   H. Tian, F. Xin, X. Wang, W. He, and W. Han, "High capacity group-IV elements (Si, Ge, Sn) based anodes for lithium-ion batteries," *Journal of Materiomics,* vol. 1, no. 3, pp. 153-169, 2015/09/01/ 2015, doi: https://doi.org/10.1016/j.jmat.2015.06.002.

[42]   C. K. Chan *et al.*, "High-performance lithium battery anodes using silicon nanowires," *Nature nanotechnology,* vol. 3, no. 1, pp. 31-35, 2008.

[43]   M.-H. Park, K. Kim, J. Kim, and J. Cho, "Flexible Dimensional Control of High-Capacity Li-Ion-Battery Anodes: From 0D Hollow to 3D Porous Germanium Nanoparticle Assemblies," *Advanced Materials,* vol. 22, no. 3, pp. 415-418, 2010/01/19 2010, doi: 10.1002/adma.200901846.

[44]   X. Su *et al.*, "Silicon-Based Nanomaterials for Lithium-Ion Batteries: A Review," *Advanced Energy Materials,* vol. 4, no. 1, p. 1300882, 2014/01/01 2014, doi: 10.1002/aenm.201300882.

[45]   Y. Xu, Y. Zhu, Y. Liu, and C. Wang, "Electrochemical Performance of Porous Carbon/Tin Composite Anodes for Sodium-Ion and Lithium-Ion Batteries," *Advanced Energy Materials,* vol. 3, no. 1, pp. 128-133, 2013/01/01 2013, doi: 10.1002/aenm.201200346.

[46]   M. T. McDowell, S. W. Lee, W. D. Nix, and Y. Cui, "25th Anniversary Article: Understanding the Lithiation of Silicon and Other Alloying Anodes for Lithium-Ion Batteries," *Advanced Materials,* vol. 25, no. 36, pp. 4966-4985, 2013/09/01 2013, doi: 10.1002/adma.201301795.

[47]   H. Wu and Y. Cui, "Designing nanostructured Si anodes for high energy lithium ion batteries," *Nano Today,* vol. 7, no. 5, pp. 414-429, 2012/10/01/ 2012, doi: https://doi.org/10.1016/j.nantod.2012.08.004.

[48]   A. M. Wilson, J. N. Reimers, E. W. Fuller, and J. R. Dahn, "Lithium insertion in pyrolyzed siloxane polymers," *Solid State Ionics,* vol. 74, no. 3, pp. 249-254, 1994/12/15/ 1994, doi: https://doi.org/10.1016/0167-2738(94)90217-8.

[49]   H. Li, "A High Capacity Nano-Si Composite Anode Material for Lithium Rechargeable Batteries," *Electrochemical and Solid-State Letters,* vol. 2, no. 11, p. 547, 1999, doi: 10.1149/1.1390899.

[50]   H. Kim, J. Choi, H. J. Sohn, and T. Kang, "The Insertion Mechanism of Lithium into Mg2Si Anode Material for Li-Ion Batteries," *Journal of The Electrochemical Society,* vol. 146, no. 12, pp. 4401-4405, 1999/12/01 1999, doi: 10.1149/1.1392650.

[51]   G. X. Wang, L. Sun, D. H. Bradhurst, S. Zhong, S. X. Dou, and H. K. Liu, "Nanocrystalline NiSi alloy as an anode material for lithium-ion batteries," *Journal of Alloys and Compounds,* vol. 306, no. 1, pp. 249-252, 2000/06/23/ 2000, doi: https://doi.org/10.1016/S0925-8388(00)00775-1.

[52]   M. N. Obrovac and V. L. Chevrier, "Alloy Negative Electrodes for Li-Ion Batteries," *Chemical Reviews,* vol. 114, no. 23, pp. 11444-11502, 2014/12/10 2014, doi: 10.1021/cr500207g.

[53]   A. Casimir, H. Zhang, O. Ogoke, J. C. Amine, J. Lu, and G. Wu, "Silicon-based anodes for lithium-ion batteries: Effectiveness of materials synthesis and electrode preparation," *Nano Energy,* vol. 27, pp. 359-376, 2016/09/01/ 2016, doi: https://doi.org/10.1016/j.nanoen.2016.07.023.

[54]   R. A. Huggins, "Lithium alloy negative electrodes," *Journal of Power Sources,* vol. 81-82, pp. 13-19, 1999/09/01/ 1999, doi: https://doi.org/10.1016/S0378-7753(99)00124-X.

[55]   E. M. Conwell, "Properties of Silicon and Germanium," *Proceedings of the IRE,* vol. 40, no. 11, pp. 1327-1337, 1952, doi: 10.1109/JRPROC.1952.273956.

[56]   K. C. Klavetter, J. Pedro de Souza, A. Heller, and C. B. Mullins, "High tap density microparticles of selenium-doped germanium as a high efficiency, stable cycling lithium-ion battery anode material," *Journal of Materials Chemistry A,* 10.1039/C5TA00319A vol. 3, no. 11, pp. 5829-5834, 2015, doi: 10.1039/C5TA00319A.

[57]   D. D. Vaughn Ii and R. E. Schaak, "Synthesis, properties and applications of colloidal germanium and germanium-based nanomaterials," *Chemical Society Reviews,* 10.1039/C2CS35364D vol. 42, no. 7, pp. 2861-2879, 2013, doi: 10.1039/C2CS35364D.

[58]   C. K. Chan, X. F. Zhang, and Y. Cui, "High Capacity Li Ion Battery Anodes Using Ge Nanowires," *Nano Letters,* vol. 8, no. 1, pp. 307-309, 2008/01/01 2008, doi: 10.1021/nl0727157.

[59]   S. Liu, J. Feng, X. Bian, Y. Qian, J. Liu, and H. Xu, "Nanoporous germanium as high-capacity lithium-ion battery anode," *Nano Energy,* vol. 13, pp. 651-657, 2015/04/01/ 2015, doi: https://doi.org/10.1016/j.nanoen.2015.03.039.

[60]   W.-S. Kim, Y. Hwa, H.-C. Kim, J.-H. Choi, H.-J. Sohn, and S.-H. Hong, "SnO2@Co3O4 hollow nano-spheres for a Li-ion battery anode with extraordinary performance," *Nano Research,* vol. 7, no. 8, pp. 1128-1136, 2014/08/01 2014, doi: 10.1007/s12274-014-0475-2.

[61]   Y. Yu, L. Gu, C. Zhu, P. A. van Aken, and J. Maier, "Tin Nanoparticles Encapsulated in Porous Multichannel Carbon Microtubes: Preparation by Single-Nozzle Electrospinning and Application as Anode Material for High-Performance Li-Based Batteries," *Journal of the American Chemical Society,* vol. 131, no. 44, pp. 15984-15985, 2009/11/11 2009, doi: 10.1021/ja906261c.

[62]   D. Wang *et al.*, "Hierarchical nanostructured core–shell Sn@C nanoparticles embedded in graphene nanosheets: spectroscopic view and their application in lithium ion batteries," *Physical Chemistry Chemical Physics,* 10.1039/C3CP44172E vol. 15, no. 10, pp. 3535-3542, 2013, doi: 10.1039/C3CP44172E.

[63]   T. Yang and B. Lu, "Highly porous structure strategy to improve the SnO2 electrode performance for lithium-ion batteries," *Physical Chemistry Chemical Physics,* 10.1039/C3CP54144D vol. 16, no. 9, pp. 4115-4121, 2014, doi: 10.1039/C3CP54144D.

[64]   G. Zhou, D.-W. Wang, L. Li, N. Li, F. Li, and H.-M. Cheng, "Nanosize SnO2 confined in the porous shells of carbon cages for kinetically efficient and long-term lithium storage," *Nanoscale,* 10.1039/C2NR33482H vol. 5, no. 4, pp. 1576-1582, 2013, doi: 10.1039/C2NR33482H.

[65]   X. W. L. a. Y. W. a. C. Y. a. J. Y. L. a. L. A. Archer, "Template-free synthesis of SnO2 hollow nanostructures with high lithium storage capacity," ed, 2006.

[66]   M. Noh, Y. Kwon, H. Lee, J. Cho, Y. Kim, and M. G. Kim, "Amorphous Carbon-Coated Tin Anode Material for Lithium Secondary Battery," *Chemistry of Materials,* vol. 17, no. 8, pp. 1926-1929, 2005/04/01 2005, doi: 10.1021/cm0481372.

[67]   Q. Zhang *et al.*, "Graphene-based carbon coated tin oxide as a lithium ion battery anode material with high performance," *Journal of Materials Chemistry A,* 10.1039/C7TA05256A vol. 5, no. 36, pp. 19136-19142, 2017, doi: 10.1039/C7TA05256A.

[68]   Y. Wu *et al.*, "A room-temperature liquid metal-based self-healing anode for lithium-ion batteries with an ultra-long cycle life," *Energy & Environmental Science,* 10.1039/C7EE01798G vol. 10, no. 8, pp. 1854-1861, 2017, doi: 10.1039/C7EE01798G.

[69]   T. Jiao *et al.*, "Bismuth nanorod networks confined in a robust carbon matrix as long-cycling and high-rate potassium-ion battery anodes," *Journal of Materials Chemistry A,* 10.1039/D0TA02414G vol. 8, no. 17, pp. 8440-8446, 2020, doi: 10.1039/D0TA02414G.

[70]   T. Kennedy, E. Mullane, H. Geaney, M. Osiak, C. O'Dwyer, and K. M. Ryan, "High-Performance Germanium Nanowire-Based Lithium-Ion Battery Anodes Extending over 1000 Cycles Through in Situ Formation of a Continuous Porous Network," *Nano Letters,* vol. 14, no. 2, pp. 716-723, Feb 2014, doi: 10.1021/nl403979s.

[71]   K. T. Lee *et al.*, "Liquid Gallium Electrode Confined in Porous Carbon Matrix as Anode for Lithium Secondary Batteries," *Electrochemical and Solid-State Letters,* vol. 11, no. 3, p. A21, 2008, doi: 10.1149/1.2823262.

[72]   S. B. Patil *et al.*, "Phase Tuning of Nanostructured Gallium Oxide via Hybridization with Reduced Graphene Oxide for Superior Anode Performance in Li-Ion Battery: An Experimental and Theoretical Study," *ACS Applied Materials & Interfaces,* vol. 7, no. 33, pp. 18679-18688, 2015/08/26 2015, doi: 10.1021/acsami.5b05154.

[73]   J.-H. Jeong, D.-W. Jung, and E.-S. Oh, "Lithium storage characteristics of a new promising gallium selenide anodic material," *Journal of Alloys and Compounds,* vol. 613, pp. 42-45, 2014/11/15/ 2014, doi: https://doi.org/10.1016/j.jallcom.2014.06.017.

[74]   C. Sun *et al.*, "Self-supported GaN nanowires with cation-defects, lattice distortion, and abundant active sites for high-rate lithium-ion storage," *Nano Energy,* vol. 68, p. 104376, 2020/02/01/ 2020, doi: https://doi.org/10.1016/j.nanoen.2019.104376.

[75]   S. B. Reese, T. Remo, J. Green, and A. Zakutayev, "How Much Will Gallium Oxide Power Electronics Cost?," *Joule,* vol. 3, no. 4, pp. 903-907, 2019/04/17/ 2019, doi: https://doi.org/10.1016/j.joule.2019.01.011.

[76]   F. Lin *et al.*, "Synchrotron X-ray Analytical Techniques for Studying Materials Electrochemistry in Rechargeable Batteries," *Chemical Reviews,* vol. 117, no. 21, pp. 13123-13186, 2017/11/08 2017, doi: 10.1021/acs.chemrev.7b00007.

[77]   J. Yang *et al.*, "In situ analyses for ion storage materials," *Chemical Society Reviews,* 10.1039/C5CS00734H vol. 45, no. 20, pp. 5717-5770, 2016, doi: 10.1039/C5CS00734H.

[78]   P. P. R. M. L. Harks, F. M. Mulder, and P. H. L. Notten, "In situ methods for Li-ion battery research: A review of recent developments," *Journal of Power Sources,* vol. 288, pp. 92-105, 2015/08/15/ 2015, doi: https://doi.org/10.1016/j.jpowsour.2015.04.084.

[79]   O. J. Borkiewicz, B. Shyam, K. M. Wiaderek, C. Kurtz, P. J. Chupas, and K. W. Chapman, "The AMPIX electrochemical cell: a versatile apparatus for in situ X-ray scattering and spectroscopic measurements," *Journal of Applied Crystallography,* vol. 45, no. 6, pp. 1261-1269, 12/01 2012, doi: 10.1107/S0021889812042720.

[80]   Y.-N. Zhou *et al.*, "High-Rate Charging Induced Intermediate Phases and Structural Changes of Layer-Structured Cathode for Lithium-Ion Batteries," *Advanced Energy Materials,* vol. 6, no. 21, p. 1600597, 2016/11/01 2016, doi: 10.1002/aenm.201600597.

[81]   H. Liu *et al.*, "Capturing metastable structures during high-rate cycling of LiFePO$_4$ nanoparticle electrodes," *Science,* vol. 344, no. 6191, p. 1252817, 2014, doi: 10.1126/science.1252817.

[82]   Z. Yang *et al.*, "In situ high-energy synchrotron X-ray diffraction studies and first principles modeling of α-MnO2 electrodes in Li–O2 and Li-ion coin cells," *Journal of Materials Chemistry A,* 10.1039/C4TA06633B vol. 3, no. 14, pp. 7389-7398, 2015, doi: 10.1039/C4TA06633B.

[83]   K. M. Wiaderek *et al.*, "Comprehensive Insights into the Structural and Chemical Changes in Mixed-Anion FeOF Electrodes by Using Operando PDF and NMR Spectroscopy," *Journal of the American Chemical Society,* vol. 135, no. 10, pp. 4070-4078, 2013/03/13 2013, doi: 10.1021/ja400229v.

[84]   X. Hua *et al.*, "Comprehensive Study of the CuF2 Conversion Reaction Mechanism in a Lithium Ion Battery," *The Journal of Physical Chemistry C,* vol. 118, no. 28, pp. 15169-15184, 2014/07/17 2014, doi: 10.1021/jp503902z.

[85]   O. J. Borkiewicz, K. W. Chapman, and P. J. Chupas, "Mapping spatially inhomogeneous electrochemical reactions in battery electrodes using high energy X-rays," *Physical Chemistry Chemical Physics,* 10.1039/C3CP50590A vol. 15, no. 22, pp. 8466-8469, 2013, doi: 10.1039/C3CP50590A.

[86]   X. Yu *et al.*, "Understanding the Rate Capability of High-Energy-Density Li-Rich Layered Li1.2Ni0.15Co0.1Mn0.55O2 Cathode Materials," *Advanced Energy Materials,* vol. 4, no. 5, p. 1300950, 2014/04/01 2014, doi: 10.1002/aenm.201300950.

[87]   C. Prestipino, O. Mathon, R. Hino, A. Beteva, and S. Pascarelli, "Quick-EXAFS implementation on the general purpose EXAFS beamline at ESRF," (in eng), *Journal of synchrotron radiation,* vol. 18, no. Pt 2, pp. 176-182, 2011, doi: 10.1107/S0909049510046546.

[88]   J. Wang, Y.-c. K. Chen-Wiegart, and J. Wang, "In Situ Three-Dimensional Synchrotron X-Ray Nanotomography of the (De)lithiation Processes in Tin Anodes," *Angewandte Chemie International Edition,* vol. 53, no. 17, pp. 4460-4464, 2014, doi: 10.1002/anie.201310402.

[89]   J. Wang, C. Eng, Y.-c. K. Chen-Wiegart, and J. Wang, "Probing three-dimensional sodiation-desodiation equilibrium in sodium-ion batteries by in situ hard X-ray nanotomography," *Nature Communications,* vol. 6, Jun 2015, Art no. 7496, doi: 10.1038/ncomms8496.

[90]   J. Wang, Y.-c. Karen Chen-Wiegart, C. Eng, Q. Shen, and J. Wang, "Visualization of anisotropic-isotropic phase transformation dynamics in battery electrode particles," *Nature Communications,* Article vol. 7, p. 12372, 08/12/online 2016, doi: 10.1038/ncomms12372 https://www.nature.com/articles/ncomms12372#supplementary-information.

[91]   T. Liu *et al.*, "Correlation between manganese dissolution and dynamic phase stability in spinel-based lithium-ion battery," *Nature Communications,* vol. 10, no. 1, p. 4721, 2019/10/17 2019, doi: 10.1038/s41467-019-12626-3.

[92]   L. Y. Lim, N. Liu, Y. Cui, and M. F. Toney, "Understanding Phase Transformation in Crystalline Ge Anodes for Li-Ion Batteries," *Chemistry of Materials,* vol. 26, no. 12, pp. 3739-3746, 2014/06/24 2014, doi: 10.1021/cm501233k.

[93]   L. Y. Lim, S. Fan, H. H. Hng, and M. F. Toney, "Storage Capacity and Cycling Stability in Ge Anodes: Relationship of Anode Structure and Cycling Rate," *Advanced Energy Materials,* vol. 5, no. 15, p. 1500599, 2015/08/01 2015, doi: 10.1002/aenm.201500599.

[94]   K. E. Silberstein, M. A. Lowe, B. Richards, J. Gao, T. Hanrath, and H. D. Abruña, "Operando X-ray Scattering and Spectroscopic Analysis of Germanium Nanowire Anodes in Lithium Ion Batteries," *Langmuir,* vol. 31, no. 6, pp. 2028-2035, 2015/02/17 2015, doi: 10.1021/la504382q.

[95]   T. M. Bandhauer, S. Garimella, and T. F. Fuller, "A Critical Review of Thermal Issues in Lithium-Ion Batteries," *Journal of the Electrochemical Society,* vol. 158, no. 3, pp. R1-R25, 2011, doi: 10.1149/1.3515880.

[96]   H. X. Kang *et al.*, "Geometric and Electrochemical Characteristics of LiNi1/3Mn1/3Co1/3O2 Electrode with Different Calendering Conditions," *Electrochimica Acta,* vol. 232, pp. 431-438, Apr 2017, doi: 10.1016/j.electacta.2017.02.151.

[97]   C. Lim *et al.*, "Analysis of geometric and electrochemical characteristics of lithium cobalt oxide electrode with different packing densities," *Journal of Power Sources,* vol. 328, pp. 46-55, Oct 2016, doi: 10.1016/j.jpowsour.2016.07.119.

[98] B. Yan, C. W. Lim, Z. B. Song, and L. K. Zhu, "Analysis of Polarization in Realistic Li Ion Battery Electrode Microstructure Using Numerical Simulation," *Electrochimica Acta,* vol. 185, pp. 125-141, Dec 2015, doi: 10.1016/j.electacta.2015.10.086.

[99] T. A. O. Zheng and J. R. Dahn, "CHAPTER 11 - Applications of Carbon in Lithium-Ion Batteries A2 - Burchell, Timothy D," in *Carbon Materials for Advanced Technologies*. Oxford: Elsevier Science Ltd, 1999, pp. 341-387.

[100] A. R. Kamali and D. J. Fray, "TIN-BASED MATERIALS AS ADVANCED ANODE MATERIALS FOR LITHIUM ION BATTERIES: A REVIEW," *Reviews on Advanced Materials Science,* vol. 27, no. 1, pp. 14-24, Feb 2011.

[101] S. Goriparti, E. Miele, F. De Angelis, E. Di Fabrizio, R. P. Zaccaria, and C. Capiglia, "Review on recent progress of nanostructured anode materials for Li-ion batteries," *J. Power Sources,* vol. 257, pp. 421-443, 2014.

[102] G. Ehrlich, C. Durand, X. Chen, T. Hugener, F. Spiess, and S. Suib, "Metallic negative electrode materials for rechargeable nonaqueous batteries," *J. Electrochem. Soc.,* vol. 147, no. 3, pp. 886-891, 2000.

[103] M. Zhang, T. Wang, and G. Cao, "Promises and challenges of tin-based compounds as anode materials for lithium-ion batteries," *Int. Mater. Rev.,* vol. 60, no. 6, pp. 330-352, 2015.

[104] H. X. Dang, K. C. Klavetter, M. L. Meyerson, A. Heller, and C. B. Mullins, "Tin microparticles for a lithium ion battery anode with enhanced cycling stability and efficiency derived from Se-doping," *J. Mater. Chem. A,* vol. 3, no. 25, pp. 13500-13506, 2015.

[105] X. Zhou, T. Li, Y. Cui, Y. Fu, Y. Liu, and L. Zhu, "In Situ Focused Ion Beam Scanning Electron Microscope Study of Microstructural Evolution of Single Tin Particle Anode for Li-Ion Batteries," *ACS Applied Materials & Interfaces,* vol. 11, no. 2, pp. 1733-1738, 2019/01/16 2019, doi: 10.1021/acsami.8b13981.

[106] Y. Cui *et al.*, "Electrochemical behavior of tin foil anode in half cell and full cell with sulfur cathode," *Electrochimica Acta,* vol. 294, pp. 60-67, Jan 2019, doi: 10.1016/j.electacta.2018.10.070.

[107] X. H. Liu, S. Huang, S. T. Picraux, J. Li, T. Zhu, and J. Y. Huang, "Reversible Nanopore Formation in Ge Nanowires during Lithiation-Delithiation Cycling: An In Situ Transmission Electron Microscopy Study," *Nano Letters,* vol. 11, no. 9, pp. 3991-3997, Sep 2011, doi: 10.1021/nl2024118.

[108] J. Liu *et al.*, "Direct growth of SnO2 nanorod array electrodes for lithium-ion batteries," *Journal of Materials Chemistry,* vol. 19, no. 13, pp. 1859-1864, 2009 2009, doi: 10.1039/b817036c.

[109] J. Y. Huang *et al.*, "In Situ Observation of the Electrochemical Lithiation of a Single SnO2 Nanowire Electrode," *Science,* vol. 330, no. 6010, pp. 1515-1520, Dec 10 2010, doi: 10.1126/science.1195628.

[110]   H. X. Dang, K. C. Klavetter, M. L. Meyerson, A. Heller, and C. B. Mullins, "Tin microparticles for a lithium ion battery anode with enhanced cycling stability and efficiency derived from Se-doping," *Journal of Materials Chemistry A,* vol. 3, no. 25, pp. 13500-13506, 2015 2015, doi: 10.1039/c5ta02131f.

[111]   M. Ebner, F. Marone, M. Stampanoni, and V. Wood, "Visualization and Quantification of Electrochemical and Mechanical Degradation in Li Ion Batteries," *Science,* 10.1126/science.1241882 vol. 342, no. 6159, p. 716, 2013.

[112]   F. Sun *et al.*, "In Situ Radiographic Investigation of (De)Lithiation Mechanisms in a Tin-Electrode Lithium-Ion Battery," *ChemSusChem,* vol. 9, no. 9, pp. 946-950, 2016, doi: 10.1002/cssc.201600220.

[113]   B. C. a. J. M. M. A. Buades, "A non-local algorithm for image denoising," *IEEE Computer Society Conference on Computer Vision and Pattern Recognition,* vol. 2, 2005.

[114]   S.-C. Chao, Y.-F. Song, C.-C. Wang, H.-S. Sheu, H.-C. Wu, and N.-L. Wu, "Study on Microstructural Deformation of Working Sn and SnSb Anode Particles for Li-Ion Batteries by in Situ Transmission X-ray Microscopy," *The Journal of Physical Chemistry C,* vol. 115, no. 44, pp. 22040-22047, 2011/11/10 2011, doi: 10.1021/jp206829q.

[115]   Q. Li *et al.*, "In Situ TEM on the Reversibility of Nanosized Sn Anodes during the Electrochemical Reaction," *Chemistry of Materials,* vol. 26, no. 14, pp. 4102-4108, 2014/07/22 2014, doi: 10.1021/cm5009448.

[116]   J. Wang *et al.*, "Structural Evolution and Pulverization of Tin Nanoparticles during Lithiation-Delithiation Cycling," *Journal of The Electrochemical Society,* vol. 161, no. 11, pp. F3019-F3024, 2014.

[117]   M. Zhang, T. Wang, and G. Cao, "Promises and challenges of tin-based compounds as anode materials for lithium-ion batteries," *International Materials Reviews,* vol. 60, no. 6, pp. 330-352, 2015/08/03 2015, doi: 10.1179/1743280415Y.0000000004.

[118]   C. Lim, H. X. Kang, V. De Andrade, F. De Carlo, and L. K. Zhu, "Hard X-ray-induced damage on carbon-binder matrix for in situ synchrotron transmission X-ray microscopy tomography of Li-ion batteries," *Journal of Synchrotron Radiation,* vol. 24, pp. 695-698, May 2017, doi: 10.1107/s1600577517003046.

[119]   S.-C. Chao, Y.-C. Yen, Y.-F. Song, Y.-M. Chen, H.-C. Wu, and N.-L. Wu, "A study on the interior microstructures of working Sn particle electrode of Li-ion batteries by in situ X-ray transmission microscopy," *Electrochemistry Communications,* vol. 12, no. 2, pp. 234-237, 2010/02/01/ 2010, doi: https://doi.org/10.1016/j.elecom.2009.12.002.

[120]   B. Yan, C. Lim, L. Yin, and L. Zhu, "Three Dimensional Simulation of Galvanostatic Discharge of LiCoO2 Cathode Based on X-ray Nano-CT Images," *Journal of the Electrochemical Society,* vol. 159, no. 10, pp. A1604-A1614, 2012, doi: 10.1149/2.024210jes.

[121]   M. Winter and J. O. Besenhard, "Electrochemical lithiation of tin and tin-based intermetallics and composites," *Electrochimica Acta,* vol. 45, no. 1-2, pp. 31-50, 1999, doi: 10.1016/s0013-4686(99)00191-7.

[122] J. Yang, Y. Takeda, N. Imanishi, and O. Yamamoto, "Ultrafine Sn and SnSb0.14 powders for lithium storage matrices in lithium-ion batteries," *Journal of the Electrochemical Society,* vol. 146, no. 11, pp. 4009-4013, Nov 1999, doi: 10.1149/1.1392584.

[123] L. Bazin *et al.*, "High rate capability pure Sn-based nano-architectured electrode assembly for rechargeable lithium batteries," *Journal of Power Sources,* vol. 188, no. 2, pp. 578-582, Mar 2009, doi: 10.1016/j.jpowsour.2008.12.025.

[124] J. Graetz, C. Ahn, R. Yazami, and B. Fultz, "Nanocrystalline and thin film germanium electrodes with high lithium capacity and high rate capabilities," *Journal of The Electrochemical Society,* vol. 151, no. 5, pp. A698-A702, 2004.

[125] C.-Y. Chou and G. S. Hwang, "On the origin of the significant difference in lithiation behavior between silicon and germanium," *Journal of Power Sources,* vol. 263, pp. 252-258, 2014.

[126] T. Kennedy, E. Mullane, H. Geaney, M. Osiak, C. O'Dwyer, and K. M. Ryan, "High-performance germanium nanowire-based lithium-ion battery anodes extending over 1000 cycles through in situ formation of a continuous porous network," *Nano letters,* vol. 14, no. 2, pp. 716-723, 2014.

[127] X. H. Liu, S. Huang, S. T. Picraux, J. Li, T. Zhu, and J. Y. Huang, "Reversible Nanopore Formation in Ge Nanowires during Lithiation–Delithiation Cycling: An In Situ Transmission Electron Microscopy Study," *Nano Letters,* vol. 11, no. 9, pp. 3991-3997, 2011/09/14 2011, doi: 10.1021/nl2024118.

[128] J. Liu *et al.*, "Direct growth of SnO 2 nanorod array electrodes for lithium-ion batteries," *Journal of Materials Chemistry,* vol. 19, no. 13, pp. 1859-1864, 2009.

[129] J. Y. Huang *et al.*, "In situ observation of the electrochemical lithiation of a single SnO 2 nanowire electrode," *Science,* vol. 330, no. 6010, pp. 1515-1520, 2010.

[130] A. R. Kamali and D. J. Fray, "Tin-based materials as advanced anode materials for lithium ion batteries: a review," *Rev. Adv. Mater. Sci,* vol. 27, no. 1, pp. 14-24, 2011.

[131] K. C. Klavetter, J. P. De Souza, A. Heller, and C. B. Mullins, "High tap density microparticles of selenium-doped germanium as a high efficiency, stable cycling lithium-ion battery anode material," *Journal of Materials Chemistry A,* vol. 3, no. 11, pp. 5829-5834, 2015.

[132] K. J. Harry, D. T. Hallinan, D. Y. Parkinson, A. A. MacDowell, and N. P. Balsara, "Detection of subsurface structures underneath dendrites formed on cycled lithium metal electrodes," *Nature Materials,* vol. 13, no. 1, pp. 69-73, Jan 2014, doi: 10.1038/nmat3793.

[133] D. P. Finegan *et al.*, "In-operando high-speed tomography of lithium-ion batteries during thermal runaway," *Nature communications,* vol. 6, 2015.

[134] M. Ebner, F. Marone, M. Stampanoni, and V. Wood, "Visualization and quantification of electrochemical and mechanical degradation in Li ion batteries," *Science,* vol. 342, no. 6159, pp. 716-720, 2013.

[135] F. Sun *et al.*, "In Situ Radiographic Investigation of (De) Lithiation Mechanisms in a Tin-Electrode Lithium-Ion Battery," *ChemSusChem,* vol. 9, no. 9, pp. 946-950, 2016.

[136] J. Wang, Y. c. K. Chen-Wiegart, and J. Wang, "In Situ Three-Dimensional Synchrotron X-Ray Nanotomography of the (De) lithiation Processes in Tin Anodes," *Angewandte Chemie,* vol. 126, no. 17, pp. 4549-4553, 2014.

[137] J. N. Weker, N. Liu, S. Misra, J. Andrews, Y. Cui, and M. Toney, "In situ nanotomography and operando transmission X-ray microscopy of micron-sized Ge particles," *Energy & Environmental Science,* vol. 7, no. 8, pp. 2771-2777, 2014.

[138] T. Li *et al.*, "Characterization of dynamic morphological changes of tin anode electrode during (de)lithiation processes using in operando synchrotron transmission X-ray microscopy," *Electrochimica Acta,* vol. 314, pp. 212-218, 2019/08/10/ 2019, doi: https://doi.org/10.1016/j.electacta.2019.05.056.

[139] L. C. Loaiza *et al.*, "Electrochemical Lithiation of Ge: New Insights by Operando Spectroscopy and Diffraction," *The Journal of Physical Chemistry C,* vol. 122, no. 7, pp. 3709-3718, 2018/02/22 2018, doi: 10.1021/acs.jpcc.7b11249.

[140] C. Lim, H. Kang, V. De Andrade, F. De Carlo, and L. Zhu, "Hard X-ray-induced damage on carbon-binder matrix for in situ synchrotron transmission X-ray microscopy tomography of Li-ion batteries," *Journal of Synchrotron Radiation,* vol. 24, no. 3, pp. 695-698, 2017, doi: doi:10.1107/S1600577517003046.

[141] X. Zhou *et al.*, "In Situ Focused Ion Beam-Scanning Electron Microscope Study of Crack and Nanopore Formation in Germanium Particle During (De)lithiation," *ACS Applied Energy Materials,* 2019/04/04 2019, doi: 10.1021/acsaem.9b00380.

[142] D. Kammer and P. W. Voorhees, "The morphological evolution of dendritic microstructures during coarsening," *Acta Materialia,* vol. 54, no. 6, pp. 1549-1558, 4// 2006, doi: https://doi.org/10.1016/j.actamat.2005.11.031.

[143] W. Tang *et al.*, "Probing Lithium Germanide Phase Evolution and Structural Change in a Germanium-in-Carbon Nanotube Energy Storage System," *Journal of the American Chemical Society,* vol. 137, no. 7, pp. 2600-2607, Feb 2015, doi: 10.1021/ja5116259.

[144] C. Luo *et al.*, "Selenium@Mesoporous Carbon Composite with Superior Lithium and Sodium Storage Capacity," *ACS Nano,* vol. 7, no. 9, pp. 8003-8010, 2013/09/24 2013, doi: 10.1021/nn403108w.

[145] G.-L. Xu *et al.*, "Insight into the Capacity Fading Mechanism of Amorphous Se2S5 Confined in Micro/Mesoporous Carbon Matrix in Ether-Based Electrolytes," *Nano Letters,* vol. 16, no. 4, pp. 2663-2673, 2016/04/13 2016, doi: 10.1021/acs.nanolett.6b00318.

[146] T. Li *et al.*, "In Situ and Operando Investigation of the Dynamic Morphological and Phase Changes of Selenium-doped Germanium Electrode during (De)Lithiation Processes," *Journal of Materials Chemistry A,* 10.1039/C9TA09750C 2019, doi: 10.1039/C9TA09750C.

[147] J. Wang, K. Chen-Wiegart Yu-chen, and J. Wang, "In Situ Three-Dimensional Synchrotron X-Ray Nanotomography of the (De)lithiation Processes in Tin Anodes," *Angewandte Chemie International Edition,* vol. 53, no. 17, pp. 4460-4464, 2014, doi: 10.1002/anie.201310402.

[148] G. C. Iltis, R. T. Armstrong, D. P. Jansik, B. D. Wood, and D. Wildenschild, "Imaging biofilm architecture within porous media using synchrotron-based X-ray computed microtomography," *Water Resources Research,* vol. 47, no. 2, 2011, doi: 10.1029/2010WR009410.

[149] S. Müller *et al.*, "Quantification and modeling of mechanical degradation in lithium-ion batteries based on nanoscale imaging," *Nature Communications,* vol. 9, no. 1, p. 2340, 2018/06/14 2018, doi: 10.1038/s41467-018-04477-1.

[150] R. Chen *et al.*, "Intermetallic SnSb nanodots embedded in carbon nanotubes reinforced nanofabric electrodes with high reversibility and rate capability for flexible Li-ion batteries," *Nanoscale,* 10.1039/C9NR04645C vol. 11, no. 28, pp. 13282-13288, 2019, doi: 10.1039/C9NR04645C.

[151] H. J. Gonzalez Malabet, D. Juarez Robles, V. de Andrade, P. P. Mukherjee, and G. J. Nelson, "In Operando XANES Imaging of High Capacity Intermetallic Anodes for Lithium Ion Batteries," *Journal of The Electrochemical Society,* vol. 167, no. 4, p. 040523, 2020/03/04 2020, doi: 10.1149/1945-7111/ab78fb.

[152] Q. H. Nguyen, N. T. Hung, S. J. Park, I. T. Kim, and J. Hur, "Enhanced performance of carbon-free intermetallic zinc titanium alloy (Zn-ZnxTiy) anode for lithium-ion batteries," *Electrochimica Acta,* vol. 301, pp. 229-239, 2019/04/01/ 2019, doi: https://doi.org/10.1016/j.electacta.2019.01.182.

[153] P. R. Abel *et al.*, "Nanostructured Si(1-x)Gex for Tunable Thin Film Lithium-Ion Battery Anodes," *ACS Nano,* vol. 7, no. 3, pp. 2249-2257, 2013/03/26 2013, doi: 10.1021/nn3053632.

[154] K. H. Seng, M.-H. Park, Z. P. Guo, H. K. Liu, and J. Cho, "Self-Assembled Germanium/Carbon Nanostructures as High-Power Anode Material for the Lithium-Ion Battery," *Angewandte Chemie International Edition,* vol. 51, no. 23, pp. 5657-5661, 2012/06/04 2012, doi: 10.1002/anie.201201488.

[155] T. Kennedy, M. Brandon, and K. M. Ryan, "Advances in the Application of Silicon and Germanium Nanowires for High-Performance Lithium-Ion Batteries," *Advanced Materials,* vol. 28, no. 27, pp. 5696-5704, 2016/07/01 2016, doi: 10.1002/adma.201503978.

[156] M.-H. Park, Y. Cho, K. Kim, J. Kim, M. Liu, and J. Cho, "Germanium Nanotubes Prepared by Using the Kirkendall Effect as Anodes for High-Rate Lithium Batteries," *Angewandte Chemie International Edition,* vol. 50, no. 41, pp. 9647-9650, 2011/10/04 2011, doi: 10.1002/anie.201103062.

[157] Y. J. Cho *et al.*, "Tetragonal Phase Germanium Nanocrystals in Lithium Ion Batteries," *ACS Nano,* vol. 7, no. 10, pp. 9075-9084, 2013/10/22 2013, doi: 10.1021/nn403674z.

[158] N. Liu, H. Wu, M. T. McDowell, Y. Yao, C. Wang, and Y. Cui, "A Yolk-Shell Design for Stabilized and Scalable Li-Ion Battery Alloy Anodes," *Nano Letters,* vol. 12, no. 6, pp. 3315-3321, 2012/06/13 2012, doi: 10.1021/nl3014814.

[159] J. Wang *et al.*, "Shell-Protective Secondary Silicon Nanostructures as Pressure-Resistant High-Volumetric-Capacity Anodes for Lithium-Ion Batteries," *Nano Letters,* vol. 18, no. 11, pp. 7060-7065, 2018/11/14 2018, doi: 10.1021/acs.nanolett.8b03065.

[160] H. Wang *et al.*, "A binder-free high silicon content flexible anode for Li-ion batteries," *Energy & Environmental Science,* 10.1039/C9EE02615K vol. 13, no. 3, pp. 848-858, 2020, doi: 10.1039/C9EE02615K.

[161] X. Guo *et al.*, "A Self-Healing Room-Temperature Liquid-Metal Anode for Alkali-Ion Batteries," *Advanced Functional Materials,* vol. 28, no. 46, p. 1804649, 2018/11/01 2018, doi: 10.1002/adfm.201804649.

[162] Y. Ding *et al.*, "A Liquid-Metal-Enabled Versatile Organic Alkali-Ion Battery," *Advanced Materials,* vol. 31, no. 11, p. 1806956, 2019/03/01 2019, doi: 10.1002/adma.201806956.

[163] R. D. Deshpande, J. Li, Y.-T. Cheng, and M. W. Verbrugge, "Liquid Metal Alloys as Self-Healing Negative Electrodes for Lithium Ion Batteries," *Journal of The Electrochemical Society,* vol. 158, no. 8, p. A845, 2011, doi: 10.1149/1.3591094.

[164] M. W. Verbrugge, R. D. Deshpande, J. Li, and Y.-T. Cheng, "The search for high cycle life, high capacity, self healing negative electrodes for lithium ion batteries and a potential solution based on lithiated gallium," *MRS Proceedings,* vol. 1333, pp. mrss11-1333-m05-04, 2011, Art no. mrss11-1333-m05-04, doi: 10.1557/opl.2011.1065.

[165] W. Liang *et al.*, "Nanovoid Formation and Annihilation in Gallium Nanodroplets under Lithiation–Delithiation Cycling," *Nano Letters,* vol. 13, no. 11, pp. 5212-5217, 2013/11/13 2013, doi: 10.1021/nl402644w.

[166] X. Guo, L. Zhang, Y. Ding, J. B. Goodenough, and G. Yu, "Room-temperature liquid metal and alloy systems for energy storage applications," *Energy & Environmental Science,* 10.1039/C9EE01707K vol. 12, no. 9, pp. 2605-2619, 2019, doi: 10.1039/C9EE01707K.

[167] Y. Jin *et al.*, "High-Energy-Density Solid-Electrolyte-Based Liquid Li-S and Li-Se Batteries," *Joule,* vol. 4, no. 1, pp. 262-274, 2020/01/15/ 2020, doi: https://doi.org/10.1016/j.joule.2019.09.003.

[168] Y. Jin *et al.*, "An intermediate temperature garnet-type solid electrolyte-based molten lithium battery for grid energy storage," *Nature Energy,* vol. 3, no. 9, pp. 732-738, 2018/09/01 2018, doi: 10.1038/s41560-018-0198-9.

[169] Y. Zhang *et al.*, "A Safe High-Performance All-Solid-State Lithium–Vanadium Battery with a Freestanding V2O5 Nanowire Composite Paper Cathode," *ACS Applied Materials & Interfaces,* vol. 8, no. 50, pp. 34309-34316, 2016/12/21 2016, doi: 10.1021/acsami.6b10358.

[170] X. Ban, W. Zhang, N. Chen, and C. Sun, "A High-Performance and Durable Poly(ethylene oxide)-Based Composite Solid Electrolyte for All Solid-State Lithium Battery," *The Journal of Physical Chemistry C,* vol. 122, no. 18, pp. 9852-9858, 2018/05/10 2018, doi: 10.1021/acs.jpcc.8b02556.

[171] C. Sun, J. Liu, Y. Gong, D. P. Wilkinson, and J. Zhang, "Recent advances in all-solid-state rechargeable lithium batteries," *Nano Energy,* vol. 33, pp. 363-386, 2017/03/01/ 2017, doi: https://doi.org/10.1016/j.nanoen.2017.01.028.

[172] A. B. Getsoian *et al.*, "Organometallic model complexes elucidate the active gallium species in alkane dehydrogenation catalysts based on ligand effects in Ga K-edge XANES," *Catalysis Science & Technology,* 10.1039/C6CY00698A vol. 6, no. 16, pp. 6339-6353, 2016, doi: 10.1039/C6CY00698A.

[173] Y. Cui *et al.*, "(De)Lithiation Mechanism of Li/SeSx (x = 0–7) Batteries Determined by in Situ Synchrotron X-ray Diffraction and X-ray Absorption Spectroscopy," *Journal of the American Chemical Society,* vol. 135, no. 21, pp. 8047-8056, 2013/05/29 2013, doi: 10.1021/ja402597g.

[174] G. Bunker, "The EXAFS of Disordered Systems and the Cumulant Expansion," in *EXAFS and Near Edge Structure III*, Berlin, Heidelberg, K. O. Hodgson, B. Hedman, and J. E. Penner-Hahn, Eds., 1984// 1984: Springer Berlin Heidelberg, pp. 268-272.

[175] J. Saint, M. Morcrette, D. Larcher, and J. M. Tarascon, "Exploring the Li–Ga room temperature phase diagram and the electrochemical performances of the LixGay alloys vs. Li," *Solid State Ionics,* vol. 176, no. 1, pp. 189-197, 2005/01/14/ 2005, doi: https://doi.org/10.1016/j.ssi.2004.05.021.

[176] K. T. Lee, Y. S. Jung, J. Y. Kwon, J. H. Kim, and S. M. Oh, "Role of Electrochemically Driven Cu Nanograins in CuGa2 Electrode," *Chemistry of Materials,* vol. 20, no. 2, pp. 447-453, 2008/01/01 2008, doi: 10.1021/cm702181m.

[177] P.-C. Tsai *et al.*, "Single-particle measurements of electrochemical kinetics in NMC and NCA cathodes for Li-ion batteries," *Energy & Environmental Science,* 10.1039/C8EE00001H vol. 11, no. 4, pp. 860-871, 2018, doi: 10.1039/C8EE00001H.

[178] C. Lim, H. Kang, V. De Andrade, F. De Carlo, and L. Zhu, "Hard X-ray-induced damage on carbon-binder matrix for in situ synchrotron transmission X-ray microscopy tomography of Li-ion batteries," (in eng), no. 1600-5775 (Electronic).

[179] J. Wang, C. Eng, Y.-c. K. Chen-Wiegart, and J. Wang, "Probing three-dimensional sodiation–desodiation equilibrium in sodium-ion batteries by in situ hard X-ray nanotomography," *Nature Communications,* Article vol. 6, p. 7496, 06/26/online 2015, doi: 10.1038/ncomms8496 https://www.nature.com/articles/ncomms8496#supplementary-information.

[180] X. W. Zhou *et al.*, "In Situ and Operando Morphology Study of Germanium-Selenium Alloy Anode for Lithium-Ion Batteries," *Acs Applied Energy Materials,* vol. 3, no. 7, pp. 6115-6120, Jul 2020, doi: 10.1021/acsaem.0c01148.

[181] X. Zhou *et al.*, "Blade-Type Reaction Front in Micrometer-sized Germanium Particles during Lithiation," *Acs Applied Materials & Interfaces,* vol. 12, no. 42, pp. 47574–47579, 2020.

[182] B. Q. Xiong *et al.*, "Boosting Superior Lithium Storage Performance of Alloy-Based Anode Materials via Ultraconformal Sb Coating-Derived Favorable Solid-Electrolyte Interphase," *Advanced Energy Materials,* vol. 10, no. 4, Jan 2020, doi: 10.1002/aenm.201903186.

[183] R. Amine *et al.*, "A practical phosphorus-based anode material for high-energy lithium-ion batteries," *Nano Energy,* vol. 74, Aug 2020, Art no. 104849, doi: 10.1016/j.nanoen.2020.104849.

[184] B. Q. Xiong *et al.*, "In Situ Construction of an Ultrarobust and Lithiophilic Li-Enriched Li–N Nanoshield for High-Performance Ge-Based Anode Materials," *ACS Energy Letters,* vol. 5, pp. 3490–3497, 2020.

[185] D. Gürsoy, F. De Carlo, X. Xiao, and C. Jacobsen, "TomoPy: a framework for the analysis of synchrotron tomographic data," (in eng), *Journal of synchrotron radiation,* vol. 21, no. Pt 5, pp. 1188-1193, 2014, doi: 10.1107/S1600577514013939.

[186] W. van Aarle *et al.*, "Fast and flexible X-ray tomography using the ASTRA toolbox," *Optics Express,* vol. 24, no. 22, pp. 25129-25147, 2016/10/31 2016, doi: 10.1364/OE.24.025129.

[187] F. Wang *et al.*, "Electrochemical Reaction of Lithium with Nanostructured Silicon Anodes: A Study by In-Situ Synchrotron X-Ray Diffraction and Electron Energy-Loss Spectroscopy," *Advanced Energy Materials,* vol. 3, no. 10, pp. 1324-1331, 2013/10/01 2013, doi: 10.1002/aenm.201300394.